JOINT TRANSPORTATION
RESEARCH PROGRAM
INDIANA DEPARTMENT OF TRANSPORTATION
AND PURDUE UNIVERSITY

Data Interpretation of Automated Plate Load Test (APLT) for Real-Time In Situ Determination of Unbound Layer Resilient Modulus

Bianka Pajo, Peter J. Becker,
Philippe L. Bourdeau, Marika Santagata

SPR-4547 • Report Number: FHWA/IN/JTRP-2023/22 • DOI: 10.5703/1288284317653

RECOMMENDED CITATION

Pajo, B., Becker, P. J., Bourdeau, P. L., & Santagata, M. (2023). *Data interpretation of automated plate load test (APLT) for real-time in situ determination of unbound layer resilient modulus* (Joint Transportation Research Program Publication No. FHWA/IN/JTRP-2023/22). West Lafayette, IN: Purdue University. https://doi.org/10.5703/1288284317653

AUTHORS

Bianka Pajo
Graduate Researcher
Lyles School of Civil Engineering
Purdue University

Peter J. Becker, PhD, PE
Research Engineer
Indiana Department of Transportation
Division of Research and Development

Philippe L. Bourdeau, PhD
Emeritus Professor of Civil Engineering
Lyles School of Civil Engineering
Purdue University

Marika Santagata, PhD
Professor of Civil Engineering
Lyles School of Civil Engineering
Purdue University
mks@purdue.edu
(765) 494-0697
Corresponding Author

JOINT TRANSPORTATION RESEARCH PROGRAM

The Joint Transportation Research Program serves as a vehicle for INDOT collaboration with higher education institutions and industry in Indiana to facilitate innovation that results in continuous improvement in the planning, design, construction, operation, management and economic efficiency of the Indiana transportation infrastructure. https://engineering.purdue.edu/JTRP/index_html

Published reports of the Joint Transportation Research Program are available at http://docs.lib.purdue.edu/jtrp/.

NOTICE

TECHNICAL REPORT DOCUMENTATION PAGE

1. Report No. FHWA/IN/JTRP-2023/22	2. Government Accession No.	3. Recipient's Catalog No.
4. Title and Subtitle Data Interpretation of Automated Plate Load Test (APLT) for Real-Time In Situ Determination of Unbound Layer Resilient Modulus		**5. Report Date** June 2023 **6. Performing Organization Code**
7. Author(s) Bianka Pajo, Peter Becker, Philippe L Bourdeau, and Marika Santagata		**8. Performing Organization Report No.** FHWA/IN/JTRP-2023/22
9. Performing Organization Name and Address Joint Transportation Research Program Hall for Discovery and Learning Research (DLR), Suite 204 207 S. Martin Jischke Drive West Lafayette, IN 47907		**10. Work Unit No.** **11. Contract or Grant No.** SPR-4547
12. Sponsoring Agency Name and Address Indiana Department of Transportation (SPR) State Office Building 100 North Senate Avenue Indianapolis, IN 46204		**13. Type of Report and Period Covered** Final Report **14. Sponsoring Agency Code**

15. Supplementary Notes

Conducted in cooperation with the U.S. Department of Transportation, Federal Highway Administration.

16. Abstract

This project examined the results of an extensive program of (1) cyclic plate loading tests carried out at Purdue University's S-BRITE site on two testing strips comprised of a coarse aggregate (Indiana #53) subbase layer compacted over either untreated or cement-stabilized subgrade, and (2) static loading tests conducted on #53 aggregate compacted in a 3.6-foot-deep testing pit. The testing program on the two strips included multistage resilient modulus (MR) tests and extended cyclic performance tests with random distributed loading (RDL) on both the subbase and the underlying subgrade. Two of the RDL tests were performed at locations where a nonwoven geotextile had been placed between subgrade and subbase. The work was aimed at improving the understanding of the behavior of subbase and subgrade materials under cyclic loading, mitigating ambiguities regarding the performance of subbase and subgrade materials, and exploring the use of automated plate load tests for determining such properties, ultimately advancing the state of pavement design practice at INDOT.

17. Key Words	18. Distribution Statement
aggregates, angle of internal friction, finite element method, geosynthetics, resilient modulus, plate bearing test, rutting, subbase materials, subgrade materials	No restrictions. This document is available through the National Technical Information Service, Springfield, VA 22161.

19. Security Classif. (of this report)	20. Security Classif. (of this page)	21. No. of Pages	22. Price
Unclassified	Unclassified	102 including appendices	

EXECUTIVE SUMMARY

Introduction

As part of the SPR-4327 *Development of Compaction Control Guidelines for Aggregate Drainage Layers and Evaluation of In Situ Permeability Testing Methods for Aggregates* project, two 20′ × 60′ testing strips (6–10″-thick (15.2–25.4 cm) #53 aggregate layer over either untreated or cement-treated subgrade) were constructed at Purdue's S-BRITE facility in West Lafayette, IN. An extensive program of automated cyclic plate loading tests (APLT) was conducted at the site, including multistage resilient modulus (MR) tests, and extended cyclic performance tests with random distributed loading (RDL) on both the subbase and the underlying subgrade. Two of the RDL tests were performed at locations where a nonwoven geotextile was placed between the subgrade and subbase. In addition, three static plate load tests were performed on #53 aggregate compacted in a 9′ × 18′ × 2.5′ deep (2.7 m × 5.5 m × 0.76 m) neighboring testing pit.

The trove of in-situ measurements emanating from these tests, coupled with the extensive site characterization performed as part of SPR-4327, were an invaluable opportunity to improve our understanding of the behavior of subbase and subgrade materials under cyclic loading and to advance the state of pavement design practice at INDOT. The research study summarized in this report was conducted to capitalize on this data, with a specific focus on advancing knowledge of the following.

- The resilient and permanent deformation properties of the unbound aggregate layer and the cement modified subgrade.
- The impact of the foundation layer on the cyclic loading response and resilient modulus of the overlaying granular layer.
- The effect of the presence of a geotextile fabric separator on permanent deformations.
- The parameters required to assess the stability of pavement subbases to construction loading.
- The suitability of automated plate load tests for measuring the resilient modulus of pavement materials in-situ.

Findings

The work performed included the following.

- Review of the literature pertaining to geomaterial resilient modulus and permanent deformation.
- Documentation of the S-BRITE test strip site conditions and the plate load testing equipment, protocols, and results.
- Elastic finite element analyses emulating the plate load test setup to investigate factors affecting the prediction of resilient moduli from plate load tests.
- Analysis of the extended cycle performance RDL tests and evaluation of the applicability of existing models for describing the relationship between accumulated permanent deformation and number of loading cycles.
- Analysis of the static plate load tests and determination of ranges of the internal angle of friction for compacted #53 aggregate.

The work performed generated findings relevant to the *interpretation of MR tests*, performed both directly on the subgrade and on the two-layer system comprised of subbase and subgrade. For tests on the untreated subgrade layer, use of the Boussinesq-based solution with a constant shape factor leads to values of M_r that are consistently lower than those derived from FE analyses conducted using the same hypotheses of homogeneity and isotropic behavior. The shape factor, which is conventionally assumed to be a constant value, is found, based on elastic FE analyses, to decrease with increasing stress level, which indicates that factors other than plate stiffness and stress distribution underneath the plate influence this parameter. Consideration of material anisotropy as measured by the modulus anisotropy ratio ($n = E_h/E_v$) impacts the moduli derived from the FE analyses. Use of the Boussinesq-based solution also leads to underestimating M_r in the case of tests on the cement treated subgrade, since consideration is not given to the presence of the softer underlying natural soil.

When interpreting the tests performed on the compacted aggregate layer overlaying the untreated or cement treated subgrade, the expression commonly used in practice and included in AASHTO (1993) for deriving the M_r of the subgrade from surface elastic deflections measured away from the plate results in inaccurate predictions. The value of M_r for the untreated subgrade back calculated using FE from off-center surface deflection measurements exceeds those obtained from tests performed directly on the subgrade, which are considered more reliable. The assumed degree of anisotropy (as measured by the modulus anisotropy ratio, n) of the aggregate subbase impacts the values of $M_{rSubgrade}$ and $M_{rSubbase}$ derived from the FE analyses, with both of these moduli increasing with increasing n.

The values of $M_{rSubbase}$ derived from the tests performed on the untreated strip are significantly lower (in some cases by almost an order of magnitude) than those estimated for the same aggregate from the tests on the cement-treated strip. This discrepancy appears to be in part due to inaccurate predictions of M_r of the untreated subgrade derived from off-center surface deflections. Foundation conditions also play a role, as discussed in the following.

Overall, a number of factors and assumptions impact the interpretation of plate load tests, including APLTs, which leads to significant uncertainty in the values of the resilient moduli of the tested layers derived from the plate load test data. Compounded with their high cost, this level of uncertainty indicates that plate load tests are not suitable for performing fundamental behavioral studies or to derive M_r values of pavement materials for use in design.

Regarding the *resilient behavior of the geomaterials tested*, estimates of M_r of compacted #53 aggregate derived from the plate load test data are found to vary broadly (3,000–72,000 psi (20.7–496.4 MPa)) depending on the nature of the subgrade (cement treated versus untreated), the testing location, the applied cyclic stress, the assumed modulus anisotropy ratio, and the approach used to derive M_r from the test data. Significant variation is also observed in the values of M_r of the cement treated subgrade derived from the plate load tests. In all cases, they are significantly higher than the Level 3 values (12,500–15,000 psi (86.2–103.4 MPa)) used in current INDOT guidelines and they exceed the values provided in the *MEDPG Manual of Practice* (AASHTO, 2020).

Finally, analysis of the MR and RDL tests performed on the two strips yields insights into the *impact of the foundation layer*. Differences in the foundation layer appear to play a role in the observed discrepancy in the values of the M_r of the #53 subbase layer derived from the MR tests performed on the two strips, with a stiffer underlying layer promoting more effective compaction.

The permanent deformation behavior of the two-layer system is also affected by the subgrade foundation layer, with significantly higher permanent deformations accumulated in the tests on the untreated strip (by a factor as large as 4.5–5 over the duration of the tests performed in this research) compared to the tests on the cement treated strip.

The permanent deformations measured in the RDL test on the untreated strip are primarily due to deformations within the subgrade, with negligible contribution from the aggregate layer. In contrast, the subbase layer appears responsible for the larger fraction (60%–70%) of the accumulated permanent deformations measured in the test on the cement treated strip.

In general, the results of the tests performed on the cement-treated strip display less spatial variability than those on the untreated strip, i.e., cement treatment contributes to more homogeneity in both the subgrade and the overlying compacted aggregate.

RDL tests indicate that at least for the cyclic stresses and the number of loading cycles (<10,000) applied in the tests, the accumulated permanent deformation behavior under repeated loading of the subbase and subgrade (untreated and cement treated) is, in most cases, best modeled using a logarithmic growth model.

As expected, the Class 1 nonwoven geotextile used in the construction of the two strips did not provide any mechanical contribution. Moreover, examination of samples retrieved after completion of the plate load testing program showed evidence of significant damage (tearing, bursting, abrasion), indicating that the filtration and separation functions were compromised by compaction of the overlying aggregate and/or the repeated loading during the RDL tests.

Implementation

Based on the work performed, the following recommendations for implementation are provided.

Plate Load Tests vs. Laboratory Tests

- Given the assumptions that impact the interpretation of plate load tests, including APLTs, laboratory tests—in which boundary conditions are clearly defined and specimen density can be carefully controlled—are deemed more appropriate for investigating fundamental aspects of material behavior, including resilient and permanent deformation behavior.

Interpretation of Plate Load Tests

- Use of the Boussinesq-based solution with a constant shape factor is not recommended for interpreting MR plate load tests on the subgrade. Elastic finite element analyses are preferred. Tests on the cement-treated subgrade should consider the presence of the softer underlying untreated soil.
- For plate load tests on two-layer (subbase over subgrade) systems, M_r of the bottom subgrade layer should not be derived from off-center surface deflections. Tests performed directly on the subgrade should be used to obtain more reliable estimates of $M_{rSubgrade}$.
- Once a reliable estimate of the subgrade M_r is obtained, finite element analyses should be the preferred method for deriving M_r of the overlying aggregate subbase layer, when possible, accounting for material anisotropy.

Plate Load Testing Protocols

- When performing plate load tests on both subbase and subgrade, the position of the plate should be sufficiently offset in the two tests to ensure that the results of the tests performed on the subgrade are not impacted by the loading history produced by the test previously performed on the overlying layer.
- Off-center measurements of surface deflections should be included in all plate load tests whenever possible to inform the interpretation of the tests (e.g., to assess whether the analysis of the test data requires consideration of the deformation of softer underlying layers or, as in the case of static plate load tests, to confirm the bearing capacity failure mechanism).

Selection of Parameters for Use in Design

- Under conditions like those encountered at the S-BRITE soil (A-6 (CL) natural soil, slurry cement stabilization with 4% cement), 25,000 psi (172.4 MPa) represents a conservative estimate for the resilient modulus of the cement modified soil, i.e., type IBC subgrade treatment.
- Based on the static plate load tests conducted in this work, values of the angle of internal friction in the 48°–50° range may be used for estimating the stability of medium-dense #53 aggregate subbases.

Construction Procedures

- Under conditions like those encountered at the S-BRITE site, the subgrade should be cement treated in order to obtain better performance in terms of increased resilient modulus, reduced permanent deformation, and less variable conditions. The results from the S-BRITE site also suggest that the presence of the stiffer cement treated layer promotes more effective compaction of the overlying aggregate.
- A higher-class geotextile product compared to the one used in this project is recommended for use between subgrade and #53 aggregate to provide separation and filtration functions.

The study also highlighted areas where *additional research* is warranted. It is suggested that future efforts be directed towards the following.

- Comparing the results of the plate load testing program to FWD and LWD data collected at the S-BRITE site.
- Comparing M_r estimates obtained from the plate load tests to M_r values derived in the laboratory for the same aggregate and subgrade soil as part of separate investigations.
- Interpreting the S-BRITE APLT data using models developed for the analysis of triaxial tests once the full data for individual cycles are made available.

CONTENTS

LIST OF TABLES

LIST OF FIGURES

1. INTRODUCTION

1.1 Background and Problem Statement

The Mechanistic Empirical Pavement Design (MEPDG) method used by INDOT requires input of the resilient modulus (M_r) for all unbound layers of the pavement structure and the underlying subgrade. Laboratory measurement of the resilient modulus poses some challenges especially for coarser materials, and there remains uncertainty in deriving reliable estimates of M_r from prediction models based on soil type and from field methods such as falling weight deflectometer (FWD), light weight deflectometer (LWD), and dynamic cone penetrometer (DCP).

For coarser materials, current practice in Indiana most often relies on a fixed (Level 3) input value (30,000 psi for a material such as the No. 53 aggregate extensively used as a separator/subbase layer in the state). In the case of subgrades, experience with soils in Indiana suggests that values routinely used in design may be overly conservative, especially for untreated soils.

As part of SPR-4327 (*Development of Compaction Control Guidelines for Aggregate Drainage Layers and Evaluation of In Situ Permeability Testing Methods for Aggregates*), two 20′ × 60′ testing strips (6–10″ thick #53 aggregate layer over either untreated or cement-stabilized subgrade) and a 9′ × 18′ × 2.5′ deep trench were constructed in summer 2020 at Purdue's S-BRITE facility in West Lafayette, IN. A geotextile fabric was used as a separator between the subgrade and the #53 aggregate over a 15′ length of each strip.

An extensive program of static and cyclic plate loading tests was conducted at the site. As discussed in later sections of this report, the testing program included a number of multi-stress, cyclic Automated Plate Load Tests (APLT), which allow for the application of conditioning cycles in situ, adjustable and controlled load pulse durations and frequencies, multi-stress test sequences while measuring peak, rebound and permanent deformations, all under automated load control.

The trove of in situ stress-strain measurements emanating from the APLT tests coupled with the extensive site characterization performed as part of SPR-4327 were deemed an invaluable opportunity to improve the understanding of the behavior of subbase and subgrade materials under cyclic loading, mitigate ambiguities regarding the performance of subbase and subgrade materials, and provide confidence on the M_r values that are currently used in design, ultimately advancing the state of pavement design practice at INDOT. The research study summarized in this report was conducted to capitalize on the data afforded by SPR-4327 and the APLT testing.

1.2 Research Objectives

This research study aimed to improve INDOT's pavement design process. To accomplish this goal, the scope of work for the research study centered around addressing the following objectives.

- Ascertain stress level dependence of the resilient modulus of No. 53 aggregate.
- Verify resilient modulus design values for subgrade treatment types of IBC (14″ chemical modification with cement) and IC (12″ No. 53 aggregate) currently used in INDOT pavement design.
- Establish the impact of the foundation layer on the cyclic loading response and resilient modulus of the overlaying granular layer.
- Quantify the degradation in the modulus of the aggregate layer and the cement treated subgrade with traffic.
- Quantify the effect of the presence of a geotextile fabric separator on permanent deformations.
- Characterize the permanent deformation and rutting potentials of unbound aggregates, soil subgrades, and cement modified subgrades.
- Gain insight into input parameters required to assess the stability of pavement subbases to construction loading.
- Assess the suitability of automated plate load tests for measuring the resilient modulus of pavement materials in-situ.

1.3 Activities and Organization of Report

To address the previously outlined research objectives, the research team developed a work plan involving rigorous analysis of pavement subbase and subgrade mechanistic behavior. The scope of work included the following activities, which are described in the subsequent sections with additional information provided in Appendices A to D.

- Review literature pertaining to geomaterial resilient modulus (Section 2.2 and Appendix A) and permanent deformation (Section 2.3).
- Document S-BRITE test strip and test pit site conditions (Sections 3.2–3.4), APLT equipment (Section 3.5), testing protocols (Section 3.6), and results of APLT testing (Section 3.7).
- Conduct finite element analyses emulating the APLT test setup to investigate factors affecting the prediction of resilient moduli from plate load tests (Chapter 4 and Appendix B).
- Analyze the extended cycle performance tests and examine the applicability of existing models for describing the relationship between accumulated permanent deformation and number of loading cycles (Section 5.3 and Appendix C and Appendix D).
- Analyze the static plate load tests and determine ranges of the internal angle of friction for compacted #53 aggregate (Section 5.2).

2. BACKGROUND

2.1 Introduction

As discussed in the introductory chapter, the primary objective of the work performed for this research project was to explore the use of automated plate load tests (APLT) for determining the resilient and

permanent deformation behavior of unbound aggregate layers.

This chapter is aimed at providing some background on key concepts examined in this work. It is organized into three main sections. The first (Section 2.2) reviews the significance of the resilient modulus (Section 2.2.1), the factors that affect it (Section 2.2.2) and the approaches for its evaluation in practice (Section 2.2.3). As the primary focus of this work was on unbound aggregates, and, in particular, on materials with characteristics similar to those of Indiana #53, a database of resilient modulus values for these materials obtained from a review of the literature is presented in Section 2.2.4.

Section 2.3 focuses on the permanent deformation behavior of aggregates, again discussing its significance, and summarizing the primary factors that affect it based on a review of the literature. Finally, Section 2.4 provides a brief overview of the conventional approach used to interpret plate load test results, based on the theory by Boussinesq (1885). The assumptions implicit in this approach and the factors influencing test interpretation are reviewed.

2.2 Resilient Modulus

2.2.1 Definition and Significance

INDOT uses the Mechanistic Empirical Pavement Design Guide (MEPDG) for the design and analysis of new and renovated pavement structures. The most important input parameter required for the unbound and foundation layers is the resilient modulus (M_r). According to AASHTO T 307-99 (2021a) the resilient modulus (M_r) is defined as "the ratio of the amplitude of the repeated axial stress to the amplitude of the resultant recoverable axial strain."

$$M_r = \frac{\sigma_{cyc}}{\varepsilon_r} \qquad \text{(Eq. 2.1)}$$

where,

σ_{cyc} = repeated axial stress, and
ε_r = axial resilient (recoverable) strain.

The term resiliency was first introduced in pavement design by Hveem and Carmany (1949) and Hveem (1955). It originated from a study of a large number of deflection data obtained from 43 projects on California highway pavements. This work provided evidence that the majority of cracks and fatigue failures occurring in bituminous pavements originated from repeated elastic deflections generated by moving loads. Hveem (1955) introduced a new term for these deflections referring to them as "resilient." It was argued that to improve existing pavement design practices, resilient deformations needed to be measured and the resilient behavior of soil incorporated in design procedures.

Seed and Fead (1960) first introduced the concept of resilient modulus and developed the first testing procedure and apparatus for testing the resilient properties of soil. The repeated loading test (RLT) was performed in a triaxial cell. Several testing methods subsequently emerged in the literature to determine the resilient modulus of unbound pavement materials. The requirement for using the resilient modulus in pavement analysis and design procedures was introduced in the AASHTO 1986 *Guide for the Design of Pavement Structures*. This standard provided guidelines on the loading protocol (magnitude, duration, and frequency) and on the procedures and measurements required to derive the recoverable strain at the end of each loading sequence from which the resilient modulus could be evaluated. Updated versions of the standard include AASHTO T 294-94 and the current testing standard AASHTO T 307-99 (AASHTO, 2021a), which was adopted in 2000. A summary of the advancements of the testing procedures for measuring resilient modulus is provided in Figure 2.1.

Apart from laboratory tests, several authors have investigated means to evaluate the resilient modulus of unbound granular materials from in-situ tests (e.g., Abu-Farsakh et al., 2004; Hoffman, 2004; Lenke et al., 2003; Petersen & Peterson, 2006; Siekmeier et al., 2000). Some of the most common procedures include plate load tests, falling weight deflectometer (FWD) tests, light weight deflectometer (LWD) tests and the dynamic cone penetrometer, and rely on data from the load-deformation curves, back-calculation procedures, and empirical relationships to evaluate M_r.

2.2.2 Factors Affecting Resilient Modulus of Unbound Aggregates

The resilient modulus of granular materials is influenced by a number of factors of varying importance. These include stress level, density, aggregate gradation, loading conditions, and water content. The following paragraphs briefly review the impact of these factors based primarily on the results of cyclic laboratory tests reported in previous studies. A more in-depth discussion of these influences is provided in review articles such as the one by Lekarp et al. (2000).

Stress level: As discussed by Lekarp et al. (2000), stress level is one of the most important factors affecting the resilient behavior of granular materials. Stress level effects refer to two distinct influences: that of the confining stress and that of the applied deviatoric (cyclic) stress. Starting with early work by Seed et al. (1967) and Allen and Thompson (1974), a number of studies have established the significant influence that both confining stress and deviatoric stress have on the resilient modulus. The work by Hicks and Monismith (1971) represents one of the earliest investigations in this area. Based on triaxial cyclic tests on both dry and saturated specimens of well-graded partially crushed gravel and crushed rock aggregates, these authors showed that, in general, M_r increases with an increase in confining stress (Figure 2.2). Other authors (e.g., Hicks, 1970; Maher et al., 2000; Puppala et al., 2011; Rada & Witczak, 1981; Trollope et al., 1962; Uzan,

Test Procedure	Details
AASHTO T-274-1982	Earliest AASHTO test procedure; No details on the sensitivities of displacement measurement devices were given; Criticisms on test procedure, test duration (5 hours long test) and probable failures of soil sample during conditioning phase; testing stresses are too severe.
AASHTO T-292-1991	AASHTO procedure introduced in 1991; Internal measurement systems are recommended; Testing sequence is criticized owing to the possibility of stiffening effects of cohesive soils.
AASHTO T-294-1992	AASHTO modified the T-292 procedure with different sets of confining and deviatoric stresses and their sequence; Internal measurement system is followed; 2-parameter regression models (bulk stress for granular and deviatoric stress model for cohesive soils) to analyze test results; Criticism on the analyses models.
Strategic Highway Research Program P-46-1996	Procedural steps of P-46 are similar to T-294 procedure of 1992; External measurement system was allowed for displacement measurement; Soil specimen preparation methods are different from those used in T-292.
AASHTO T-307-1999	T-307-1999 was evolved from P-46 procedure; recommends the use of external displacement measurement system. Different procedures are followed for both cohesive and granular soil specimen preparation.
NCHRP 1-28 A: Harmonized Method-2004 (RRD 285)	This recent method recommends a different set of stresses for testing. Also, a new 3-parameter model is recommended for analyzing the resilient properties. The use of internal measurement system is recommended in this method.

Figure 2.1 Evolution of AASHTO testing procedures for measuring resilient modulus (Puppala, 2008).

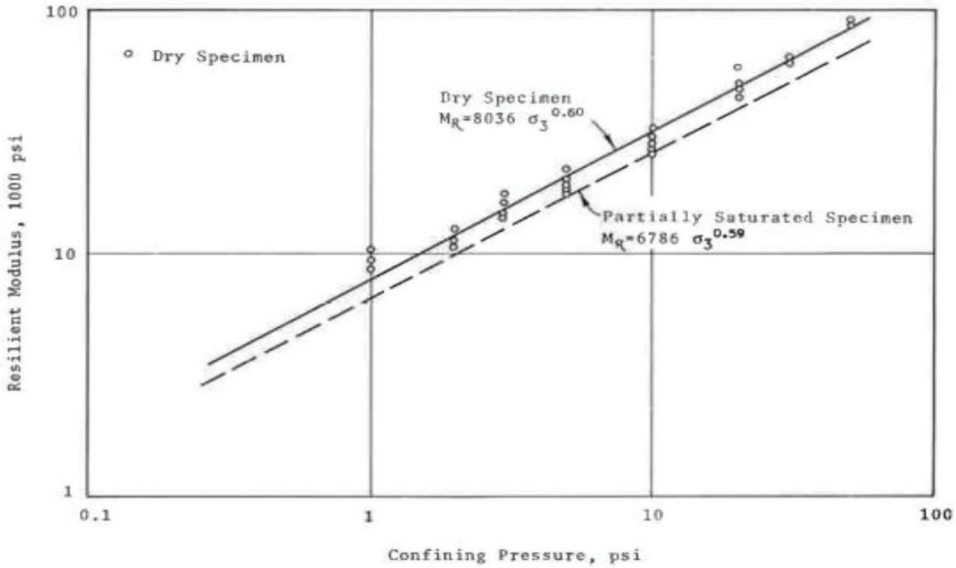

Figure 2.2 Effect of confining stress on the resilient modulus of partially crushed gravel aggregate (Hicks & Monismith, 1971).

1985) have subsequently reported similar results from laboratory investigations on a range of aggregate materials.

Lekarp et al. (2000) report that the deviatoric stress has a secondary effect on the resilient modulus compared to the confining stress. Similar observations have also been made by Allen and Thompson (1974), Papagiannakis and Masad (2008), Uthus (2007), Zeghal (2004), while Trollope et al. (1962) reported no increase in resilient modulus with variations of axial stress ($\sigma_a < \sigma_{failure}$) for repeated cyclic tests conducted on a sandy material.

Hicks and Monismith (1971) showed that the resilient modulus slightly increases with an increase in deviatoric stress for high principal stress ratios (Figure 2.3). Other studies, such as those by Maher et al. (2000), Malla and Joshi (2006), Puppala et al. (2011), and by Nguyen and Mohajerani (2016) have documented similar variation in resilient modulus with deviatoric stress. According to Maher et al. (2000) the mechanism responsible for the increase in modulus is the reorientation of grains into a denser state with an increase in deviatoric stress. However, other studies (e.g., Morgan (1966), Uzan (1985), Pan et al. (2006)) have reported an opposite effect of the deviatoric stress, with M_r shown to decrease slightly with an increase in the applied cyclic stress. Pan et al. (2006) argues that the increase in dilation of soil with increasing deviatoric stress is the mechanism responsible for the observed strain softening.

Several mathematical models have been proposed to describe the stress level dependency of the resilient modulus of granular materials. A summary of some

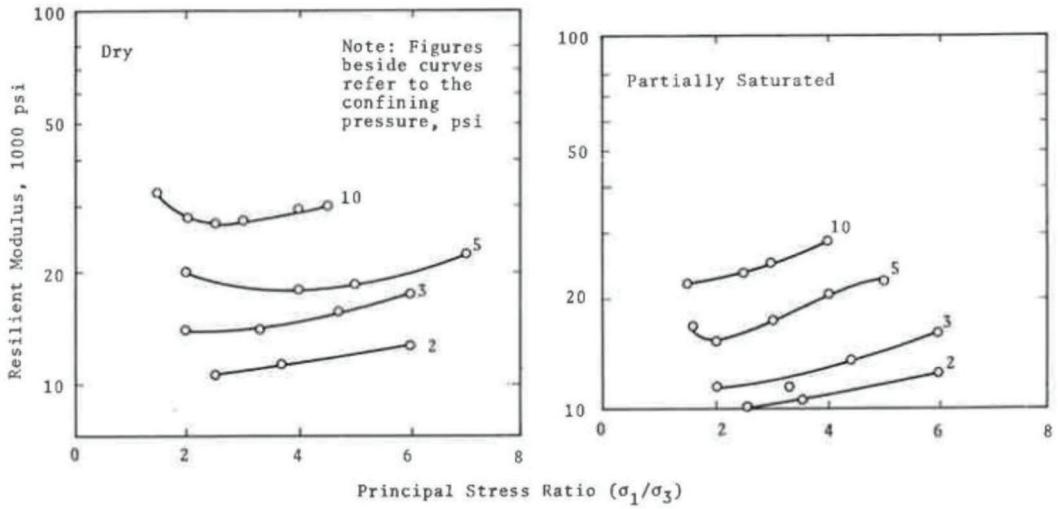

Figure 2.3 Effect of principal stress ratio on the resilient modulus of partially crushed gravel aggregate in dry and partially saturated conditions (Hicks & Monismith, 1971).

commonly used models is presented in Table 2.1 (Nguyen & Mohajerani, 2016). In the earliest models the resilient modulus is expressed as a function of either deviatoric stress or confining stress (sum of principal stresses), while both stresses are considered in later models. While all the equations presented in Table 2.1 follow a log-log relationship, throughout the years models based on a semi-logarithmic structure between M_r and stress (e.g., Andrei et al., 2004) have also been proposed. The model developed through NCHRP Project 1-37A (NCHRP, 2004b), also referred to as the "universal model," is employed by NCHRP for pavement materials in the *Guide for Mechanistic-Empirical Design*.

Density: A number of studies have shown that the resilient modulus of granular materials increases with an increase in density (e.g., Kalcheff & Hicks, 1973; Kolisoja, 1997; Lekarp et al., 2000; Tanimoto & Nishi, 1970; Trollope et al., 1962), although this influence is considered to be small compared to other factors such as stress level and water content (Rada & Witczak, 1981). The effect of density is attributed to the increase in the number of interactions between grains and thus the reduction in the intergranular contact stresses that occur as the soil system is compacted. As a result, the deformations that the grains experience diminish and the resilient modulus increases (Lekarp et al., 2000). Several researchers have proposed relationships between resilient modulus and physical properties, one of them being density, for a variety of granular materials. A review of these models is presented by Titi and Matar (2018).

The impact of density on the resilient behavior of granular soils is affected by other factors. In particular, all parameters, such as fines content, stress level, particle angularity and mineralogy that affect the distribution of the intergranular stresses within the aggregate mass and the degree of particle crushing, play an important role. For example, it has been shown that the effects of density on M_r decrease with increasing fines content (Lekarp et al., 2000) and are almost insignificant for fully crushed aggregate materials and at high stress levels.

Aggregate gradation and fines content: Seed et al. (1967) and Hicks (1970) were some of the earliest authors to investigate the influence of these factors on the resilient modulus of granular materials. In particular, Seed et al. (1967) evaluated laboratory resilient modulus data from 7 different previous studies, and concluded that a variation in fines content in the 2%–10% range had a negligible impact on M_r. In contrast, other researchers have reported a decrease of the resilient modulus with increasing fines content (Hicks & Monismith, 1971; Kamal et al., 1993, Witchmann et al., 2015). This effect is consistent with observations reported in the literature regarding the effect of fines on the initial shear modulus of granular materials. As discussed by Lekarp et al. (2000), the impact of gradation and fines content is also influenced by other factors such as water content and aggregate type.

Several studies have compared the resilient modulus of well graded and uniformly graded aggregate materials. For example, based on laboratory triaxial tests, Shaw (1980) showed that well graded materials have higher resilient modulus than uniformly graded materials.

Loading rate: Laboratory tests have also highlighted the effect of load frequency and load duration on M_r. Seed and Chan (1964) investigated the impact of load duration on the resilient modulus of a silty sand through triaxial repeated loading tests in which the loading period varied between 0.3 s and 20 min. This work showed an approximately 18% increase in resilient modulus as the loading duration decreased in

TABLE 2.1
Models for Resilient Modulus Reported in Literature (Nguyen & Mohajerani, 2016)

$M_r = k_1\left(\frac{\sigma_3}{P_a}\right)^{k_2}$	Dunlap (1963), Monismith et al. (1967)
$M_r = k_1\left(\frac{\sigma_d}{P_a}\right)^{k_2}$	Moossazadeh & Witczak (1981)
$M_r = k_1\left(\frac{\sigma_{sum}}{P_a}\right)^{k_2}$	Seed et al. (1967)
$M_r = K_1 P_a\left(\frac{\sigma_{sum}}{P_a}\right)^{k_2}\left(\frac{\sigma_d}{P_a}\right)^{k_3}$	Uzan (1985)
$M_r = k_2 + k_3(k_1 - \sigma_d)(k_1 \geq \sigma_d)$	Raad & Figueroa (1980), Thompson & Robnett (1979)
$M_r = k_1 P_a\left(\frac{\sigma_{sum}}{P_a}\right)^{k_2}\left(\frac{\tau_{oct}}{P_a}\right)^{k_3}$	Witczak & Uzan (1988)
$M_r = k_1\left(\frac{\sigma_1\sigma_2 + \sigma_2\sigma_3 + \sigma_3\sigma_1}{\tau_{oct}}\right)^{k_2}$	Johnson et al. (1986)
$M_r = k_1\left(\frac{(\sigma_1 + \sigma_2 + \sigma_3)/3}{\sigma_d}\right)^{k_2}$	Tam & Brown (1988)
$M_r = k_1 P_a\left(\frac{\sigma_3}{P_a}\right)^{k_2}\left(\frac{\sigma_d}{P_a}\right)^{k_3}$	Pezo (1993)
$M_r = k_1\left(\frac{\sigma_3}{P_a} + 1\right)^{k_2}\left(\frac{\sigma_d}{P_a} + 1\right)^{k_3}$	Hopkin et al. (2001)
$M_r = k_1 P_a\left(\frac{\sigma_3}{P_a} + 1\right)^{k_2}\left(\frac{\sigma_d}{P_a} + 1\right)^{k_3}$	Ni et al. (2002)
$M_r = k_1 P_a\left(\frac{\sigma_{sum}}{P_a}\right)^{k_2}\left(\frac{\tau_{oct}}{P_a} + 1\right)^{k_3}$	NCHRP 1-37A (NCHRP, 2004b) "universal model"
$M_r = k_1 P_a\left(\frac{\sigma_{sum}}{P_a}\right)^{k_2}\left(\frac{\sigma_d}{P_a} + 1\right)^{k_3}(\sigma_2 = \sigma_3)$	–
$M_r = k_1 P_a\left(\frac{\sigma_{sum} - 3k_4}{P_a}\right)^{k_2}\left(\frac{\tau_{oct}}{P_a} + k_5\right)^{k_3}$	NCHRP 1-28A (NCHRP, 2004a)
$M_r = k_1 P_a\left(\frac{\sigma_{sum}}{P_a} + 1\right)^{k_2}\left(\frac{\sigma_d}{P_a} + 1\right)^{k_3}$	Ooi et al. (2006)
$M_r = k_1 P_a\left(\frac{\sigma_{sum}}{P_a} + 1\right)^{k_2}\left(\frac{\tau_{oct}}{P_a} + 1\right)^{k_3}$	–
$M_r = k_1 P_a\left(\frac{\sigma_{sum} - 3k_4}{P_a}\right)^{k_2}\left(\frac{\tau_{oct}}{P_a} + k_5\right)^{k_3} + k_1(\mu_\alpha - \mu_\omega)^{\beta_1}$	Gupta et al. (2007)

Note:
k_1, k_2, k_3, k_4, k_5, α_1, α_1 = regression coefficients.
σ_3 = confining stress.
σ_d = deviator stress.
σ_{sum} = sum of principal stresses.
τ_{oct} = octahedral shear stress.
P_a = reference stress.
$(\mu_\alpha - \mu_\omega)$ = matric suction.

this range. Coffman et al. (1964) investigated the influence of load frequency on the resilient modulus of granular materials used for base and subbase layers in the AASHO Road Test. A general trend of increasing resilient modulus with load frequency was observed, but the amount of stiffening experienced was reported to be dependent on saturation and density. The results of repeated load triaxial tests on a subbase material reported by Tanimoto and Nishi (1970) also showed that the variation of resilient modulus with load frequency is a function of other properties of the material, and that for a sufficiently large number of load applications the impact of frequency on the resilient properties of unbound aggregate materials is negligible. According to Lekarp et al. (2000), the overall conclusion from the studies available in literature (e.g., Lashine et al., 1971, Robinson, 1974) is that load duration has a small to negligible impact on the measured resilient modulus. The same conclusion is reached regarding the effect of loading frequency, with the exception being close to saturated materials in which excess pore pressures may develop at higher loading frequencies leading to a reduction of the modulus.

Water content and degree of saturation: The effect of these parameters, which are inherently linked, is generally acknowledged to be significant, as illustrated by the very early study by Haynes and Yoder (1963). These authors investigated the variation in resilient

modulus of gravel and crushed stone aggregates for different values of moisture content. They reported that the resilient modulus of gravel aggregates experienced an approximately 50% decrease as the degree of saturation increased from 70% to 100%. A similar effect (20% change in the resilient modulus with degree of saturation going from 70 to 80%) was observed in tests on crushed stone aggregates. Similar observations have been reported by other researchers (e.g., Heydinger et al., 1996; Hicks & Monismith, 1971; Seed et al., 1967). According to Lekarp et al. (2000) different explanations have been put forth in the literature for this behavior. The general view is that with increasing water content and degree of saturation, excess pore pressures can be generated during cyclic loading. This has a direct impact on the effective stress state which controls the overall strength and deformation behavior of the material.

2.2.3 Evaluation of Resilient Modulus in Design Practice

According to NCHRP 1-37A (*Guide for Mechanistic-Empirical Design of New and Rehabilitated Pavement Structures*), the resilient modulus of unbound materials can be obtained from laboratory tests, as well as, from correlations with other material properties such as CBR. These options are reflected in the three "levels of input" available in the MEDPG.

In *Level 1*, M_r is determined from laboratory tests performed on the unbound aggregate material. The recommended standards for evaluating the resilient modulus are NCHRP 1-28A (NCHRP, 2004a; Witczak, 2003) and AASHTO T307 (AASHTO, 2021a). The tests performed in the laboratory are cyclic triaxial tests performed according to the recommended standards under a range of stresses that are intended to be representative of the in-situ loading conditions. NCHRP 1-28A recommends determination of the resilient modulus from a generalized model known as the "universal" model. Linear or nonlinear regression analysis is used to analyze the data obtained from the laboratory tests and determine the regression constants shown in the model of Equation 2.2 (see also Table 2.1).

$$M_r = k_1 P_a \left(\frac{\theta}{P_a}\right)^{k_2} \left(\frac{\tau_{oct}}{P_a} + 1\right)^{k_3} \qquad \text{(Eq. 2.2)}$$

where,

P_a = atmospheric pressure,
θ = bulk stress = $\sigma_1 + \sigma_2 + \sigma_3$,
τ_{oct} = octahedral shear stress
= $\sqrt{(\sigma_1-\sigma_2)^2+(\sigma_1-\sigma_3)^2+(\sigma_2-\sigma_3)^2} \cdot \frac{1}{3}$, and
k_1, k_2, k_3 = constants derived from regression analyses.

k_1, which is necessarily greater than zero, reflects the effect of packing, stress history and particle characteristics. Both k_2 and k_3 represent the relationship between M_r and bulk (volumetric) stress and octahedral (deviatoric) stress, respectively. For aggregate materials, increasing bulk stress and decreasing octahedral stress cause stiffening of the material. Thus, k_2 and k_3 are expected to be greater than and less than zero, respectively (NCHRP, 2004a).

The model in Equation 2.2 is a derivative of a more general one that is described by the following equation, which includes two additional constants, k_6 and k_7, which must be less than zero, and greater than 1, respectively.

$$M_R = k_1 P_a \left(\frac{\theta - 3k_6}{P_a}\right)^{k2} \left(\frac{\tau_{oct}}{P_a} + k_7\right)^{k_3} \qquad \text{(Eq. 2.3)}$$

As documented in NCHRP 1-28A (2003), which analyzed 14 different constitutive models for predicting M_r values from tests performed on a range of unbound materials, this model was found to provide the overall best goodness of fit statistics. While the two additional parameters, k_6 and k_7, increase the accuracy of the model, the simplified model in Equation 2.2 which assumes $k_6 = 0$ and $k_7 = 1$, has been adopted in the *Mechanistic Empirical Pavement Design Guide* for unbound aggregate materials, and is more commonly used.

Level 2 of design is based on correlations of M_r with soil index and strength properties such as CBR (California Bearing Ratio). Level 2 of design is used when resources or testing equipment are not available for resilient modulus determination as required in Level 1. The following empirical equation, which comes from the from the UK Transportation Research Laboratory (TRL) relates M_r to CBR:

$$M_r = 2{,}555(CBR)^{0.64} \qquad \text{(Eq. 2.4)}$$

Other soil properties used in Level 2 in correlations with the resilient modulus are PI (plasticity index), DCP (dynamic cone penetrometer) index, P200 (percent passing no. 200 sieve). In the case of PI and DCP index, there is no direct relationship with M_r. Instead, PI and DCP index are first correlated to CBR (see Figure 2.4), which is in turn correlated with M_r. A summary of the empirical correlations used in Level 2 of design is presented in Figure 2.4. PI is used in M_r correlations of coarse-grained soils that contain more than 12% fines and exhibit some plasticity. For clean granular materials (PI = 0), M_r is correlated to D_{60} (NCHRP, 2004b).

Level 3 of design requires the input of a single M_r value that represents the entire foundation. Usually these are default values that come from local agency historical records. Recommended values of M_r for a wide range of unbound granular and subgrade materials are provided in the *MEDPG Manual of Practice* (AASHTO, 2020). M_r values are in the 16,000–40,000 psi (110–276 MPa) range for granular materials (A-1-a to A-2-7 classification) and vary between 8,000 and 16,500 psi (55–114 MPa) for fine grained materials (A-3-a to A-7-6 classification). For coarse materials, current practice in Indiana most often relies on a fixed (Level 3) input value (30,000 psi (207 MPa)) for a

Strength/Index Property	Model	Comments	Test Standard
CBR	$M_r = 2555(CBR)^{0.64}$ (TRL) Mr, psi	CBR = California Bearing Ratio, percent	AASHTO T193, "The California Bearing Ratio"
R-value	$M_r = 1155 + 555R$ (*20*) Mr, psi	R = R-value	AASHTO T190, "Resistance R-Value and Expansion Pressure of Compacted Soils"
AASHTO layer coefficient	$M_r = 30000\left(\frac{a_i}{0.14}\right)$ (*20*) Mr, psi	a_i = AASHTO layer coefficient	AASHTO Guide for the Design of Pavement Structures
PI and gradation*	$CBR = \frac{75}{1+0.728(wPI)}$ (see Appendix CC)	wPI = P200*PI P200= percent passing No. 200 sieve size PI = plasticity index, percent	AASHTO T27. "Sieve Analysis of Coarse and Fine Aggregates" AASHTO T90, "Determining the Plastic Limit and Plasticity Index of Soils"
DCP*	$CBR = \frac{292}{DCP^{1.12}}$	CBR = California Bearing Ratio, percent DCP =DCP index, mm/blow	ASTM D 6951, "Standard Test Method for Use of the Dynamic Cone Penetrometer in Shallow Pavement Applications"

Figure 2.4 Examples of empirical correlations of M_r with index and strength soil properties used in Level 2 of design (NCHRP, 2004b).

material such as the #53 aggregate extensively used as a separator/subbase layer in Indiana).

2.2.4 Resilient Modulus Data for Granular Materials Meeting INDOT No. 53 Specifications

Several studies in literature have investigated the resilient modulus of aggregates. As part of this project, resilient modulus data from laboratory tests performed on 58 different materials from six independent studies conducted in Kentucky (Hopkins et al., 2007), North Carolina (Chow et al., 2014), Oklahoma (Hossain et al., 2015), Nevada (Hajj et al., 2018), Utah (Jackson, 2015), and Alaska (Li et al., 2011) were compiled. As shown in Figure 2.5, these materials, which are herein referred using a symbol that includes the abbreviation for the state of origin and a sequential number (e.g., KY-1), meet INDOT No. 53 particle size distribution specifications. The objective of this review was to generate a database of values of M_r and of the universal model k regression coefficients for materials with characteristics similar to INDOT No. 53. Table 2.2 summarizes key information for each of these studies, including the number of materials tested, gradation and compaction characteristics (maximum dry density, water content, method of compaction) and, when available, characteristics (water content and dry density) of the specimens tested. For all materials in Table 2.2, regression analyses were performed to derive the k_1, k_2, k_3 coefficients appearing in the universal model.

Additional data were retrieved from a 2002 FWHA report (Yau & Von Quintus, 2002), which compiles laboratory data for the over 2000 unbound aggregate materials and soils tested as part of the Long-Term Pavement Performance Program. All resilient modulus data in this study were derived from laboratory cyclic triaxial tests performed following AASHTO-T307 (AASHTO, 2021a), which recommends 200 conditioning loading cycles followed by 16 loading stages consisting of 100 loading cycles each. The 423 sets of data pertaining to unbound aggregate base and subbase materials were extracted from the results included in the 2002 FWHA report and added to the database for this project. The FWHA report provides statistical data on the k parameters for these 423 materials. Note that the FHWA report provides only the k-values determined from nonlinear regression analyses of the M_r data, but not the original M_r data.

Examples of the variation of M_r with confining stress and deviatoric stress are presented in Figure 2.6 for 12 of the materials in the database generated. While this data pertains to tests conducted at a single confining stress (10 psi ~ 69 kPa–Figure 2.6b) and a single value of deviatoric stress (15 psi ~ 103 kPa–Figure 2.6a), similar trends are observed for other loading conditions. The figures highlight how unbound aggregate materials having similar gradation and compaction characteristics can exhibit a broad range of resilient modulus values under the same loading conditions.

Finally, Figure 2.7a–c present box whisker plots for parameters k_1, k_2, and k_3 for the universal model. Each figure contains two plots, one pertains to values obtained best fitting the data from the six sources shown in Table 2.2 (database compiled in this study); the second shows the values reported in the 2002 FHWA report. Tables summarizing key statistical indicators for each of the fitting parameters are included with each figure. In general, the values from the FHWA report show less dispersion than those for the database compiled for this project (compare ranges and COV). Overall, these plots and the associated statistics highlight the broad range in the values that the fitting parameters k_1, k_2, and k_3 can attain, even for materials of very similar gradation. As k_1 reflects differences in particle characteristics and in their packing, a wide range for this parameter may be

TABLE 2.2
Summary of Gradation, Compaction, and Specimen Characteristics of the Database Materials

		Gradation			Compaction Characteristics			Specimen Characteristics	
Symbol	Reference	Passing No. 200 (%)	D_{50} (mm)	Cu	Max Dry Density (pcf)	Optimum Water Content (%)	Method of Compaction	Dry Density (pcf)	w (%)
KY	Hopkins et al. (2007)	0.00–13.00	3.50–9.52	51.67–142.22	142.50–144.80	5.50–6.90	Shaker Table, Standard Proctor Test: Method D	128.50–140.90	3.5–4.9
NC	Chow et al. (2014)	8.00	6.00	90	131.30–153.50	4.20–7.40	Standard Proctor Test: Method A	131.60–159.50	3.9–7.4
OK	Hossain et al. (2015)	4.80–6.30	6.00–10.4	52.78–123.08	133.00–149.00	4.60–7.50			
AK	Li et al. (2011)	6.00–10.00	4.71–5.00	34.44–88.00	146.10–156.80	5.20–6.00	Impact Compaction Method	145.16–156.83	5.2–6.3
UT	Jackson (2015)	4.80–10.20	3.50–5.20	18.52–92.86	137.40–142.20	5.40–6.60			
NV	Hajj et al. (2018)	5.30–10.00	3.2–8.00	31.25–140.0	129.70–147.50	3.50–8.40	Standard Proctor Test: Method A, D		

expected. However, k_2 and especially k_3 also show significant variation. For k_3, several studies generated physically implausible positive values.

2.3 Permanent Deformation

2.3.1 Significance

As discussed in Section 2.2.2, individual soil grains tend to rearrange themselves into denser configurations in response to applied compressive stresses. The compressive stresses induce straining of the soil matrix that involves frictional slip between grains and compression at grain contacts. Upon removal of the compressive stress, the soil matrix will attempt to revert to its original loose configuration. However, the matrix will only experience a partial rebound (i.e., resilient strain) since a portion of the energy input from the compressive stress will have been dissipated through individual soil grain rearrangement. The difference in soil matrix configurations before and after compression is therefore an irrecoverable or so-called permanent strain. Repeated permanent strains accumulate as permanent deformations that manifest in flexible pavements as ruts, which lead to pavement structural failures and increased potential for hydroplaning.

The *Indiana Design Manual* requires that MEPDG predicted pavement rutting (i.e., total pavement permanent deformation) for new and rehabilitation hot mix asphalt (HMA) pavements not exceed 0.75 in. Total pavement permanent deformation equals the summation of permanent deformations from each pavement layer (e.g., asphalt surface course, aggregate base, subgrade, etc.). The MEPDG software predicts permanent deformations of aggregate base and subgrade layers using Equation 2.5 from Tseng and Lytton (1989).

$$\delta_p = \beta_{s_1} k_1 \left(\frac{\varepsilon_0}{\varepsilon_r}\right) e^{-\left(\frac{\rho}{N}\right)^{\beta}} \varepsilon_v h \qquad \text{(Eq. 2.5)}$$

where,

δ_p = permanent deformation for the layer (in.),
N = number of traffic loading repetitions,
ε_o, β, and ρ =material properties,
ε_r = resilient strain from laboratory testing used to determine material properties—ε_o, β, and ρ,
ε_v = average computed vertical resilient strain in the layer,
h = layer thickness (in.),
β_{s1} = INDOT calibration factor (equals 0.12), and
k_1 = national calibration factor (equals 0.965 for aggregate bases and coarse-grained soils, 0.635 for sand soils and 0.675 for fine-grained soil according to AASHTO (2020)).

MEPDG users do not input values for ε_o, β, ρ, and ε_r, rather the software computes the values using empirical expressions (Equation 2.6–Equation 2.10) developed from NCHRP Project 1-37A (NCHRP, 2004b).

$$w = 51.712\left[\left(\frac{M_r}{2{,}555}\right)^{\frac{1}{0.64}}\right]^{-0.3586\ \mathrm{GWT}^{0.1192}} \qquad \text{(Eq. 2.6)}$$

$$\log\beta = -0.61119 - 0.017638w \qquad \text{(Eq. 2.7)}$$

$$C_o = \ln\left(\frac{a_1 {M_r}^{b_1}}{a_9 {M_r}^{b_9}}\right) \qquad \text{(Eq. 2.8)}$$

$$\rho = 10^9\left[\frac{C_o}{1-(10^9)^{\beta}}\right]^{\frac{1}{\beta}} \qquad \text{(Eq. 2.9)}$$

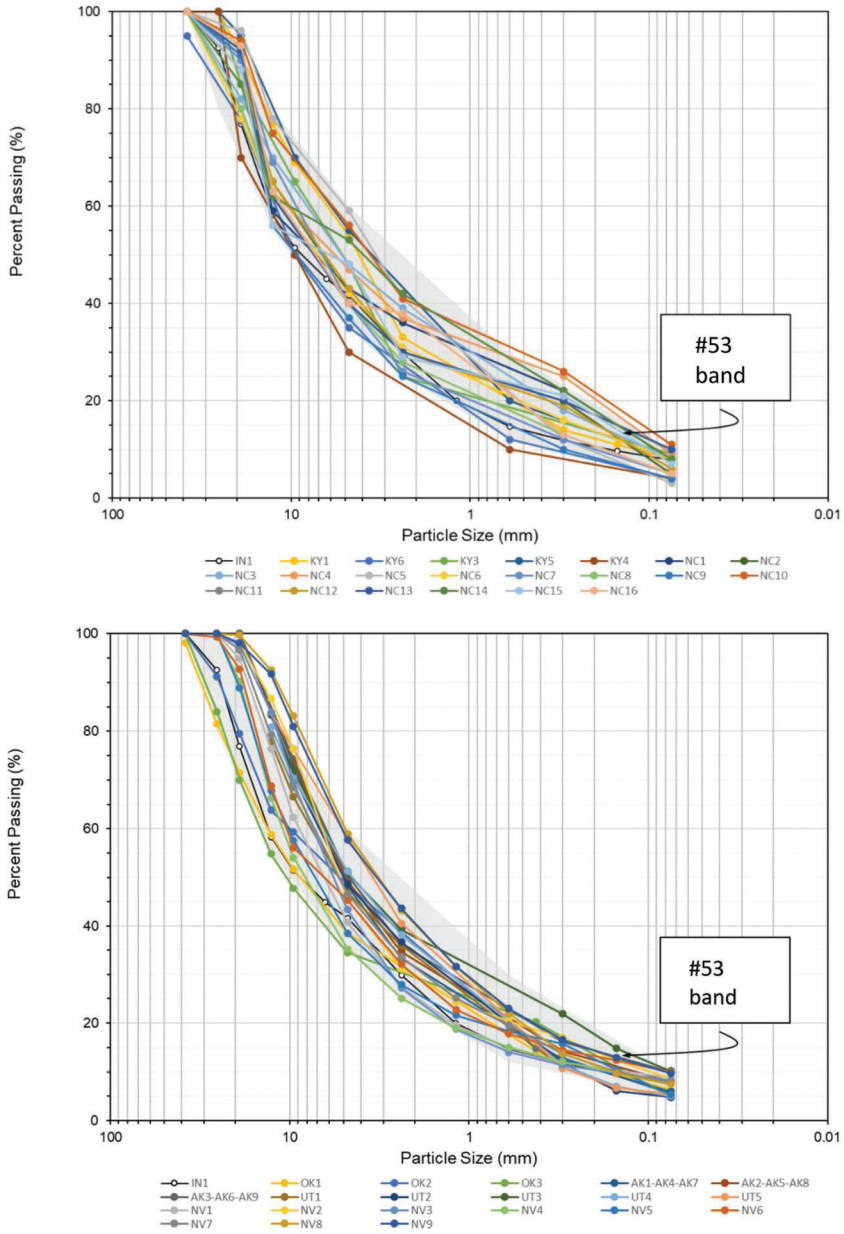

Figure 2.5 Particle size distributions of materials included in the database and reference gradation band for Indiana #53.

$$\log\left(\frac{\varepsilon_o}{\varepsilon_r}\right) = \frac{1}{2}\left\{a_1 \exp\left(\rho^{\beta}\right) M_r{}^{b_1} + a_9 \exp\left[\left(\frac{\rho}{10^9}\right)^{\beta}\right] M_r{}^{b_9}\right\} \qquad \text{(Eq. 2.10)}$$

where,

w = moisture content (%),
M_r = layer resilient modulus (psi),
GWT = groundwater table depth (ft),
a_1 = 0.15,
b_1 = 0.0,
a_9 = 20.2, and
b_9 = 0.0.

2.3.2 Factors Affecting Permanent Deformation

Permanent deformation is largely the function of applied loading conditions and soil shear strength. The following paragraphs provide a general overview of these factors, though a more comprehensive discussion can be found in Tseng and Lytton (1989) and in Thom (2014).

Loading Magnitude: Greater magnitude loadings induce higher amounts of strains in soils. Since permanent strain is proportional to the induced strain, it is expected for greater magnitude loadings to result in greater amounts of permanent deformation. Indeed, a heavier loading will contribute a greater amount of

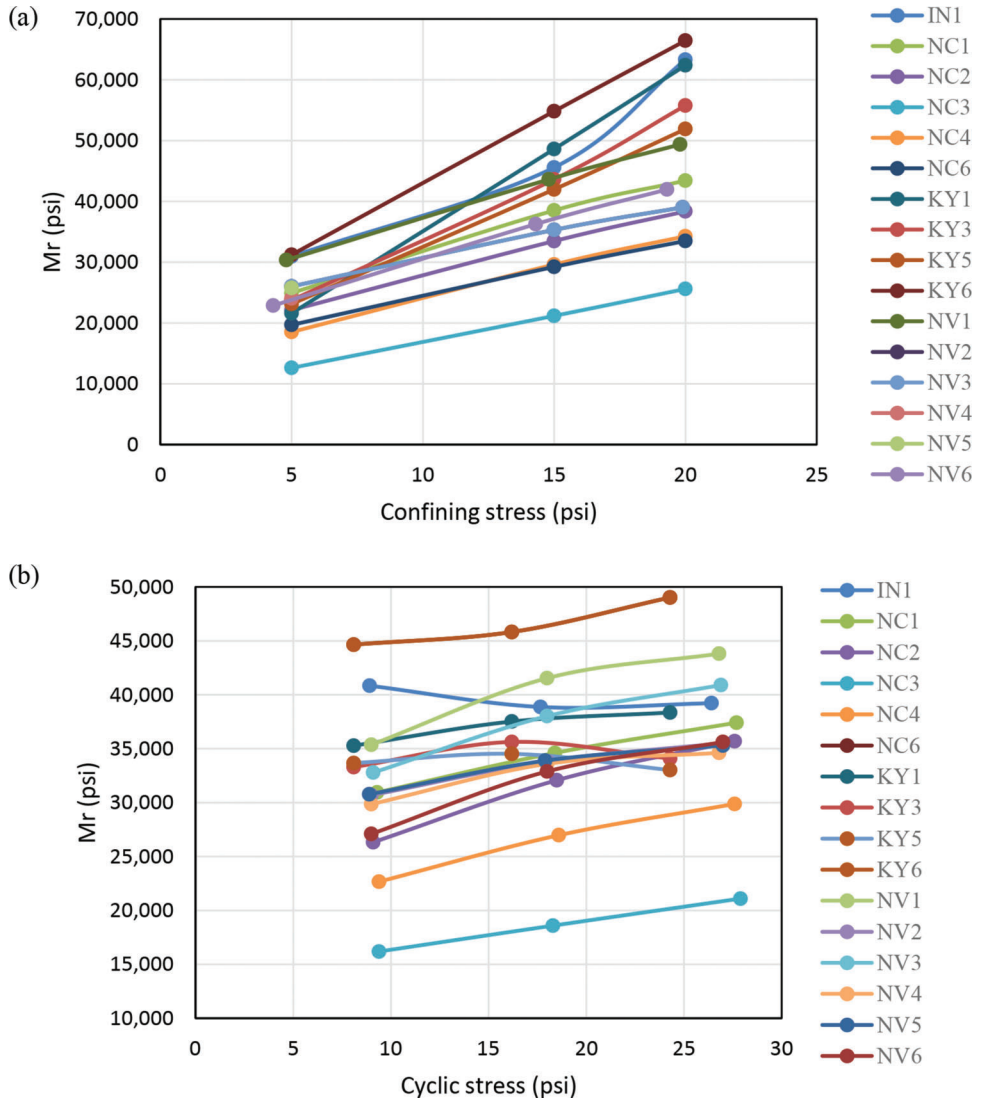

Figure 2.6 Variation of M_r with (a) confining stress (15 psi deviatoric stress), and (b) deviatoric stress (10 psi confining stress) for aggregates that meet INDOT No. 53 particle size distribution specifications.

energy that can more easily induce interparticle slip within a soil matrix.

Number of Loading Cycles: Total permanent deformation tends to increase logarithmically with an increasing number of loading cycles. With each additional loading cycle individual grains within a soil matrix become more resistant to interparticle slip that causes permanent strain. As a result, the amount of permanent deformation per loading cycle will decrease to a limit of zero. This limit is referred to as the "shakedown limit" where plastic strain ceases altogether (Thom, 2014).

Shear Strength: Because permanent strain is largely the result of frictional slip across soil grains, soils with greater shear strength are more resistant to accumulating permanent deformations. Therefore, stronger soils are expected to experience lowers amounts of permanent deformation. Soil shear strength is a function of several other factors including soil type (granular versus fine-grained), confining stress, stress history, moisture content, density, particle angularity.

2.4 Interpretation of Plate Load Tests

2.4.1 Boussinesq Solution

Conventional interpretation of the plate load test makes use of Boussinesq's (1885) half space solution (Equation 2.1) for evaluating the elastic modulus of the tested soil material, which assumes homogeneous isotropic linear-elastic material behavior.

$$E = \frac{(1-v^2)\cdot q \cdot r}{\delta_r}\cdot f \qquad \text{(Eq. 2.11)}$$

where,

E = elastic modulus,

δ_r = resilient (elastic) deflection of the plate,

(a)

k_1		
Statistical Indicators	**Database** *in Table 2.2*	**FHWA**
Maximum	4,368.6	1,847.4
Quartile	1,287.0	1,049.8
Median	942.2	852.7
Quartile	747.6	677.8
Minimum	511.0	280.9
Mean	1,131.9	873.2
Standard Deviation	642.0	272.6
COV	56.7%	31.2%
N	60	423

(b)

k_2		
Statistical Indicators	**Database** *in Table 2.2*	**FHWA**
Maximum	1.718	1.062
Quartile	1.188	0.7
Median	0.712	0.628
Quartile	0.543	0.565
Minimum	0.138	0.174
Mean	0.837	0.626
Standard Deviation	0.413	0.133
COV (%)	49.3	21.2
N	60	423

(c)

k_3		
Statistical Indicators	**Database** *in Table 2.2*	**FHWA**
Maximum	0.89	0
Quartile	0.077	0
Median	-0.067	-0.129
Quartile	-2.71	-0.261
Minimum	-4.606	-2.898
Mean	-0.975	-0.170
Standard Deviation	1.687	0.215
COV (%)	173.0	126.5
N	60	423

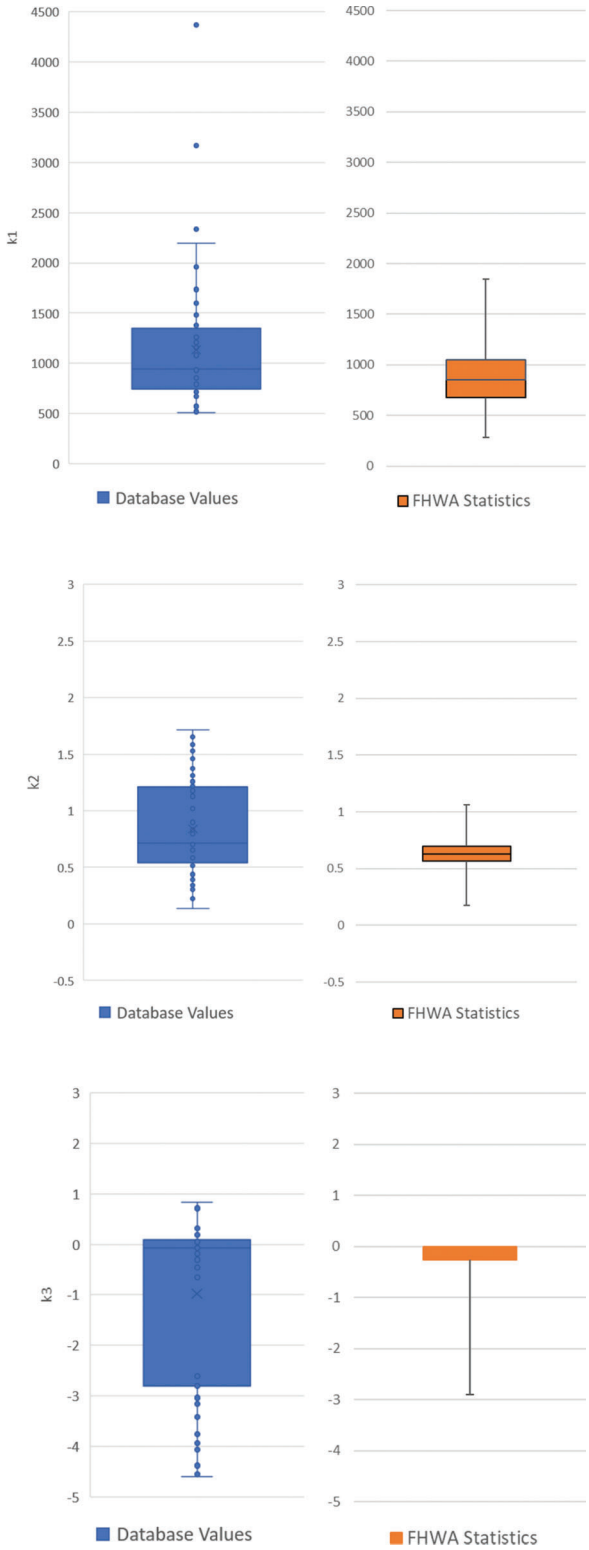

Figure 2.7 Statistics for universal model parameters (a) k_1, (b) k_2, and (c) k_3 for aggregates that meet INDOT No. 53 particle size distribution specifications.

ν = Poisson's ratio,
q = applied contact stress,
r = radius of bearing load plate, and
f = shape factor.

The value of the shape factor f that appears in Equation 2.11 is intended to reflect the stress distribution beneath the plate. The earliest definition of the shape factor assumed uniform distribution of stress

beneath the plate, which corresponds to f = 2 (Timoshenko & Goodier, 1970). Ullitdz (1987) subsequently proposed that the distribution of the stress under a loaded rigid plate has a parabolic shape, which varies depending on the properties of the underlying material: parabolic and inverse parabolic, for a plate resting on a cohesionless and cohesive soil, respectively. These stress distributions correspond to values of the shape factor of 8/3 and $\pi/2$, respectively.

Use of the Boussinesq solution for interpreting plate load test data is founded on a number of assumptions (material homogeneity, isotropic linear-elastic response) that may not be realistic particularly in the case of tests on layered pavement systems. Additional uncertainty is associated with the selection of values of both the Poisson ratio (ν) and the shape factor. The subsequent sections provide a brief review of the effect of Poisson ratio and plate stiffness and discuss the impact that consideration of material non-homogeneity and anisotropy have on the interpretation of plate load test data based on previous work.

2.4.2 Factors Affecting Interpretation of Plate Load Tests

2.4.2.1 Influence of Poisson's ratio. Use of the Boussinesq equation (Equation 2.11) requires an input of the soil's Poisson ratio, ν. When using plate load tests for pavement design, a value of 0.4 is commonly used for both subbase and subgrade layers (White & Vennapusa, 2017; White et al., 2016, 2019). However, the Poisson ratio is a complex soil property that depends on a number of factors including confining pressure, deviatoric stress and soil physical properties, and values reported in the literature fall in a broad range (0.1–1, e.g., Brown & Hyde, 1975; LeKarp et al., 2000, Morgan, 1966). Isotropic elasticity theory provides an upper bound of 0.5 for the Poisson ratio value used in analyses, as the increase in volume associated with $\nu > 0.5$ does not comply with elasticity theory. Nevertheless, even a variation of this property in a narrower range has a significant impact. For example, keeping all other parameters constant, as ν varies between 0.2 and 0.5, the factor $(1\text{-}\nu^2)$ accounts for almost a 30% difference in the predicted modulus.

2.4.2.2 Influence of plate stiffness. A key assumption involved in the interpretation of plate load test data is related to the stiffness of the plate. Flexible plates, such as rubber tires, generate a uniform pressure distribution on the loaded surface. However, steel plates that are typically used in plate load tests are better modeled as rigid. Given the high stiffness of the material constituent of the plate, a large portion of the structural capacity of the system comes from the plate itself (Yoder & Witczak, 1975). Moreover, variations in plate rigidity bring about differences in the distribution of stresses beneath the loaded area and as a result, in the soil settlement.

Boussinesq's theory for flexible plates was further extended to rigid plates by Burmister, and the respective equations, here expressed in terms of settlement, are shown in Equations 2.12 and 2.13.

$$\delta_r = \frac{2(1-\nu^2)qr}{E} \text{ (flexible plate)} \qquad \text{(Eq. 2.12)}$$

$$\delta_r = \frac{\pi(1-\nu^2)qr}{2E} \text{ (rigid plate)} \qquad \text{(Eq. 2.13)}$$

where,
- E = elastic modulus of the material,
- r = radius of the loaded bearing area,
- q = the applied load at the surface,
- ν = Poisson's ratio of the soil material, and
- δ_r = deflection at the axis of the load.

Based on these equations, the predicted settlement under a perfectly rigid plate is approximately 0.8 times that predicted for the same conditions under a perfectly flexible plate.

Several authors in the literature have examined the influence of plate (or foundation) stiffness (Arnold et al., 2010; Brown, 1969; Horikoshi & Randolph, 1997; Lemmen et al., 2017; Poulos, 1968) on settlement. An illustration of this effect is provided by the work of Mayne and Poulos (1999), who incorporate a rigidity correction factor I_F in the expression used for calculating the settlement of foundations. I_F depends on the modulus and geometry of the plate, as well as on the modulus of the soil, through a plate flexibility factor K_f defined as shown in Equation 2.14.

$$K_f = \left(\frac{E_{plate}}{E_{soil}}\right)\left(\frac{2t}{d}\right)^3 \qquad \text{(Eq. 2.14)}$$

where,
- E_{plate} = elastic modulus of the plate material,
- E_{soil} = elastic modulus of the soil located beneath the plate (at a depth equal to the radius of the plate),
- d = diameter of the plate, and
- t = thickness of the plate.

This formula was generated as an approximation after Brown (1969), who used finite-element analyses to investigate the effect of plate rigidity. The relationship between I_F and K_f is shown in Figure 2.8. The figure shows both the original results from Brown (1969), as well as the approximate expression by Mayne and Poulos (1999). The rigidity correction factor I_F is observed to vary between a minimum value of $\frac{\pi}{4}$ for low values of K_f and a maximum value of 1 (high K_f), which correspond to ideal rigid and flexible conditions, respectively.

Similar to what is seen in the solutions provided by Burmister and Bousinessq (Equation 2.12 and Equation 2.13), the settlement predicted under a perfectly rigid plate is approximately 0.8 times that predicted under a perfectly flexible plate. Note that for a rigid circular

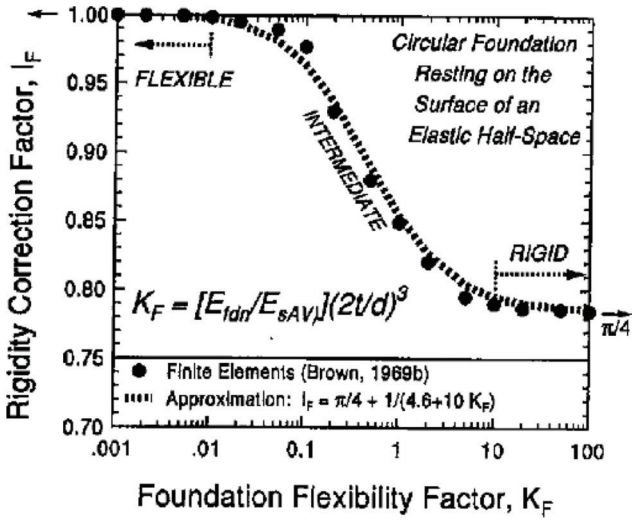

Figure 2.8 Effect of plate rigidity on the settlement of a vertically loaded circular foundation (Mayne & Poulos, 1999).

plate the settlements calculated at the center, corner and edge of the plate are equal, while for a flexible plate the settlement calculated at the center of the plate is 3/2 the settlement calculated at the edge.

2.4.2.3 Influence of material non-homogeneity. As discussed previously, the use of Boussinesq's equation is based on a homogeneous infinite half space. The assumption of material homogeneity is questionable in the case of pavement systems, which consist of layers that have distinct mechanical properties. This was first recognized by Burmister (1945), who developed solutions based on elastic, isotropic material response for calculating the settlement of a two-layer pavement system. The solutions account for two different interface conditions: full continuity (i.e., no slippage) between the two layers or zero shear stress at the interface. For the first interface condition, the solution by Burmister (1945) is shown in Equation 2.15.

$$\delta_r = \frac{1.5\,qr}{E_2} F\left[\frac{h}{r}, \frac{E_1}{E_2}\right] = \frac{1.5\,qr}{E_2} F_w \qquad \text{(Eq. 2.15)}$$

where,

E_1, E_2 = elastic moduli of top and bottom layer, respectively,

r = radius of the loaded bearing area,

q = the applied load at the surface,

h = thickness of top pavement layer, and

F_w = settlement coefficient (function of $\frac{h}{r}$ and $\frac{E_1}{E_2}$).

Influence curves for determining F_w for the case of a stiffer upper layer are shown in Figure 2.9. The figure shows that, as expected, relative to the homogeneous case (constant value of $E = E_2$), the presence of a top stiffer layer reduces the predicted settlement. The greater the contrast in the values of the elastic modulus between the two layers, the more significant the impact. For a given value of $\frac{E_1}{E_2}$, the settlement coefficient decreases with $\frac{h}{r}$. For example, for $\frac{E_1}{E_2} = 10$ and h > r, F_w falls below 0.5. This implies that for such conditions the assumption of homogeneity would lead to over-predict the settlement by 50% or more (or, alternatively, underpredict the modulus of the bottom layer soil from the measured surface settlement by the same amount).

Through the use of finite element analyses, a number of authors, starting with Clough and Rashid (1965) and Wilson (1963), have further investigated the role played by stratification and material non-homogeneity. This issue is further examined in Chapter 4 of this report.

While Equation 2.15 quantifies the effect on plate settlement, the presence of stratification clearly also influences the stress distribution in the loaded soil (Burmister, 1945). This effect can be examined using the KENLAYER software developed for the design of flexible pavements (Huang, 2004). The software, which incorporates Burmister's solution for an elastic multi-layered system under a circular load, assumes two boundary conditions (contact stress = q, surface free of shear stress) and four continuity conditions (continuity of vertical stress, vertical displacement, shear stress and radial displacement through each interface), and allows computation of stress and deformations throughout the system (Huang, 2004). Figure 2.10 shows the variation of the depth of influence (based on 90% attenuation under the centerline of the plate) for a two-layer model in which the stiffness of the top layer (with thickness equal to ~1.5 times the radius of the loading plate) was varied, so that the layer modulus ratio R $\left(R = \frac{E_1}{E_2} = \frac{E_{top}}{E_{bottom}}\right)$ ranged between 0.01 and 50.

As illustrated in Figure 2.10, when the top layer is underlain by a stiffer layer (R < 1), the influence depth does not vary significantly even as R changes by two orders of magnitude (0.01 to 1). In the case of a weaker underlying layer, instead, the effect of R is significant, with the depth of influence markedly decreasing with increasing value of R. For a sufficiently high value of R, it is seen to not extend into the underlying softer layer.

Overall, these results demonstrate that neglecting material non-homogeneity in the interpretation of plate load test data can lead to inaccurate predictions of moduli.

2.4.2.4 Influence of material anisotropy. Another significant assumption incorporated in the evaluation of elastic modulus from field data is that of isotropic material behavior for all layers. However, the anisotropic properties of soils and in particular of granular materials used for subbase and base layers have been long documented in the literature. Casagrande and Carillo (1944) were some of the earliest authors to distinguish two forms of anisotropy in granular materials: inherent and induced anisotropy. The first

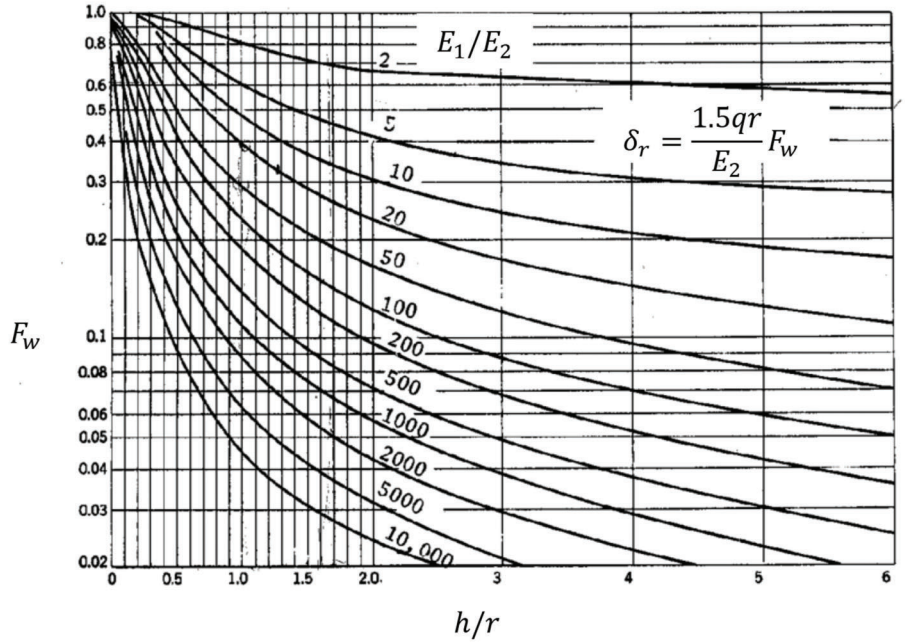

Figure 2.9 Influence curves of settlement coefficient F_w for a two-layer system (Burmister, 1945).

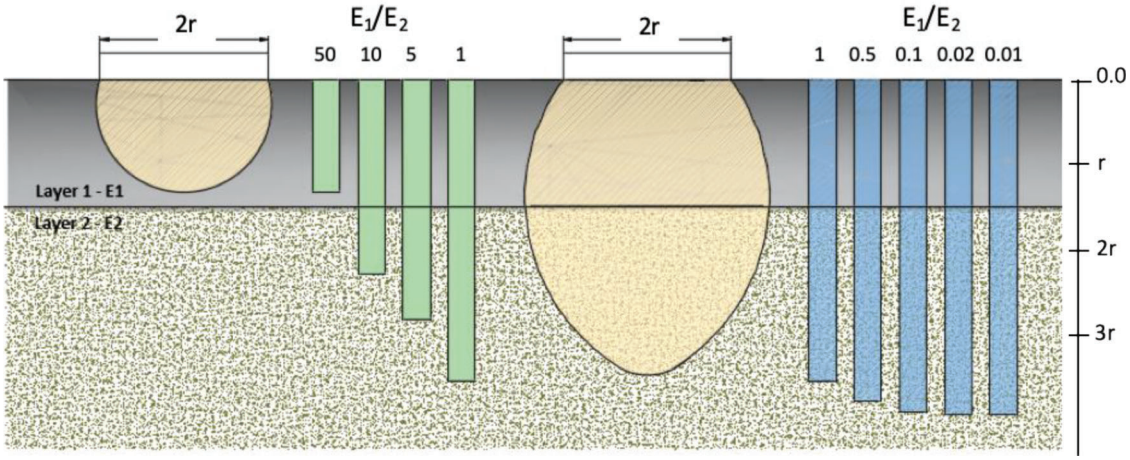

Figure 2.10 Variation of influence depth for different values of layer modulus ratio (R = E1/E2).

comes as a result of the deposition of the material, while the latter is a result of loading. While of relevance to this work is the effect of anisotropy on the stress-strain behavior, other properties such as permeability and thermal and electrical conductivity are also known to be affected (e.g., Kuhn et al., 2015).

The sources of anisotropy during loading come from the mechanisms of load transfer in granular media. Unlike continuous media, the distribution of stresses in granular media is not uniform but concentrated along continuous chains of particles (Tutumluer, 2009). Given this mechanism of load transfer, granular materials can distribute the load by means of compression and shear forces between aggregates. For this reason, there is a preferred orientation of particle contacts along the direction of compressional loading. This directional dependency of the contacts leads to a directional dependency of the material's stiffness (Gu et al., 2020).

Some of the earlier studies on the influence of anisotropy on stress and strain field produced by the application of a surface load include the work by Koning (1957), Barden (1963), and Hanna (1965).

The work by Barden (1963) quantifies the effect of the degree of anisotropy of a homogeneous medium, as measured by the modulus anisotropy ratio n $\left(n = \frac{E_h}{E_v}\right)$, on the vertical stress produced by a concentrated load applied at the surface. The results of this work are summarized in Figure 2.11 for n

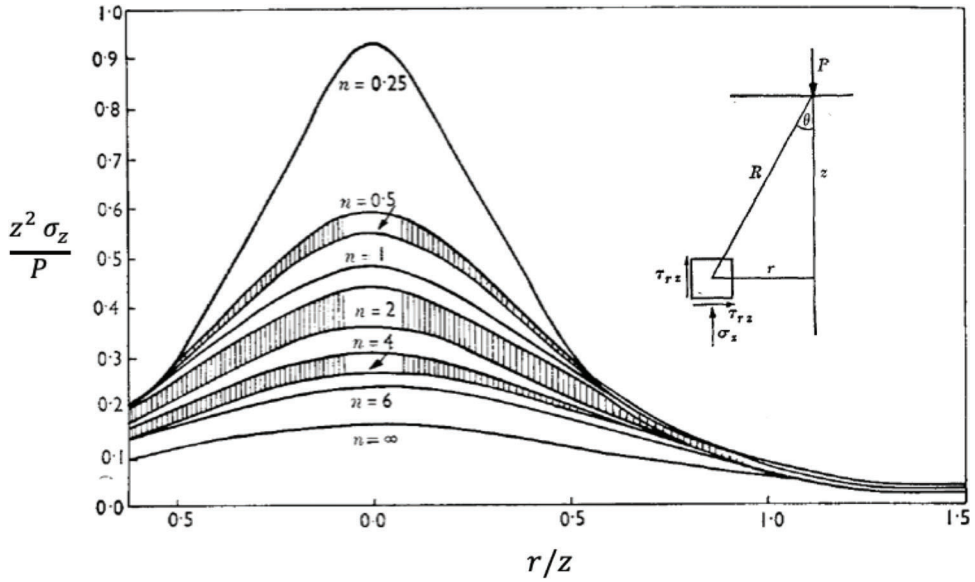

Figure 2.11 Variation of vertical stress with distance from a concentrated load applied at the surface (adapted from Barden, 1963).

varying from 0.25 to infinity, with the bands for each n represent variations in the values of the Poisson ratio. The figure demonstrates that the anisotropy ratio of the loaded material significantly influences its load spreading capacity. This, as a result, would affect the deformations produced by the applied load. For example, focusing on the vertical stress generated directly below the applied load, it is seen that at any given depth, as n varies between 0.25 and 6, the vertical stress increase is, respectively, almost twice and less than half of the value derived assuming isotropy.

As the work presented in this report was focused on the interpretation of plate load tests conducted on compacted aggregate layers, the anisotropy ratio of these materials is of particular interest. A number of laboratory studies have investigated the anisotropic properties of aggregates and other granular materials. Some key studies are summarized in Table 2.3. The last column in this table summarizes the values of n derived from each study. These are found to vary within a broad range, from less than 0.1 to almost 2. Of significance is the study by Bellotti et al. (1996) based on seismic wave propagation measurements. While conduced on a silty sand, the study indicates a relationship between the measured anisotropy ratio, n, and the consolidation stress ratio K ($= \sigma'_h/\sigma'_v$). This is relevant to compacted granular materials in which higher values of K may be developed as a result of compaction.

The first row in Table 2.3 refers to a publication by Tutumluer et al. (2016) which includes data for 113 aggregate materials obtained from repeated triaxial tests performed using the UI-FastCell that allows measurement of the resilient modulus in both the horizontal and vertical direction. As shown in the table, values of n derived from this study alone varied from 0.08 to 1.51. By testing a broad range of materials, Tutumluer et al. (2016) were also able to identify the effect of various parameters on n. They show that the anisotropy modulus ratio n increases with increasing compaction effort, fines content, particle angularity and particle texture roughness. The results presented by Tutumluer et al. (2016) on the influence of aggregate texture and angularity on n are in accordance with the results presented by Ashtiani and Little (2009) based on tests on 56 granular aggregate samples (Figure 2.12).

The effect of the fines content is illustrated by the resilient modulus data presented in Figure 2.13. This data pertain to tests performed for a range of confining and deviatoric stresses on crushed gravel with fines content of 8% and 16%. For the gravel with 8% fines, the horizontal modulus data fall, for the most part, below the corresponding vertical modulus data, reflecting values of the anisotropy ratio, n, smaller than 1. In contrast, with 16% fines the horizontal moduli are consistently greater than the vertical moduli for all stress conditions examined, resulting in values of n that exceed 1.

Finally, with regard to the effect of compaction effort, Tutumluer et al. (2016) report that the modulus anisotropy ratio n of two crushed aggregates with 12%–13% fines increased with increasing compaction effort.

The effect of the deviatoric stress level on n is less straightforward. For example, Figure 2.13b shows that for the gravel with 16% fines, the horizontal modulus decreased with increasing deviatoric stress, while the vertical modulus remained constant or decreased slightly, reflecting a reduction in n. Results by Seyhan and Tutumluer (2002) for other aggregate materials show the opposite trend. Seyhan and Tutumluer note that trends of increasing modulus with increasing deviatoric stress are generally associated with good quality materials.

TABLE 2.3
Values of Modulus Anisotropy Ratio (n) Reported in the Literature for Granular Soil Materials

Author	Type of Test	Materials Tested	D_{50} (mm)	Number of Data	Range of n (Eh/Ev)	
Tutumluer et al., 2016	UI-FastCell	Uncrushed gravel Crushed dolomite	2–10	114	Low stress level ($\sigma_d > 69$ kPa)	0.17–1.51
		Limestone Crushed stone			Intermediate stress level ($\sigma_d > 138$ kPa)	0.08–1.33
		Recycled concrete aggregates (RCA)			High stress level ($\sigma_d > 276$ kPa)	0.05–1.32
Adu-Osei et al., 2001	RaTT	Crushed rock (California granite)	–	108	Well-graded materials	0.15–1.28
		Texas crushed limestone			Coarse materials	0.36–0.6
		Rounded pit gravel (Texas gravel)			Fine graded materials	0.156–1.116
		Rounded glacial sandy gravel (Minnesota gravel)				
Seyhan & Tutumluer, 2002	UI-FastCell	Gravel Crushed–stone	–	39	Low/intermediate/high stress level	0.38–1.5
Bellotti et al., 1996	Laboratory seismic tests	Ticino sand	0.55	26	–	0.79–1.9
Jiang et al., 1997	Triaxial compression tests	Sandy gravel	–	36	Isotropic stress states	0.45
	Triaxial cyclic tests		–		Anisotropic stress states	0.28–0.67
Hicher & Chang, 2006	Elastic model based on properties of particles contacts	Toyoura sand, hime gravel, chiba gravel	–	40	Anisotropic stress states	0.45–0.8
			–	–	Isotropic stress states	0.9

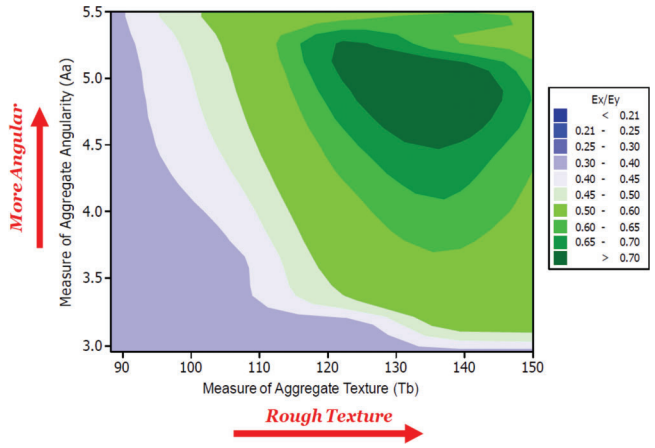

Figure 2.12 Effect of aggregate angularity and texture on the anisotropy ratio n (Ashtiani & Little, 2009).

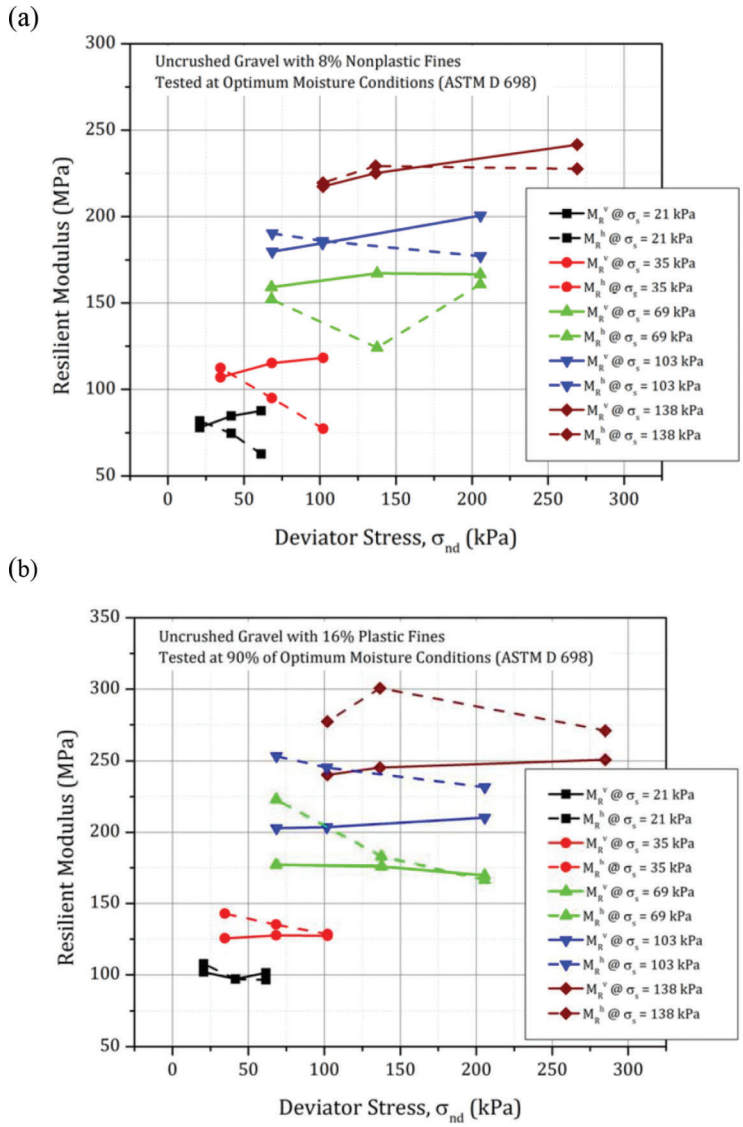

Figure 2.13 Horizontal and vertical resilient moduli of uncrushed gravel material with (a) 8% non-plastic fines, and (b) 16% non-plastic fines (Tutumluer et al., 2016).

3. SITE DESCRIPTION AND PLATE LOAD TESTING PROGRAM

3.1 Introduction

This chapter describes the methods used to construct the aggregate strips (Section 3.2) and testing pit (Section 3.4) where the plate load testing program was conducted, provides an overview of the conditions at the testing locations (Section 3.3), the plate load testing equipment (Section 3.5) and the testing protocols (Section 3.6), and presents examples of the data obtained from the different types of tests performed (Section 3.7).

3.2 S-BRITE Strip Construction and Testing

The plate load testing program was performed at locations on two 60 ft by 20 ft (18 m by 6 m) unbound aggregate test strips (Figure 3.1) constructed at the Purdue University Steel Bridge Research Inspection Training and Engineering Center (S-BRITE), part of Purdue's Center for Aging Infrastructure (CAI) in West Lafayette, IN. The testing strips were constructed during the summer of 2020 as part of a separate JTRP project (SPR-4327 *Control Guidelines for Aggregate Drainage Layers and Evaluation of In Situ Permeability Testing Methods for Aggregates*). This same project involved extensive additional testing of the strips including light weight deflectometer (LWD) and nuclear density tests.

Figure 3.1 identifies the location of the site, where soil conditions under the vegetated organic layer include 3.5 to 6 ft (1.1–1.8 m) of silty or sandy clay underlain by silty or clayey sands. The water table lies approximately 18 ft (5.5 m) below the ground surface (Patriots Engineering and Environmental Inc, 2014).

After removal of the topsoil and excavation of an additional 6″ (15.2 cm) thick layer of the natural soil throughout the site, different procedures were followed for construction of the two strips.

On the northern strip, the aggregate layer was constructed in a single lift (average thickness = 5.5 in (14.0 cm)) on the compacted natural soil, a clayey sand with 48%–49% fines, and average liquid limit and plastic limit of 27.9% and 14.6%, respectively (CS and A-6 classification according to USCS and AASHTO). Target values of water content and dry unit weight were 8.3% and 129.1 pcf (20.1 kN/m^3). Subgrade compaction was performed by an independent contractor (Specialties Company LLC of Indianapolis, IN).

Slurry cement stabilization with a cement application rate of 50.8 lb/yd^2 was performed by the same contractor to a depth of 14 in (35.6 cm) on the footprint of the second southern strip targeting 8% water content and 125.1 pcf (19.6 kN/m^3) dry unit weight. Subgrade compaction and soil stabilization specifications were based on laboratory compaction and unconfined compression tests performed according to INDOT design procedures (INDOT, 2022). Construction of the aggregate layer on the cement treated subgrade was performed in two lifts, with a final average thickness of 8.7 in (22.1 cm).

INDOT #53 aggregate sourced from US Aggregates (Delphi, IN) was selected for both strips. The particle size distribution for this aggregate, which is widely used by INDOT as a pavement subbase layer, is shown in

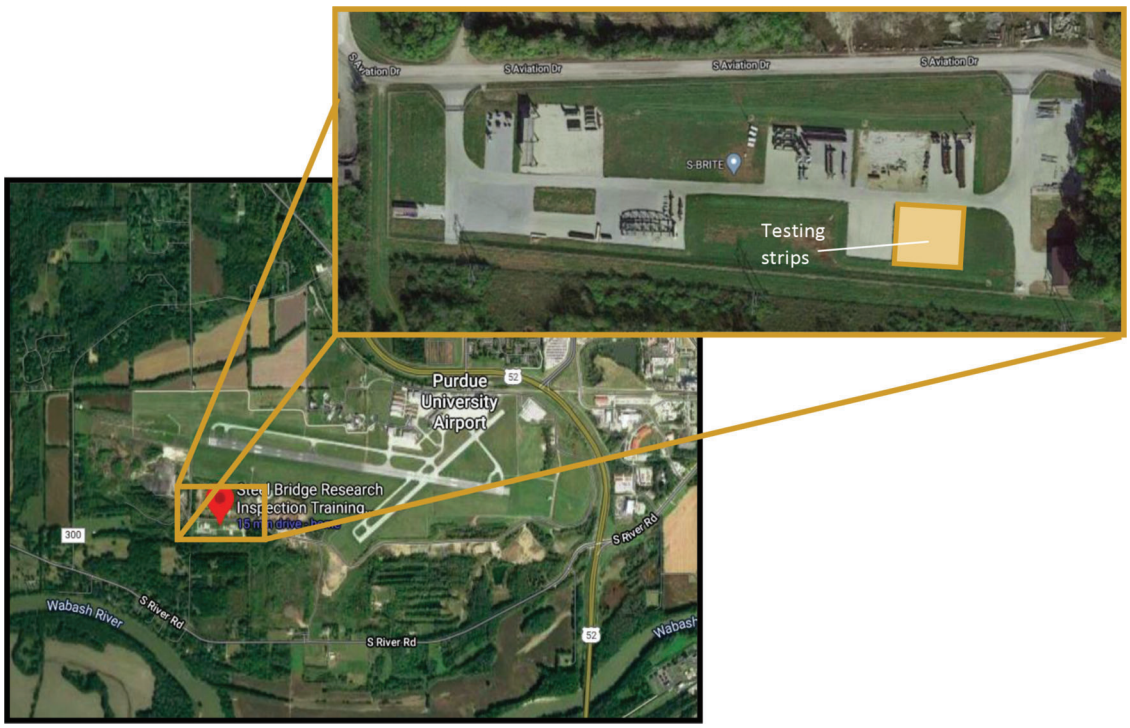

Figure 3.1 Location of the S-BRITE facility in West Lafayette, IN.

Figure 3.2 along with the band that identifies the limits for the Indiana #53 designation. In both strips the aggregate was placed and graded using a loader, and then compacted using a CAT CS44B compactor, following a sequence of 4 static, 4 vibratory (f = 30 Hz) and four additional static passes. To limit segregation of the material, care was placed in mixing the aggregate stockpile.

A grid of perpendicular lines with a uniform spacing of 3 feet (0.9 m) was established for identifying the testing locations on both strips. For each strip, the grid lines parallel to the east-west direction were labeled with numbers from 1–7 (starting from north), while the grid lines parallel to the north-west direction were labeled with letters from A–T (starting from west) as shown in Figure 3.3. Prior to placement of the aggregate, a geotextile (GEOTEX® 601 6 oz nonwoven geotextile fabric manufactured by Propex) was placed on the subgrade on the eastern most side of both strips (overlapping rows P–T on the grid).

Elevation readings at all points on the 3 by 3 ft grid were collected using a rotary laser after each construction stage, allowing determination of the thickness of the individual lifts. Figure 3.4 presents maps of the thickness of the full aggregate subbase layer for the two strips herein referred to as UNT (untreated) and CT (cement treated) strips.

Light weight deflectometer (LWD) and nuclear density (ND) tests were performed at locations on each of the two test strips to determine the in-situ material

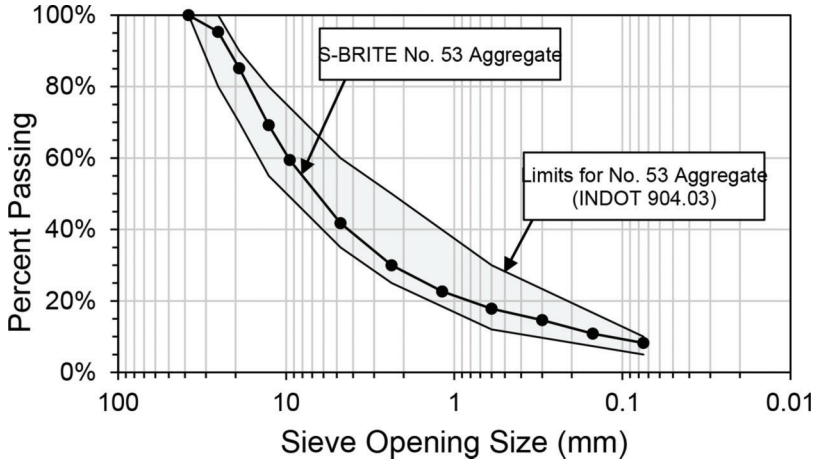

Figure 3.2 Particle size distribution of S-BRITE No. 53 aggregate.

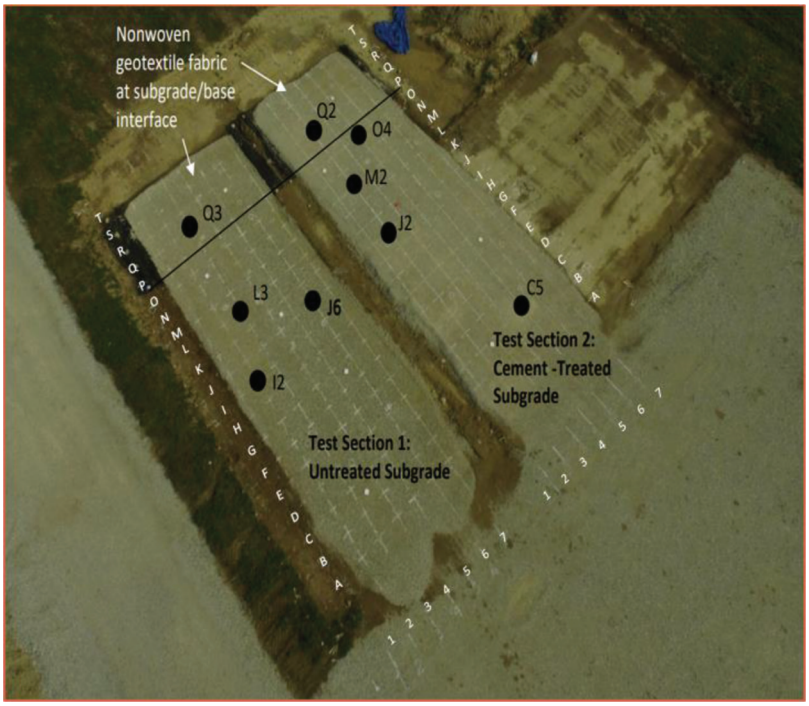

Figure 3.3 Plate load testing locations on S-BRITE strips.

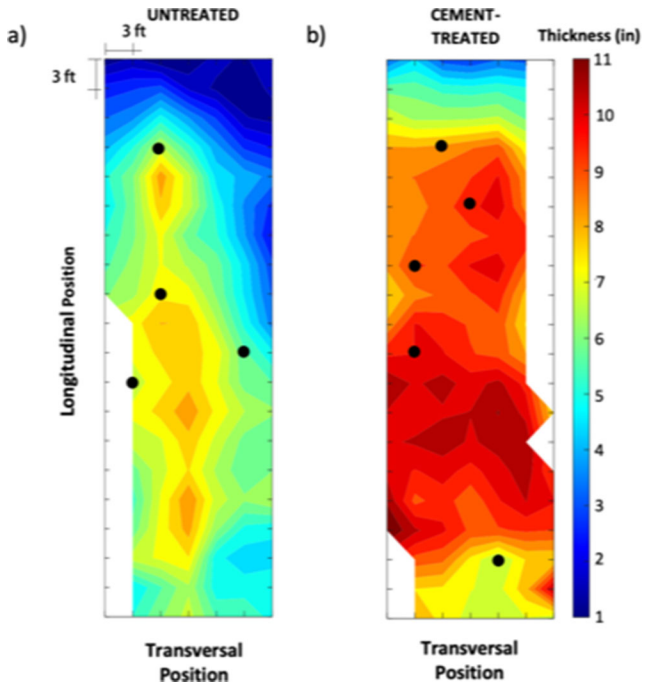

Figure 3.4 Thickness of aggregate subbase layer on (a) UNT, and (b) CT strips (maps based on measurements at grid points; black circles identify plate load testing locations).

characteristics of the layers. LWD tests were performed at all grid points on the two strips (over 125 points on each strip) with both a small (LWD-S: D = 0.150 m, drop height = 0.165 m) and a large (LWD-L: D = 0.300 m, drop height = 0.720 m) platen.

Nuclear density tests were performed only after completion of strip construction at points offset from the grid (39 and 37 locations on the UNT and CT strips, respectively).

The LWD testing procedure followed the ASTM E2583-07 (ASTM, 2020) standard test method for measuring deflections of paved and unpaved surfaces. In this test a mass is dropped from a specific height generating a force pulse which is transmitted by means of a plate resting on the surface of the loaded layer. Depending on the manufacturer, different sensors are used to measure the surface deflection produced by the applied impulse load. LWD tests for this research project were performed using the Zorn ZFG 3.0 light weight deflectometer (www.zorn-instruments.com). With this apparatus, surface deflections are derived by twice integrating readings from the accelerometer built into the loading plate.

While several models are commonly used to transform LWD readings into moduli, in order to reduce the bias created by the assumptions associated with the use of such models, only average deflections are reported in this document.

Nuclear density testing procedures followed the ASTM D6938-17a standard test method for measurement of in-place density and water content of soil by means of nuclear gauges (ASTM, 2017). Nuclear density tests were performed by Earth Exploration (a Terracon Company) of Indianapolis. The equipment used was a Troxler 3430 Nuclear Density Gauge. The direct transmission method, which is the preferred procedure, involves the extension of a probe through the base of a nuclear gauge into a vertical hole to a specific depth. The nuclear gage system includes gamma and neutron radiation sources and detectors which can measure the radiation and quantify the total (wet) density and moisture content of the soil. The in-situ density of the soil is calculated using the detected rate of gamma radiation at the surface of the soil. The moisture content of the soil is measured using a backscatter gauge that allows the neutron sources and detectors to be placed both in the same plane. The recorded attenuation of the fast neutrons at the surface of soil allows the determination of water mass per unit volume, from which the gravimetric water content can then be calculated. Dry density and degree of saturation are then calculated from these parameters. The latter calculation requires knowledge of the specific gravity of the aggregate which was assumed to be equal to 2.77 based on measurements performed following ASTM C127-15 as part of a previous research project (Getchell et al., 2020).

Finally, pictures of the finished surface of the aggregate layer were taken at all grid points and were processed using custom developed software (Garzon-Sabogal et al., 2024). The key output of the routine, which relies on detection of the two-dimensional projections of grains as features, is an index termed median feature size, which is found to effectively represent the

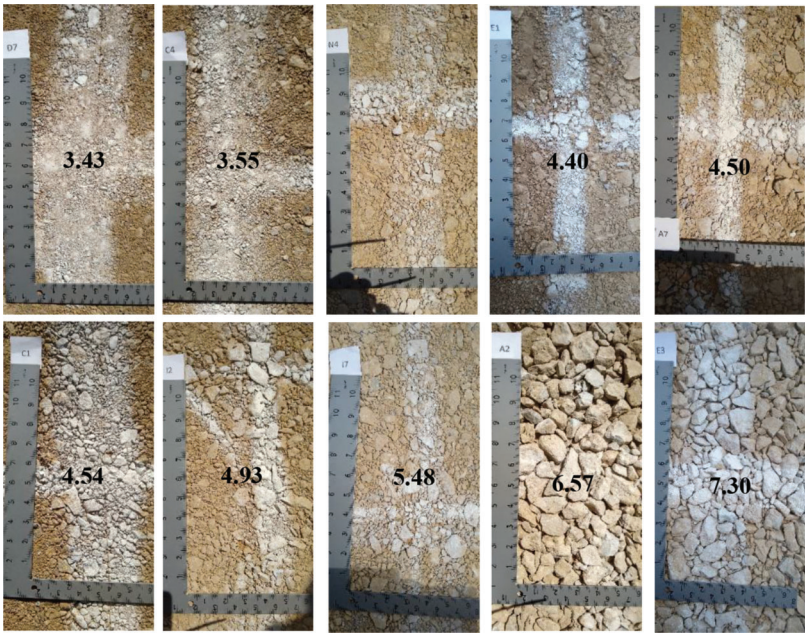

Figure 3.5 Images of aggregate surface at various locations on strips. The number at the center of each image represents the value of the median feature size (in mm) derived from image analysis.

differences in gradation observed visually. This is illustrated in Figure 3.5, which shows examples of values of the index (in mm) derived from the analysis of images at visually contrasting locations on the aggregate surface.

Key statistical indicators for the thickness of the aggregate layer for both strips, as well as for additional parameters discussed previously, are summarized in Table 3.1.

3.3 Identification and Overview of Conditions at Plate Load Testing Locations

Based on the significant range of variation of the strip layer properties observed from the LWD and ND tests, nine testing locations were chosen for the Automated Plate Load Tests (APLT): four on the UNT strip and five on the CT strip. The testing locations, which are identified in Figure 3.3, are herein referred using the following notation: CT or UNT to denote a location on the strip constructed on the cement treated or the untreated subgrade, followed by a letter (A to T) and a number (1–7) that identify the coordinates of the point on the grid shown in Figure 3.3.

As discussed in more detail in the rest of the report, two types of cyclic APLT tests were performed for this project. In the first, the loading protocol mimicked that used for laboratory resilient modulus tests. Hence the tests are referred to here as resilient modulus (MR) tests. The symbol MR is used to differentiate the test from the maetrial property (Mr) that the test is designed to measure. The second set of tests involved a larger number of loading cycles that followed a randomly distributed load, and that are thus referred to as RDL tests.

A summary of the tests performed at each location is presented in Table 3.2. In the table, MR tests performed on the subbase (aggregate) layer are referred to as resilient modulus tests with multi radius measurements to reflect that they involved measurement of the surface deflection not only on the plate but at distances of 2r, 3r, and 4r from the center of the plate. In most cases after completion of the test on the subbase, the aggregate was removed and the same test (with measurement of the deflection only on the plate) was repeated at the same location on the underlying subgrade. As noted in the table, two of the RDL tests were conducted on the subbase at locations (CTQ2 and UNTQ3) where a geotextile had been placed below the aggregate.

The testing locations for this project were selected by the research team to reflect the range of material conditions existing in the field. Key data obtained at each testing location during construction (thickness of subbase layer) and during the preliminary testing program (LWD deflections measured on both subgrade (large plate) and subbase (large and small plate), dry density and water content of subbase from ND tests, median feature size of subbase from image analyses) are summarized in Table 3.3 along with the mean values, standard deviations and the range calculated for each of these parameters from measurements at all grid points on each strip.

LWD deflection data for each strip are also shown in the form of histograms in Figure 3.6 (subbase–CT strip), Figure 3.7 (subbase–UNT strip) and Figure 3.8 (subgrade–both strips). Finally, Figures 3.9, 3.10, and 3.11 show 3D maps of LWD deflections and dry unit weight data. Measurements obtained in correspondence to the individual testing

TABLE 3.1
Key Statistical Indicators of Data for CT and UNT Strips

	Strip	$\bar{x}$	σ	CV	Skewness	Kurtosis	No. Measurement	Range
LWD-L (mm)	UNT	0.48	0.29	0.60	1.61	5.45	138	0.12–1.61
	CT	0.26	0.08	0.28	1.48	5.69	133	0.57–0.16
LWD–S (mm)	UNT	0.40	0.16	0.41	1.00	3.45	138	0.16–0.89
	CT	0.20	0.07	0.34	2.17	9.53	133	0.12–0.57
LWD-L Subgrade (mm)	UNT	1.44	1.32	0.92	1.62	4.80	129	0.07–0.54
	CT	0.16	0.07	0.45	1.97	8.67	126	0.22–6.03
	CT	4.48e3	3.62e3	0.80	3.35	19.70	132	9.42e2–2.70e4
Thickness (in)	UNT	5.48	1.95	0.35	-0.63	2.49	129	1.15–8.60
	CT	8.70	1.82	0.20	-1.22	4.28	126	3.00–11.55
Median Feature Index (mm)	UNT	5.97	0.82	0.14	-0.30	2.31	137	4.14–7.83
	CT	4.36	0.67	0.15	1.26	4.23	132	3.41–6.56
γ_d (pcf)	UNT	133.0	2.50	0.02	-0.84	3.40	39	126.1–138.0
	CT	138.0	2.50	0.02	-0.00	1.68	37	128.6–142.3
w (%)	UNT	3.50	0.33	0.09	0.27	3.10	39	2.90–5.90
	CT	4.62	0.57	0.12	0.22	2.04	37	3.30–5.80
S (%)	UNT	0.36	0.05	0.13	0.08	2.44	39	0.25–0.50
	CT	0.58	0.10	0.17	0.40	1.92	37	0.36–0.76

TABLE 3.2
Overview of Tests Conducted at Each Testing Location

Strip	Testing Location	Layer	Type of Test	Test ID.
Cement - Treated (CT)	CTC5	Subbase	Resilient Modulus Test w/ multi radius measurements	MR-CTC5-SB
		Subgrade	Resilient Modulus Test	MR-CTC5-SG
	CTM2	Subbase	Resilient Modulus Test w/ multi radius measurements	MR-CTM2-SB
		Subgrade	Resilient Modulus Test	MR-CTM2-SG
	CTJ2	Subbase	Resilient Modulus Test w/ multi radius measurements	MR-CTJ2-SB
		Subgrade	Resilient Modulus Test	MR-CTJ2-SG
	CTO4	Subbase	Extended Cycle Performance Test w/ Random Distributed Loading	RDL-CTO4-SB
		Subgrade	Extended Cycle Performance Test w/ Random Distributed Loading	RDL-CTO4-SG
	CTQ2[1]	Subbase	Extended Cycle Performance Test w/ Random Distributed Loading	RDL-CTQ2-SB
Untreated (UNT)	UNTJ6	Subbase	Resilient Modulus Test w/ multi radius measurements	MR-UNTJ6-SB
		Subgrade	Resilient Modulus Tests	MR-UNTJ6-SG
	UNTL3	Subbase	Resilient Modulus Test w/ multi radius measurements	MR-UNTL3-SB
		Subgrade	Resilient Modulus Tests	MR-UNTL3-SG
	UNTI2	Subbase	Extended Cycle Performance Test w/ Random Distributed Loading	RDL-UNTI2-SB
		Subgrade	Extended Cycle Performance Test w/ Random Distributed Loading	RDL-UNTI2-SG
	UNTQ3[1]	Subbase	Extended Cycle Performance Test w/ Random Distributed Loading	RDL-UNTQ3-SB

[1]Location where geotextile was placed below aggregate layer.

locations are identified on both the histograms and the 3D plots.

With few exceptions, the selection of the testing locations focused on points where the parameters reported in Table 3.3 fell within +/-1 standard deviation of all data for that strip. Moreover, where possible, an effort was made to choose locations that facilitated isolation of the effect of one or more parameters. For example, on the untreated strip, MR tests were performed at locations UNTJ6 and UNTL3, which showed a large difference in all the LWD results. In particular, the LWD deflection measured on the subgrade at UNTJ6 is over five times greater than that measured at UNTL3,

TABLE 3.3
Summary of Layer Characteristics at Testing Locations and Statistics from All Measurements on Each Strip

Location		LWD Deflection Data (mm)			Subbase Layer Thickness (in)	Subbase Dry Unit Weight (pcf)	Subbase Water Content (%)	Median Feature Size (mm)
		Subbase Large Plate	Subbase Small Plate	Subgrade Large Plate				
CTC5		0.274	–	0.154	6.65[1]	139.2	4.65	4.69
CTJ2		0.279	0.123[1]	0.108	9.95	137.3	4.42	4.36
CTM2		0.304	0.186	0.116	9.50	134.8[1]	4.52	5.12
CTO4		0.229	0.133	0.146	9.75	134.8[1]	4.54	4.11
CTQ2		0.279	0.176	0.153	8.40	137.3	4.3	4.18
CT (all grid points)	Ave	0.26	0.2	0.16	8.7	138.0	4.62	4.36
	σ	0.08	0.07	0.07	1.82	2.50	0.57	0.67
	Range	0.16–0.57	0.12–0.57	0.07–0.54	3.0–11.55	128.6–142.3	3.3–5.8	3.41–6.56
UNTJ6		0.575	0.419	2.214	5.90	133.6	3.64	6.45
UNTL3		0.300	0.321	0.430	7.55[1]	133.0	2.98[1]	6.20
UNTI2		0.384	0.283	2.368	7.00	133.0[1]	3.19	4.94
UNTQ3		0.375	0.399	1.412	6.85	131.7	3.21	.24
UNT (all grid points)	Ave	0.48	0.4	1.44	5.48	133.0	3.5	5.97
	σ	0.29	0.16	1.32	1.95	2.50	0.33	0.82
	Range	0.12–1.61	0.16–0.89	0.22–6.03	1.15–8.60	126.1–138.0	2.9–5.9	4.14–7.83

[1]Identifies values that fall outside +/- 1 standard deviation range.

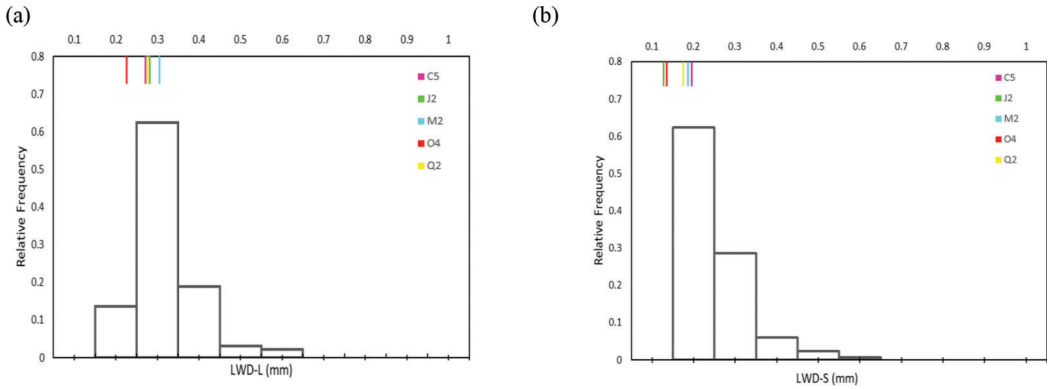

Figure 3.6 Histograms of LWD data on the subbase of CT strip: (a) LWD-L, and (b) LWD-S.

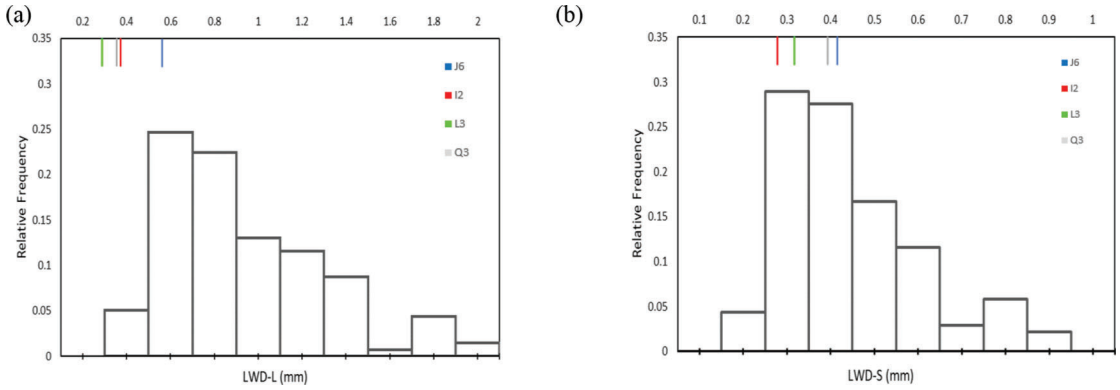

Figure 3.7 Histograms of LWD data on the subbase of UNT strip: (a) LWD-L, and (b) LWD-S.

providing an opportunity to assess the impact of contrasting subgrade conditions on the results of the plate loading test. Similarly, to permit comparisons between the two strips, one of the testing locations on the CT strip was chosen in correspondence to a point (CTC5) where the subbase thickness was comparable

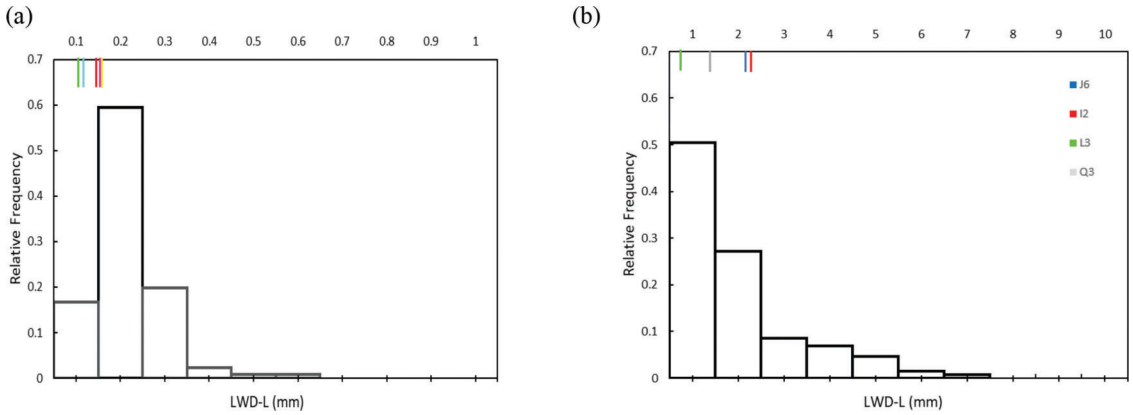

Figure 3.8 Histograms of LWD-L data on subgrade: (a) CT strip, and (b) UNT strip.

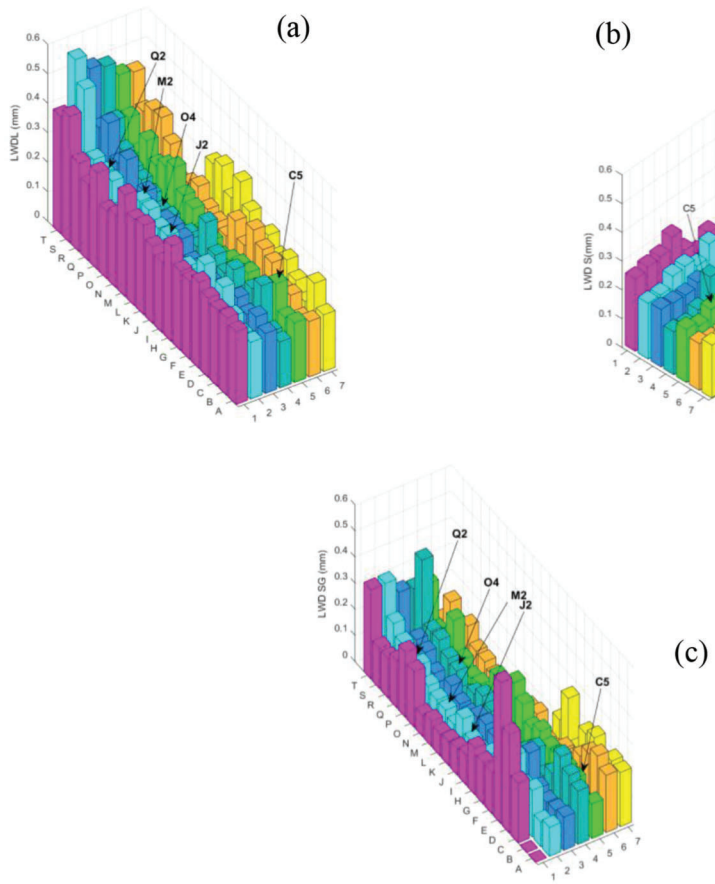

Figure 3.9 3D maps of LWD deflection data for CT strip: (a) LWD-L (subbase), (b) LWD-S (subbase), and (c) LWD-L (subgrade).

to those measured on the UNT strip (while outside the +/-1 standard deviation for the CT strip).

3.4 Test Pit for Static Plate Load Tests

Static plate load tests were performed in proximity to the strips, at three locations on a thick (3.6 ft ~110 cm) layer of the same #53 aggregate compacted in a pit having cross-section area of 9 ft × 18 ft (2.7 m × 5.4 m). The aggregate layer was constructed in 7 lifts on the compacted natural soil with a final average thickness of 3.6 ft. The aggregate was placed and graded using a loader, and then compacted using a SPF3000 vibratory plate compactor. In the test pit area, nonwoven geotextile was installed at the contact surface between the subgrade and aggregate layer. The images

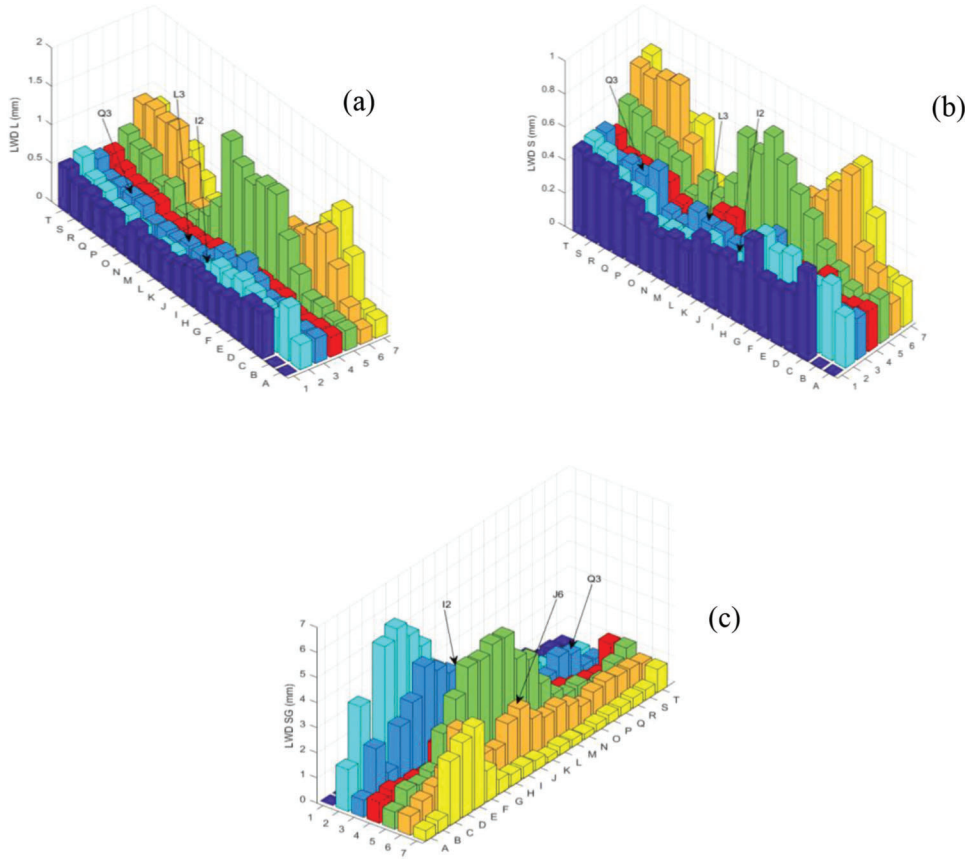

Figure 3.10 3D maps of LWD deflection data for UNT strip: (a) LWD-L (subbase), (b) LWD-S (subbase), and (c) LWD-L (subgrade).

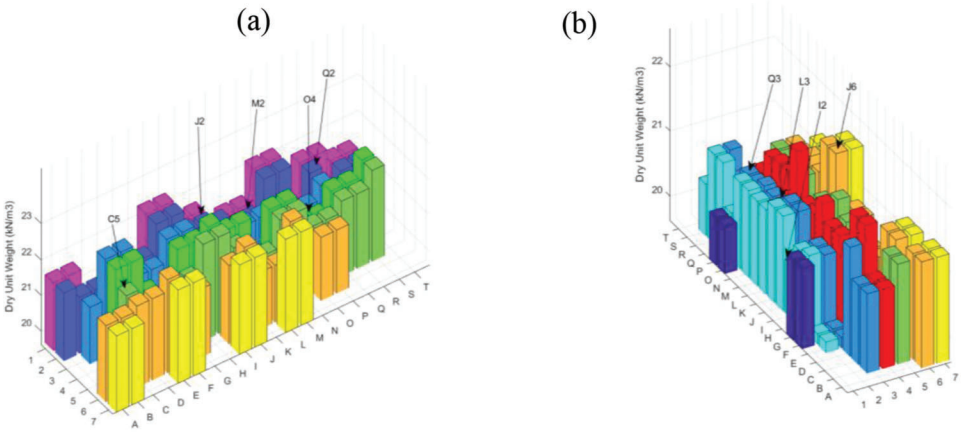

Figure 3.11 3D maps of dry unit weight data from ND tests: (a) CT, and (b) UNT strip.

in Figure 3.12 illustrate the steps followed for construction of the test pit. Elevation readings were collected using a rotary laser after each lift at the locations shown in Figure 3.13.

Standard Penetration Tests (SPT) were performed at three locations in the test pit (see Figure 3.13). The SPT tests were performed as per ASTM D1586 (ASTM, 2011). The borehole was advanced to a depth of 8 in to perform the test at a depth (~diameter of the plate) that was expected to be affected by the bearing capacity mechanism. The sampler was inserted into the soil by dropping a 140-lb hammer from a 30-in height. The measured values were corrected to a 60% energy level. For the overburden correction, a soil unit weight of 134.9 pcf (21 kN/m^3) was used. This data is discussed in Section 5.2.

Figure 3.12 Test pit construction sequence: (a) aerial view of test pit area, (b) markup of elevation reading's locations, (c) nonwoven geotextile installation at the interface between subgrade and aggregate base layer, and (d) aggregate layer compaction by means of a vibratory plate compactor.

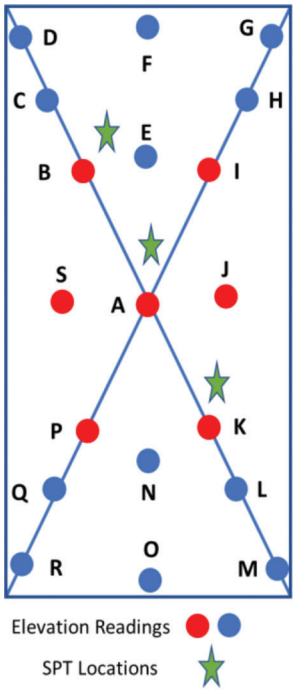

Figure 3.13 Schematic view of test pit locations used for elevation readings and SPT testing.

3.5 Plate Load Testing Equipment

All plate load tests were performed by Ingios Geotechnics using the trailer mounted automated plate load test (APLT) system shown in Figure 3.14a. It uses an advanced electronic-hydraulic control system to apply controlled static or cyclic loading through a circular bearing plate and allows application of complex loading patterns and control of loading frequency, pulse duration and dwell time (resting period between cycles). The loading system is compatible with plates of different dimensions. In this testing program 12 in (30 cm) and 18 in (46 cm) plates were used for the cyclic tests, while the static tests were performed using 8, 9.75 and 12 in (20, 25, 30 cm) plates. All plates had thickness of ~1 in (2.54 cm). As recommended by ASTM D1195/AASHTO T221 (AASHTO, 2021c; ASTM, 2021b), in all tests a thin bed of fine sand was placed between the loading plate and the ground surface to facilitate levelling. Settlement of the plate generated with every load step was measured via three proximity sensors positioned on the edge of the plate and mounted at 120° to each other (Figure 3.14c). The average settlement values obtained from each increment and the corresponding mean normal stress generate the load–deflection curve and provide measurements of the permanent and resilient deformation for each cycle, allowing calculation of stiffness parameters including the resilient modulus (Figure 3.15). The resilient deformation used in the stiffness derivation is the deflection of the plate during the unloading portion of the cycle calculated as the average value of the three measurements at the plate edge. As shown in Figure 3.14b, which illustrates the setup for the MR tests performed on the subbase layer, three additional proximity sensors were used in these tests to measure the deflection of curved beams seated on the ground

Figure 3.14 (a) APLT trailer and setup for automated plate load test (APLT), (b) on aggregate subbase with multi-radii deflection measurements, and (c) on subgrade after removal of aggregate, and (d) setup for static load tests.

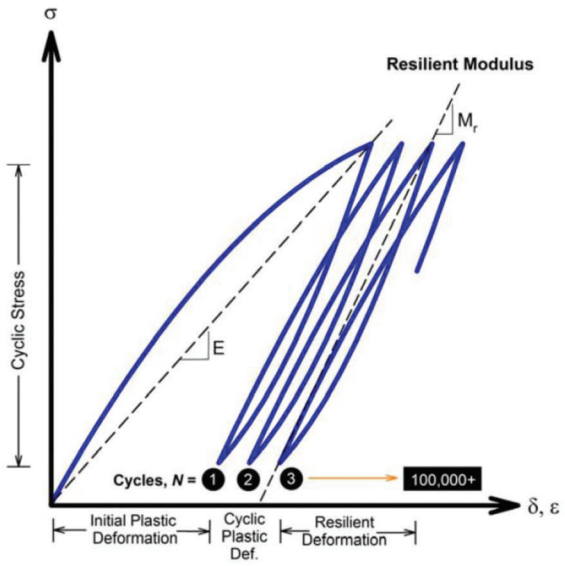

Figure 3.15 Derivation of resilient modulus from APLT cyclic plate load tests (White & Vennapusa, 2019).

at distances equal to 2r, 3r and 4r (r = radius of loading plate) from the center of the plate and covering approximately one third of the circumference of the circle at these values of the radius. As discussed by White and Vennapusa (2017) the use of this "layered analysis sensor kit" represents an improvement on previous point measurements of the deflection basin. Resilient deformations derived from these measurements are used in elastic layered analysis to derive stiffness parameters of underlying layers (White & Vennapusa, 2017).

3.6 APLT Testing Protocols

The plate load testing protocols followed in the testing program, especially those for the cyclic tests, differed from those commonly used in the field and described in existing standards such as ASTM D1195/AASHTO T221 (AASHTO 2021c; ASTM, 2021b). A summary of the loading protocols followed in the MR, RDL and static tests is presented in the following.

3.6.1 MR Tests

The loading procedure for the MR tests performed for this project is based on AASHTO T307-99 (AASHTO, 2021a) requirements for load duration, cycle duration and number of cycles. Moreover, as in AASHTO T307, and contrary to common plate load test standards, the testing procedure includes a conditioning stage of 500 load repetitions prior to the start of the actual loading stage. In the laboratory this stage is required to compensate for the imperfections associated with specimen setup and placement and alignment of the loading cap with the test specimen. For tests in-situ it is intended to simulate the non-virgin conditions of a layer that has been subjected to repeated loading during pavement construction (e.g., due to construction traffic and compaction equipment) and service. It is generally recognized that the conditioning stage affects the calculated resilient modulus values, as the applied stresses affect the stress history of the material prior to testing (Nazarian et al., 1996).

As indicated in Table 3.2, MR tests were performed at 5 different locations using a 12-in diameter plate for the tests conducted on the subbase layer and an 18-in diameter plate for the tests conducted on the

subgrade layer. Each test consisted of 1,550 cycles (including the 500 conditioning cycles), with 0.2 s load time and 0.8 s dwell time, as per AASHTO T307. Following the 500 conditioning cycles at 13 psi (89.6 kPa), the cyclic load was increased in 6 steps with the resulting cyclic stress amplitude varying from 4 psi to 38 psi (27.6 to 262.0 kPa) (Table 3.4). As shown in the table, the minimum stress remained constant at 2 psi, i.e., for a cyclic stress of 13 psi, the applied stress varied between 2 and 15 psi. As discussed previously, cyclic tests on the subbase layer were performed utilizing the "layered analysis sensor kit" developed by the testing contractor that provides additional measurements of surface deflection at distances of 2r, 3r, and 4r away from the center of the plate (Figure 3.14b).

3.6.2 RDL Tests

Extended cycle performance tests with random distributed loading (RDL tests) were performed at 4 locations (one on the subbase and one on the subgrade on each of the two strips), using 12-in and 18-in diameter plates. The RDL tests on the subgrade and two of those on the aggregate subbase included 5,000 loading cycles. The remaining two RDL tests on the aggregate subbase involved 10,000 cycles. As summarized in Table 3.5., the random distributed loading schedule used 10 different cyclic stress levels varying from 5 to 50 psi. The second column in this table (percent distribution) represents the number of cycles pertaining to each cyclic stress for 100 cycles set. The cyclic stress percent distribution is repeated in 100 cycle steps, but the loading pattern and the cyclic stresses applied are random for each set. In Figure 3.16a, the percent distribution of cyclic stress for the first 100 cycles is shown for all RDL testing locations. Figure 3.16b presents the percent distribution of cyclic stress for the first 400 cycles (four 100 cycles sets), for the test performed on the subbase at location CTQ2, in which a repeating pattern can clearly be observed.

3.6.3 Static Tests

Several standard test methods are available for performing static plate load tests, with the most common ones being ASTM D1196 (ASTM, 2021) and AASHTO T222 (AASHTO, 2021b), which are standard test methods for non-repetitive static plate load tests on soils and flexible pavement components. The testing procedure for APLT static tests performed for this project followed ASTM D1196 guidelines for plate and beam reference setup and for determination of the load duration for each load increment.

Static incremental load tests were conducted using 8 in, 9.75 in, and 12 in (~20, 25, and 30 cm) diameter

TABLE 3.4
Load Sequence in MR Tests

Step	Number of Cycles, N	Cyclic Stress, σ_{cyclic}(psi) (kPa) *nominal values*	Minimum Stress, σ_{min} (psi) (kPa) *nominal values*	Maximum Stress, σ_{max} (psi) (kPa) *nominal values*
Cond.	500	13 (89.6)	2 (13.8)	15 (103.4)
1	100	4 (27.6)	2 (13.8)	6 (41.4)
2	100	8 (55.2)	2 (13.8)	10 (68.9)
3	150	13 (89.6)	2 (13.8)	15 (103.4)
4	200	18 (124.1)	2 (13.8)	20 (137.9)
5	250	28 (193.1)	2 (13.8)	30 (206.8)
6	250	38 (262.0)	2 (13.8)	40 (275.8)

TABLE 3.5
Loading in RDL Tests

Test Designation	Relative Frequency (%)	Number of Cycles, N (per 100 cycle set)	Cyclic Stress, σ_{cyclic} (psi) (kPa) *nominal values*	Minimum Stress, σ_{min} (psi) (kPa) *nominal values*	Maximum Stress, σ_{max} (psi) (kPa) *nominal values*
5,000 to 10,000	5	5	5 (34.45)	2 (13.8)	7 (48.2)
Cycles RDL Tests	8	8	10 (68.9)	2 (13.8)	12 (82.7)
	15	15	15 (103.4)	2 (13.8)	17 (117.1)
	22	22	20 (137.8)	2 (13.8)	22 (151.6)
	16	16	25 (172.3)	2 (13.8)	27 (186)
	12	12	30 (206.7)	2 (13.8)	32 (220.5)
	9	9	35 (241.15)	2 (13.8)	37 (254.9)
	6	6	40 (275.6)	2 (13.8)	42 (289.4)
	5	5	45 (310.05)	2 (13.8)	47 (323.8)
	2	2	50 (344.5)	2 (13.8)	52 (358.3)

TABLE 3.6
Loading Sequence for Static Tests

Stage	Load Step	Target Applied Load (lbs)	Target Applied Stress (psi) (MPa)
Seating	0	75–113	1 (0.007)
Seating	0	0	0
Load	1	2,827	25 (0.17)
Load	2	5,654	50 (0.34)
Load	3	8,482	75 (0.52)
Load	4	11,309	100 (0.69)
Load	5	14,137	125 (0.86)
Unload	6	8,482	75 (0.52)
Unload	7	2,827	25 (0.17)
Load	8	8,482	75 (0.52)
Load	9	14,137	125 (0.86)
Load	10	16,964	150 (1.03)
Load	11	19,792	175 (1.21)
Load	12	22,619	200 (1.38)
Load	13	25,446	225 (1.55)

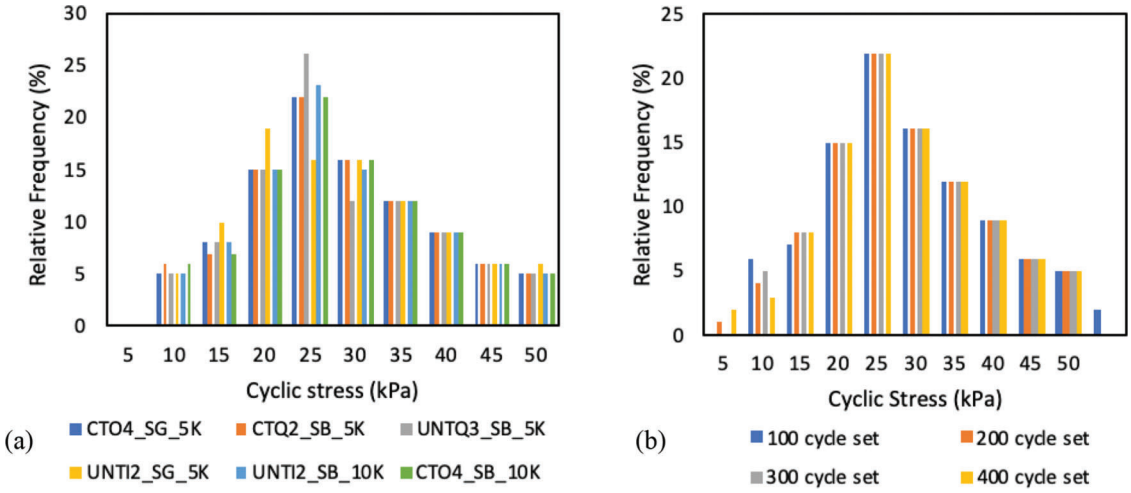

Figure 3.16 Cyclic stress relative frequency distribution for (a) first 100 cycles in all RDL tests, and (b) for first four sets of 100 cycles in test performed at CTQ2SB testing location (5,000 cycles)

loading plates. Prior to the application of the incremental load, a seating procedure for the bearing plate and the assembly was followed which required the application and release of a small load (75–113 lbs, corresponding to 1–1.5 psi (0.007–0.01 MPa)) until a deflection 0.01 in–0.02 in was achieved.

The applied stress was then increased up to 225 psi (1.55 MPa) in 25 psi (0.17 MPa) load increments (Table 3.6). The maximum stress reached in the tests was dictated by the maximum reaction force provided by the loading system (7 tons). The use of anchors was required in the test performed with the 12-in diameter plate. This approximately doubled the loading capacity. Figure 3.17 shows the testing setup with and without anchors. Per ASTM D1196, each load increment was maintained for at least 3 minutes once a rate of deflection of ~0.001 in/minute was achieved.

3.7 Example Data from APLT Tests

3.7.1 MR Tests

Resilient modulus (MR) tests were performed at five locations (Figure 3.3 and Table 3.2). The data from these tests provided to the research team consisted of the applied cyclic load from which the applied cyclic stress is calculated; the average permanent and resilient deformations of the loading plate measured at the end of each loading cycle (see Figure 3.15); and the resilient deformations measured for each loading cycle at 2r, 3r, and 4r. Data obtained from the test on the subbase layer at the CTC5 testing location are presented in Figure 3.18. They are qualitatively representative of the data obtained at all testing locations.

Figure 3.18a shows the variation of the applied maximum cyclic stress with number of cycles psi in

Figure 3.17 APLT static test setup: (a) without anchors, and (b) with anchors (adapted from Ingios, 2021).

6 loading steps (4, 8, 13, 18, 28, and 38 psi) following 500 cycles of conditioning. During each loading stage the applied cyclic stress remains within $\pm 5\%$ of the average value after the first 2–10 cycles. The small "jump" observed at the beginning of each loading step reflects the adjustment of the control system as the load is increased. While cyclic, the tests are interpreted as pseudo-static, and the values of the resilient modulus for each loading step are derived from the applied cyclic stress and the resulting resilient deflection.

Figure 3.18b shows the variation of the resulting permanent deformation with number of cycles. The permanent deformation increases slowly and gradually with time throughout the conditioning stage under the application of the 500 loading cycles, remains essentially constant during the first three loading stages (4–13 psi) ($\sim$5% increase relative to the value at the end of the conditioning stage) during which the cyclic stress is lower or equal than that applied during the conditioning stage, and starts increasing again during the fourth loading step. A similar response is observed over the last three loading stages with the rate of accumulation of permanent deformation gradually decreasing with the number of cycles over each loading step and increasing with stress level.

Figure 3.18c shows the variation of the resilient (i.e., recoverable—see Figure 3.15) deformation with number of cycles. The resilient deformation increases with stress level and remains approximately constant over each loading stage. Finally, Figure 3.18d presents the resilient deflections measured in the same test at radial distances equal to 2r, 3r, and 4r. All three measurements are approximately equal. This is because attenuation of stress at a certain depth with radial distance tends to reach a constant value. Qualitatively similar data were obtained from all other resilient modulus tests on the subbase aggregate layer. Table 3.7 summarizes the average deflections measured at the end of each loading stage.

Overall, similar trends are observed in the data for the MR tests conducted on the subgrade layer, as illustrated in Figure 3.19, which presents data obtained from one of these tests (MR test at CTC5 location).

3.7.2 RDL Tests

Extended cycle performance tests with random distributed loading (RDL) tests were performed at 4 locations (Figure 3.2 and Table 3.2). As discussed previously, RDL tests consisted in the application of 5,000 cycles (tests on both subbase and subgrade at locations UNTQ3 and CTQ2) or 10,000 cycles (tests on both subbase and subgrade at locations UNTI2 and CTO4). The RDL test data provided to the research team consisted of the applied cyclic stress and the average permanent and rebound deformations at the end of each loading cycle. Figure 3.20 shows an example of the data obtained from a RDL test (5,000 cycle test on subbase layer at CTQ2 testing location). Figure 3.20a shows the variation of the applied cyclic stress, which, as discussed previously, varied in the 5–50 psi (0.03–0.34 MPa) range with the same percent distribution of applied cyclic stress repeating every 100 cycles. Figure 3.20b shows the resulting permanent deformation. As discussed by Nazzal (2007), it increases rapidly during the first stage of the test reflecting the volume change produced by the loading (e.g., for the test shown, $\sim$50% of the final deformation is accumulated over the first 50 cycles). The rate of accumulation of permanent deformation decreases over time to an

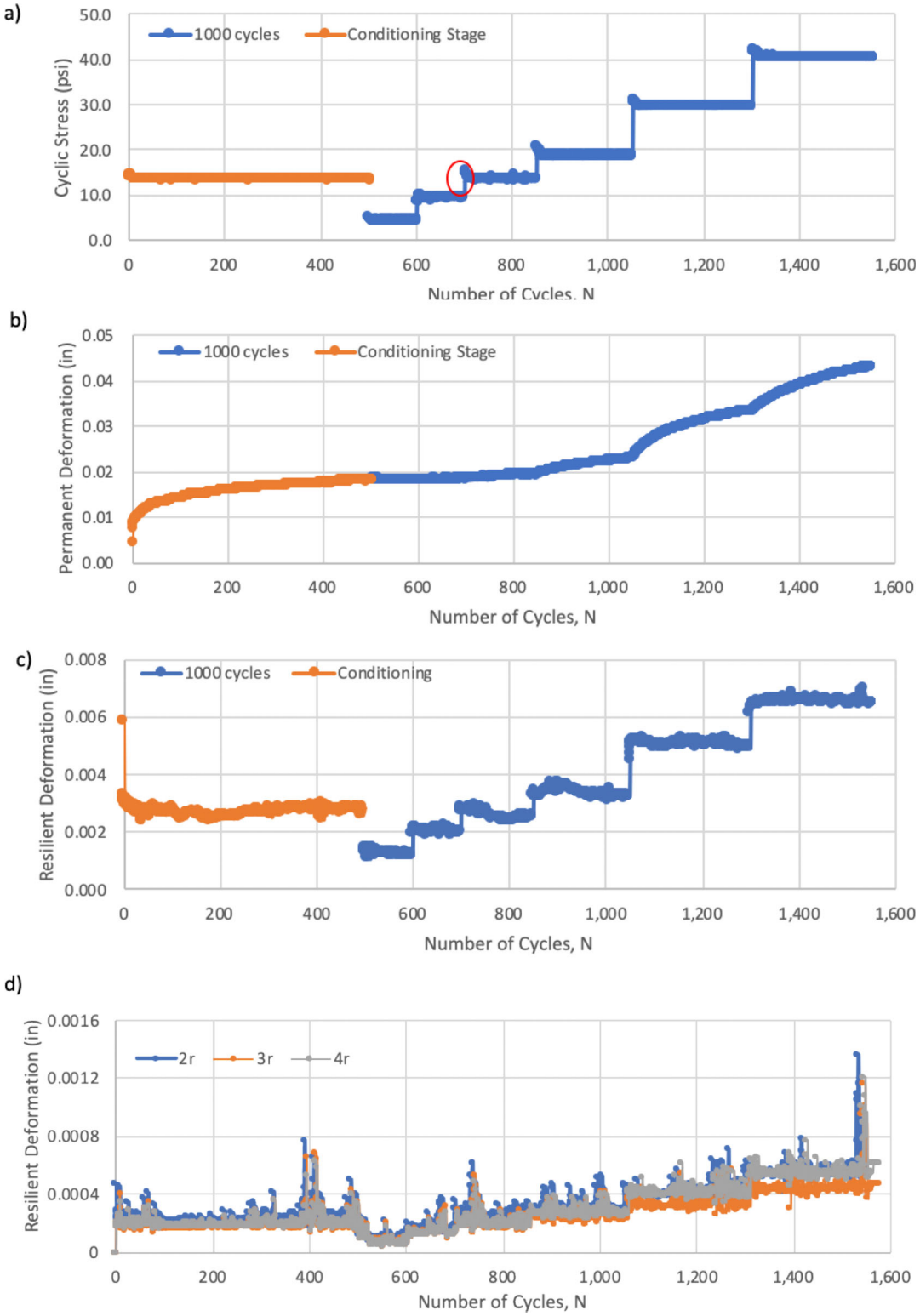

Figure 3.18 Example of data obtained from MR tests on subbase (CTC5 testing location): (a) maximum applied cyclic stress, (b) permanent deformation under plate, (c) resilient deformation under plate, and (d) resilient deformations at radial distances 2r, 3r, and 4r versus number of cycles.

approximately constant value. For the test shown this occurs at ~4,900 cycles, where the increase in permanent deformation per cycle is ~0.000025 in/cycle.

Figure 3.20c shows the variation of the resilient deformation with number of cycles, which follows the same pattern of the applied cyclic stress.

TABLE 3.7
Permanent Deformation (in inches) at the End of Each Loading Stage from MR Tests at All Testing Locations

Testing Location		Loading Stage						
		Conditioning	4 psi	8 psi	14 psi	18 psi	28 psi	38 psi
UNTJ6SB	Subbase	0.0283	0.0286	0.0290	0.0311	0.0517	0.1300	0.2038
UNTL3SB	Subbase	0.0300	0.0301	0.0304	0.0314	0.0370	0.0546	0.0735
CTJ2SB	Subbase	0.0148	0.0150	0.0149	0.0155	0.0187	0.0270	0.0342
CTM2SB	Subbase	0.0194	0.0192	0.0194	0.0201	0.0230	0.0330	0.0430
CTC5SB	Subbase	0.0181	0.0182	0.0184	0.0192	0.0229	0.0333	0.0431
UNTJ6SG	Subgrade	0.1230	0.1231	0.1237	0.1270	0.1537	0.2516	0.3600
UNTL3SG	Subgrade	0.0268	0.0270	0.0271	0.0280	0.0315	0.0460	0.0670
CTC5SG	Subgrade	0.0093	0.0094	0.0116	0.0100	0.0111	0.0122	0.0141
CTJ2SG	Subgrade	0.0066	0.0067	0.0067	0.0070	0.0073	0.0081	0.0087
CTM2SG	Subgrade	0.0119	0.0119	0.0120	0.0125	0.0130	0.0155	0.0175

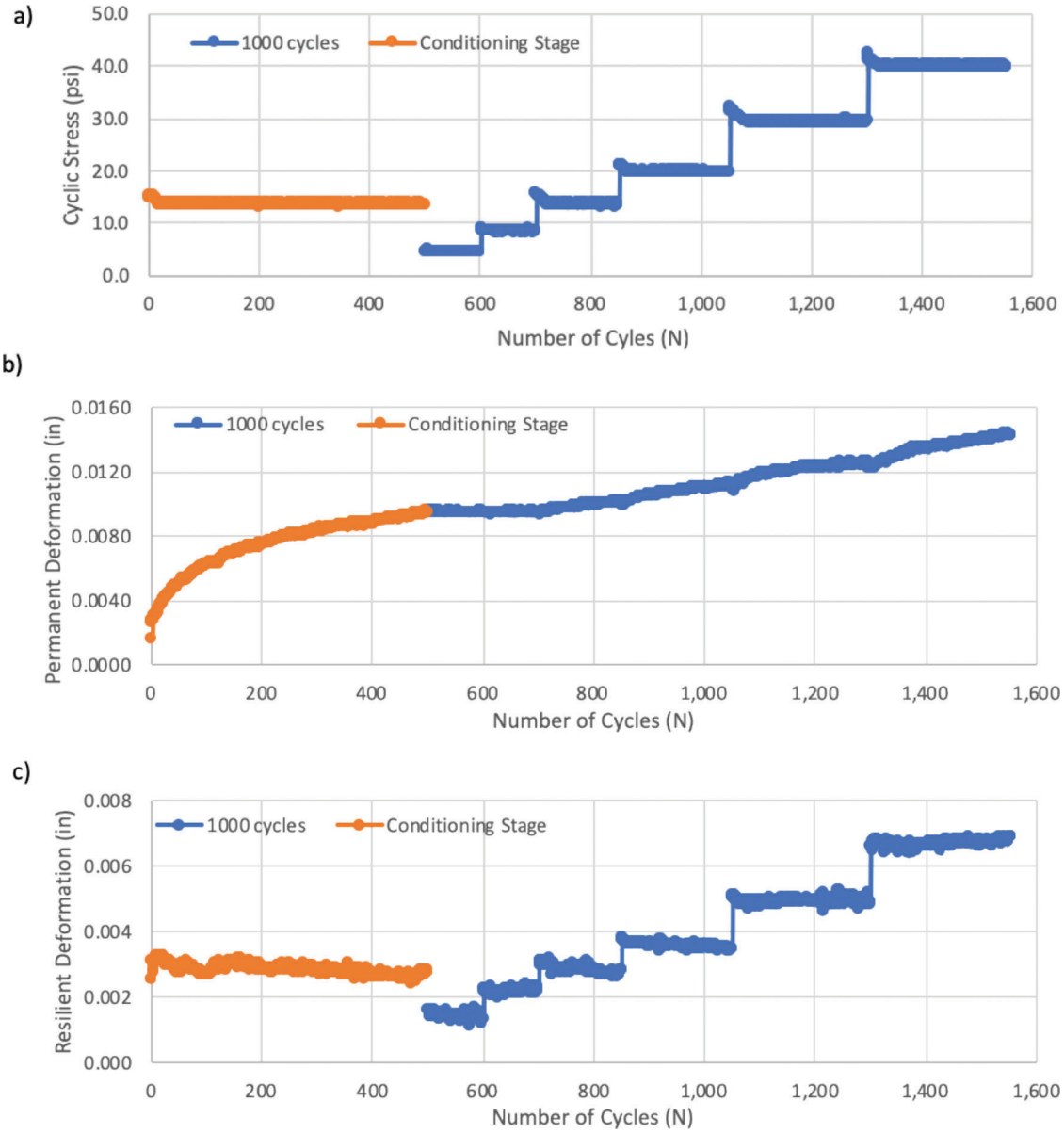

Figure 3.19 Example of data obtained from MR tests on subgrade (CTC5 testing location): (a) applied cyclic stress, (b) permanent deformation, and (c) resilient deformation versus number of cycles.

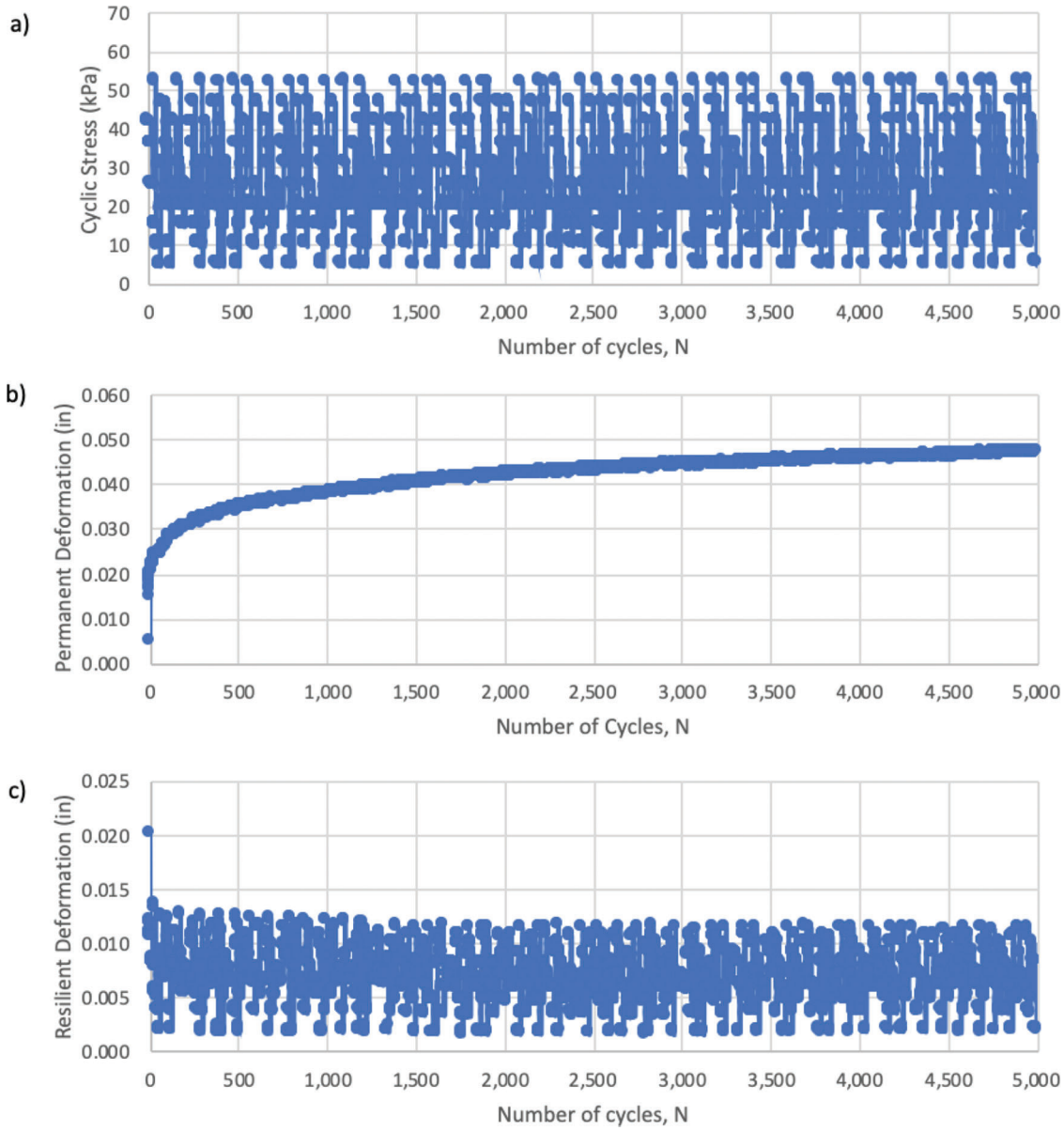

Figure 3.20 Example of data obtained from RDL tests on subbase (CTQ2 testing location): (a) applied cyclic stress, (b) permanent deformation, and (c) resilient deformation under plate versus number of cycles

3.7.3 Static Tests

Static load tests for this project were conducted using 8 in, 9.75 in, and 12 in (~20, 25, and 30 cm) diameter loading plates. The data from these tests provided to the research team consisted of the applied load from which the applied stress is calculated, and the average total deflections of the loading plate measured with time (averaged from 3 sensors). Data obtained from the 8-in diameter loading plate static test are presented in Figure 3.21. They show the variation of the applied stress and measured deflection with time over the entire duration of the test, including during the unload reload cycle. Similar data were obtained from the remaining two static tests. Plots of applied stress, average deflection, and rate of deflection versus time are presented in Figure 3.22 for the 75-psi stress increment from this same test. Figure 3.22c highlights the rapid decrease with time of the deflection rate. The standard test method for static tests (ASTM, 2021b) indicates that for each loading stage the load should be maintained until a rate of deflection of 0.001 in/min or less is achieved and maintained for three consecutive minutes. For the test load increment shown in Figure 3.22, this was found to occur approximately 6 minutes after the increase in the load. The complete load-settlement curve obtained from the data for the 8-in diameter plate test is shown in Figure 3.23.

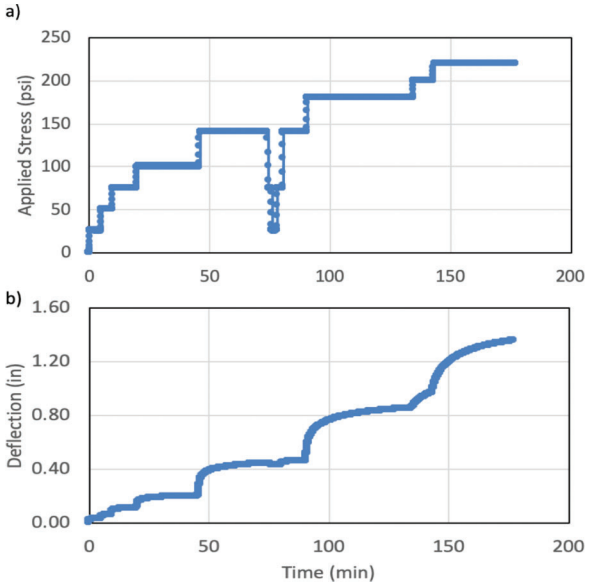

Figure 3.21 Data obtained from 8-inch diameter static plate load test showing variation of (a) applied stress, and (b) plate deflection with time.

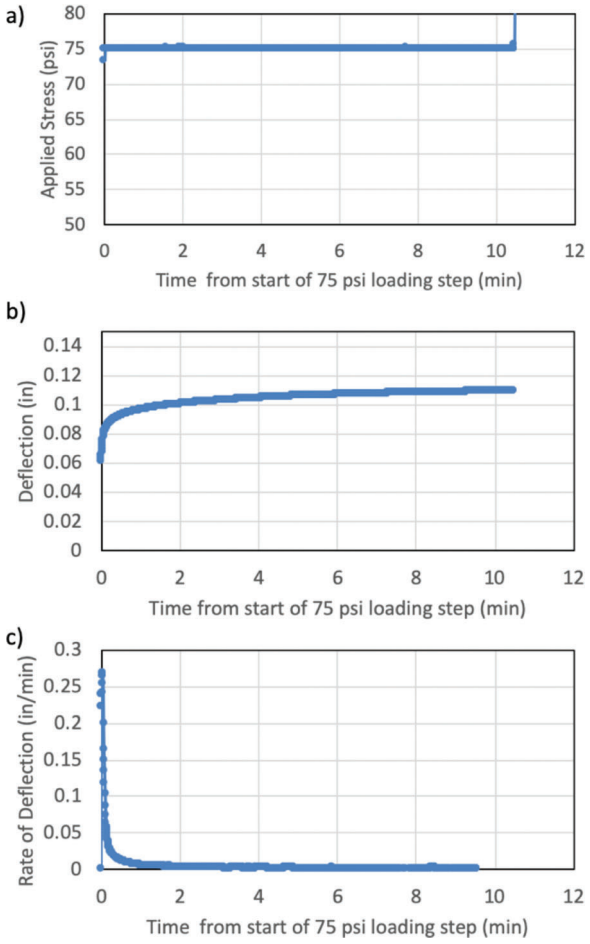

Figure 3.22 Data obtained from one load increment (75 psi) of 8-inch diameter static plate load test showing variation of (a) applied stress, (b) plate deflection, and (c) rate of deflection with time from start of increment.

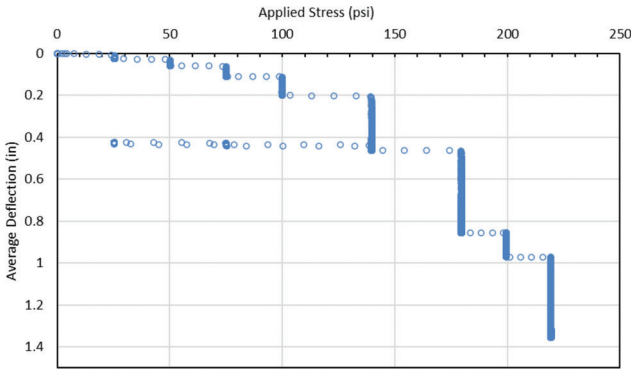

Figure 3.23 Load settlement curve for APLT 8-inch diameter static load test.

4. ANALYSIS AND INTERPRETATION OF M_r-TESTS

4.1 Introduction

This chapter is organized in two main parts. The first (Section 4.2) presents the results of a parametric study, performed using the finite element (FE) program ABAQUS, to examine the impact that assumptions on plate stiffness, material anisotropy, Poisson ratio and material homogeneity have on the stress and strain fields generated below a loaded circular area and on the resulting plate settlement.

The second part of the chapter (Sections 4.3 and 4.4) focuses on the analysis of the data obtained from the MR automated plate load tests performed at the S-BRITE site and described in Chapter 3. The analysis focuses exclusively on the resilient (elastic) deformation data, and on the derivation of the resilient modulus, M_r. Additionally, while the tests involved cyclic loading, this is neglected in the analyses, and for each loading stage average values of the cyclic stress and resilient strain (see Figure 3.18a and c) are used for calculating the modulus.

Section 4.3 outlines the approach conventionally used for the interpretation of plate load tests on both homogenous and layered systems, as put forth by White and Vennapusa (2017). The values of the M_r moduli derived for both subgrade and subbase applying this approach—herein referred to as "conventional"—to the analysis of the S-BRITE field data are then reviewed.

Further examination of select field data is presented in Section 4.4 based on additional analyses performed using ABAQUS. These explore the impact that assumptions inherent in the conventional approach have on the values of moduli predicted from the field data, discuss some of the limitations of such approach, and highlight the uncertainty associated with deriving values of the resilient modulus from plate load test data.

4.2 Parametric Study Using FE Analyses

As discussed in Section 2.4, commonly used approaches for the interpretation of plate load tests

rely on a number of simplified assumptions related to material response, including homogeneity and linear elastic isotropic behavior. In order to analyze the influence that each of the assumptions bears on the interpretation of plate load tests, numerical analyses were carried out using the ABAQUS finite element software package. A 2D axisymmetric finite element model was used to simulate loading by a circular plate, and a parametric study was performed to assess the influence of the following parameters on the interpretation and analysis of plate load tests: plate stiffness, Poisson ratio(s), material anisotropy as measured by the modulus anisotropy ratio ($n = E_h/E_v$), and stratification as measured by the layer modulus ratio ($R = E_{v\text{-toplayer}}/E_{v\text{-bottomlayer}}$). The following sections provide details on the FE model and summarize key results from these analyses.

4.2.1 Model

4.2.1.1 Model geometry. The plate, subbase and subgrade layer were all modeled as axisymmetric solid-deformable-homogeneous parts. Given the symmetry of the system only one half of the structure was modeled. The height of the model was chosen to be large enough to allow over 90% attenuation of vertical stresses with depth (h = 2 m, corresponding to 13.3r, with r = radius of the loaded plate) based on the Boussinesq solution for a flexible plate on an elastic isotropic medium. The horizontal dimension was also chosen as 2 m (~13.3r) to minimize boundary effects. Figure 4.1a shows the right half of the pavement model with dimensions 2 × 2 m which was used in all analyses involving a flexible plate on a single homogeneous soil layer. In the analyses of two-layer systems, the model was modified to comprise a 0.2 m-thick granular base layer on top of the subgrade layer. When considering rigid plate loading conditions, the model was further modified to include the plate itself, as shown in Figure 4.1b. The dimensions of the steel plate were chosen in accordance with the values of diameter (0.30 m) and thickness (0.025 m) presented in AASHTO T221 (ASTM, 2021b).

A total of 12320 CAX8R (eight-node axisymmetric) elements were used to mesh the subbase and subgrade layers (Figure 4.2). Forty-nine CAX8R additional elements were used to mesh the plate elements for the rigid case analysis.

4.2.1.2 Material models and input parameters. Analyses involving a single homogenous layer were conducted utilizing both isotropic and anisotropic linear elastic models. For the analysis of two-layer systems, anisotropic conditions were considered only for the top (subbase) layer, while the underlying subgrade layer was always modeled using an isotropic linear elastic model. Isotropic elasticity is the most common model used in the numerical analysis of pavement systems and requires the input of only two parameters: elastic modulus (E) and Poisson's ratio (ν).

As discussed by Barden (1963), a cross anisotropic model better represents the conditions existing in most natural and man-made deposits, including in compacted aggregate layers forming base and subbase layers of pavement systems, and use of such a model leads to improved predictions of stresses generated by applied loads. This material model requires the following definition of five independent elastic parameters.

$E_v = E_2$ = elastic modulus in the vertical direction.

$E_h = E_1$ = elastic modulus in the horizontal direction.

ν_{hh} = Poisson ratio quantifying the effect of the horizontal strain on the horizontal strain.

ν_{hv} = Poisson ratio quantifying the effect of the horizontal strain on the vertical strain.

G_{vh} = shear modulus in the vertical shear plane.

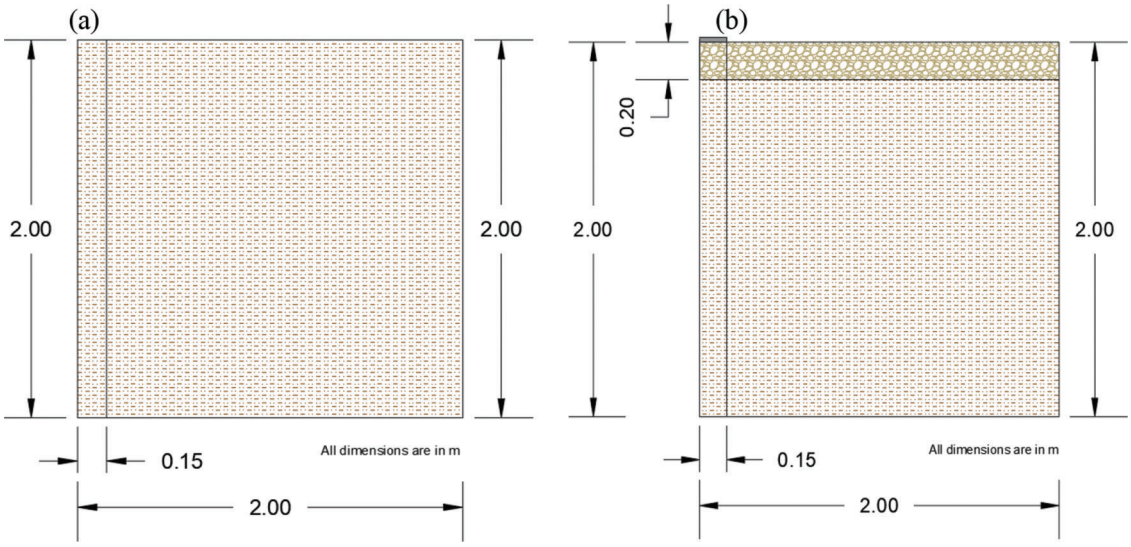

Figure 4.1 Cross-section of model for (a) flexible plate, single layer analysis, and (b) rigid plate, two-layer analysis.

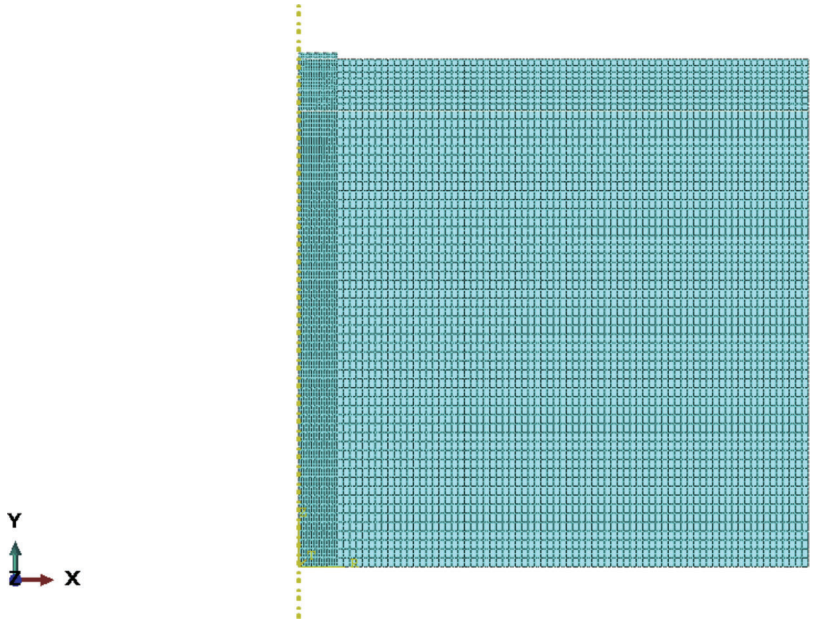

Figure 4.2 Finite element mesh (rigid plate, 2-layer analysis).

According to Love (1892), the remaining elastic parameters, v_{vh} and G_{hh}, are dependent on the other five independent constant and are defined as Equations 4.1 and 4.2.

$$\frac{v_{hv}}{E_h} = \frac{v_{vh}}{E_v} \qquad \text{(Eq. 4.1)}$$

$$G_{hh} = \frac{E_h}{2(1+v_{hh})} \qquad \text{(Eq. 4.2)}$$

where,

v_{vh} = Poisson ratio quantifying the effect of the horizontal strain on the vertical strain, and

G_{hh} = the shear modulus in the horizontal shear plane.

This reduces the number of input parameters from 9 to 7. In addition, for cross-anisotropic materials the vertical direction is also the axis of the material's rotational symmetry. As a result, $E_h = E_1 = E_3$ and $G_{hv} = G_{vh}$, which reduces the number of elastic constants required to describe an elastic cross-anisotropic material to 5.

The input parameters used in the single layer analyses are summarized in Table 4.1. The values of the Poisson ratios (ν = 0.2–0.4) were selected to satisfy the constraints posed by the thermodynamic requirements for positive strain energy for a cross-anisotropic material (Pickering, 1970). The vertical modulus (E_v) of the aggregate layer was set to 310 MPa and was kept constant in all the analyses. As the FE analyses were ultimately aimed at gaining insight into the interpretation of the plate load tests performed at the Purdue S-BRITE site (Chapter 3), this value was derived from one of the static plate load tests conducted at that location.

The modulus anisotropy ratio ($n = E_h/E_v$) was chosen to vary from 0.2 to 5 to represent the range reported in the literature for granular aggregate materials (e.g., Ashtiani & Little, 2009; Bellotti et al., 1996; Jiang et al., 1997; Seyhan & Tutumluer, 2002), Tutumluer et al. (2016), Hicher and Chang (2006)—see Chapter 2). When an independent input value for G_{vh} was required (non-isotropic conditions), it was selected equal to $0.3E_v$, based on literature data for granular materials. For example, Tutumluer and Thompson (1997) report values of G_{vh} = 18%–35% E_v from 50 repeated load triaxial tests on various granular materials (gravel, partially crushed and crushed aggregates). Similar values are reported by other authors (Bellotti et al., 1996; Modoni et al., 2000; Seyhan & Tutumluer, 2002; Wang & Al-Qadi, 2013).

Note that for n = 1, only three cases (identified in Table 4.1 by an asterisk) reflect true isotropic elastic conditions (two independent elastic constants, E and ν, with $G = E/(2(1+\nu))$). In the other cases $E_h = E_v$, but different combinations of the Poisson ratios are considered (i.e., anisotropy in ν) and/or a fixed value of G_{vh} is used. This was done for comparison to the cases with n different from 1 in which G_{vh} was kept equal to 93 GPa ($0.3E_v$).

For two-layer systems, the analyses examined the effect of the layer modulus ratio, R, which is defined as the ratio of the vertical modulus of the top layer (subbase for the tests of interest to this work) to that of the underlying one (subgrade), i.e., $R = E_{Subbase}/E_{Subgrade}$. As shown in Table 4.2, R was varied between 0.5 and 10. This range reflects both cases in which the subbase is less stiff than the underlying layer, as would occur for a cement treated subgrade, as well as cases in which it is stiffer, as might be expected for an untreated subgrade. In all cases the bottom layer (subgrade) was

TABLE 4.1
Material Input Parameters for Single-Layer Analyses (Flexible and Rigid Plate)

n	E_v (MPa)	E_h (MPa)	ν_{hv}	ν_{hh}	G_{hv} (MPa)
0.2	310	62	0.2	0.2	93
			0.2	0.3	
			0.2	0.4	
0.5	310	155	0.2	0.2	93
			0.2	0.3	
			0.2	0.4	
			0.3	0.2	
			0.3	0.3	
			0.3	0.4	
			0.4	0.2	
			0.4	0.3	
			0.4	0.4	
n = 1	310	310	0.2[1]	0.2[1]	129[1], 93
			0.2	0.3	
			0.2	0.4	
			0.3	0.2	119[1], 93
			0.3[1]	0.3[1]	
			0.3	0.4	
			0.4	0.2	111[1], 93
			0.4	0.3	
			0.4[1]	0.4[1]	
n = 2	310	620	0.2	0.2	93
			0.2	0.3	
			0.2	0.4	
			0.3	0.2	
			0.3	0.3	
			0.3	0.4	
			0.4	0.2	
			0.4	0.3	
			0.4	0.4	
n = 5	310	1,550	0.2	0.2	93
			0.2	0.3	
			0.2	0.4	
			0.3	0.2	
			0.3	0.3	
			0.3	0.4	
			0.4	0.2	
			0.4	0.3	
			0.4	0.4	

Note:
Red text identifies input parameters for base case.
[1]Cases for true isotropic conditions.

modeled as isotropic with ν = 0.3. For each value of R, 6 different cases were examined varying n of the top (subbase) layer between 0.5 and 2 and considering different values of the Poisson ratios, ν_{hh} and ν_{hv}. In all cases G_{vh} of the top layer was set equal to $0.3E_v$.

Finally, Table 4.3 summarizes the material input parameters used for modeling the plate.

4.2.1.3 Loading and boundary conditions. The loading of the model was performed in two steps. In the first step, the force of gravity affecting the model was simulated. In the second step, a static pressure of 275 kPa (~40 psi) was applied either at the top of the subbase layer (flexible case) or on top of the plate (rigid case). This value was selected as it represents the maximum stress applied in the plate load tests carried out in the field for this project. The density was assumed to be 2,200 kg/m^3 (corresponding to a unit weight of 21.6 kN/m^3 ~137.4 pcf) for the aggregate subbase layer and 2,000 kg/m^3 corresponding to a unit weight of 19.6 kN/m^3 ~124.8 pcf) for the subgrade layer. The value used for the aggregate layer was estimated from measurements conducted at the site where the plate load tests were performed (see Chapter 3). The same value was used for both untreated and treated subgrade based on compaction specifications for these layers.

The boundary conditions for the model are illustrated in Figure 4.3. Given the symmetry of the problem, the left boundary is an axis of symmetry, allowing vertical displacement only. The bottom boundary of the model restricts the displacement of the system in both directions. At the right boundary of the geometry, all nodes were constrained horizontally but were free to move in the vertical direction. Finally, the top boundary of the model is free of restraint.

4.2.2 Results of Parametric Study

4.2.2.1 Effect of plate stiffness. As summarized in Table 4.1, the cases examined in the analyses correspond to five different values of the anisotropy parameter n, 9 different combinations of the Poisson ratios and different values of the shear modulus. For n = 0.2, only three analyses could be performed, as for the other six cases the positive strain energy requirement was not satisfied. Figure 4.4 shows plots of the vertical stress distribution throughout the model for three different cases (n = 0.2, 1, 5) for both a flexible and a rigid plate (ν_{hh} = 0.4, ν_{hv} = 0.4, ν_{hv} = 0.2, G = 93 MPa) note that these include both the initial stresses, and the stress increases due to the load applied at the surface). According to the commonly adopted stress sign convention used in both standard mechanics and in FE software, normal compressive stresses are shown as negative, and tensile stresses as positive. Focusing on the comparison between flexible and rigid plate, as expected, the stress distribution beneath the load is uniform in the case of the flexible plate, while stress concentrations are observed under the edge of the rigid plate. This is true independent of the degree of anisotropy of the underlying material. At a certain depth from the surface, for all three values of the modulus anisotropy ratio n, the stress bulbs appear to be approximately equal for both the flexible plate and rigid plate.

It is of interest to examine the effect of the rigidity of the plate on the vertical stress distribution at a depth of 1.33r, which, for the tests analyzed in this work, corresponds to the average position of the interface between subbase and subgrade (8″ ~ 20 cm, see Chapter 3). This is done in Figure 4.5 which presents

TABLE 4.2
Material Input Parameters for Two-Layer Analyses (Flexible and Rigid Plate)

	Subbase					Subgrade	
$R = E_{vSubbase} / E_{vSubgrade}$	n = E_h / E_v	E_v (MPa)	E_h (MPa)	ν_{hv}	ν_{hh}	E_v (MPa)	ν
R = 0.5	0.5	310	155	0.3	0.3	620	0.3
	1		310	0.4	0.3		
	2		620				
R = 1	0.5	310	155	0.3	0.3	310	0.3
	1		310	0.4	0.3		
	2		620				
R = 2	0.5	310	155	0.3	0.3	155	0.3
	1		310	0.4	0.3		
	2		620				
R = 5	0.5	310	155	0.3	0.3	62	0.3
	1		310	0.4	0.3		
	2		620				
R = 10	0.5	310	155	0.3	0.3	31	0.3
	1		310	0.4	0.3		
	2		620				

TABLE 4.3
Material Input Parameters for Plate (Rigid Case Analysis)

Density (kg/m^3)	Elastic Modulus (GPa)	Poisson's Ratio (v)
7,800	210	0.28

plots of vertical stress increase normalized by the applied stress versus radial distance. Three curves are presented for both flexible and rigid plate, corresponding to values of the modulus anisotropy ratio n of 0.2, 1 and 5 ($\nu_{hh} = 0.4$, $\nu_{hv} = 0.2$, and G = 93 MPa in all the analyses). The figure shows that for all cases, modeling

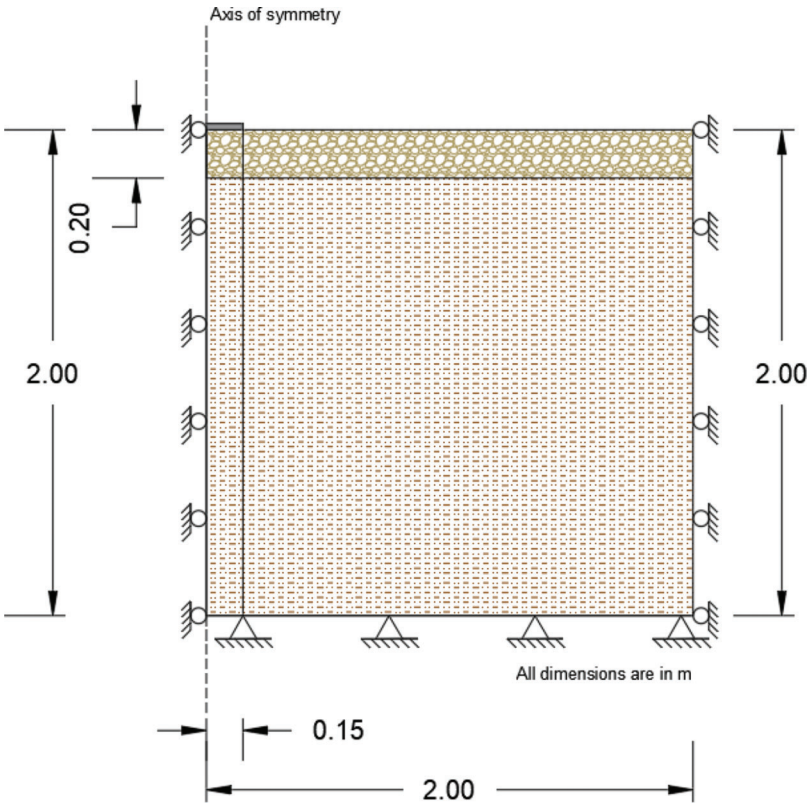

Figure 4.3 Boundary conditions for FE model.

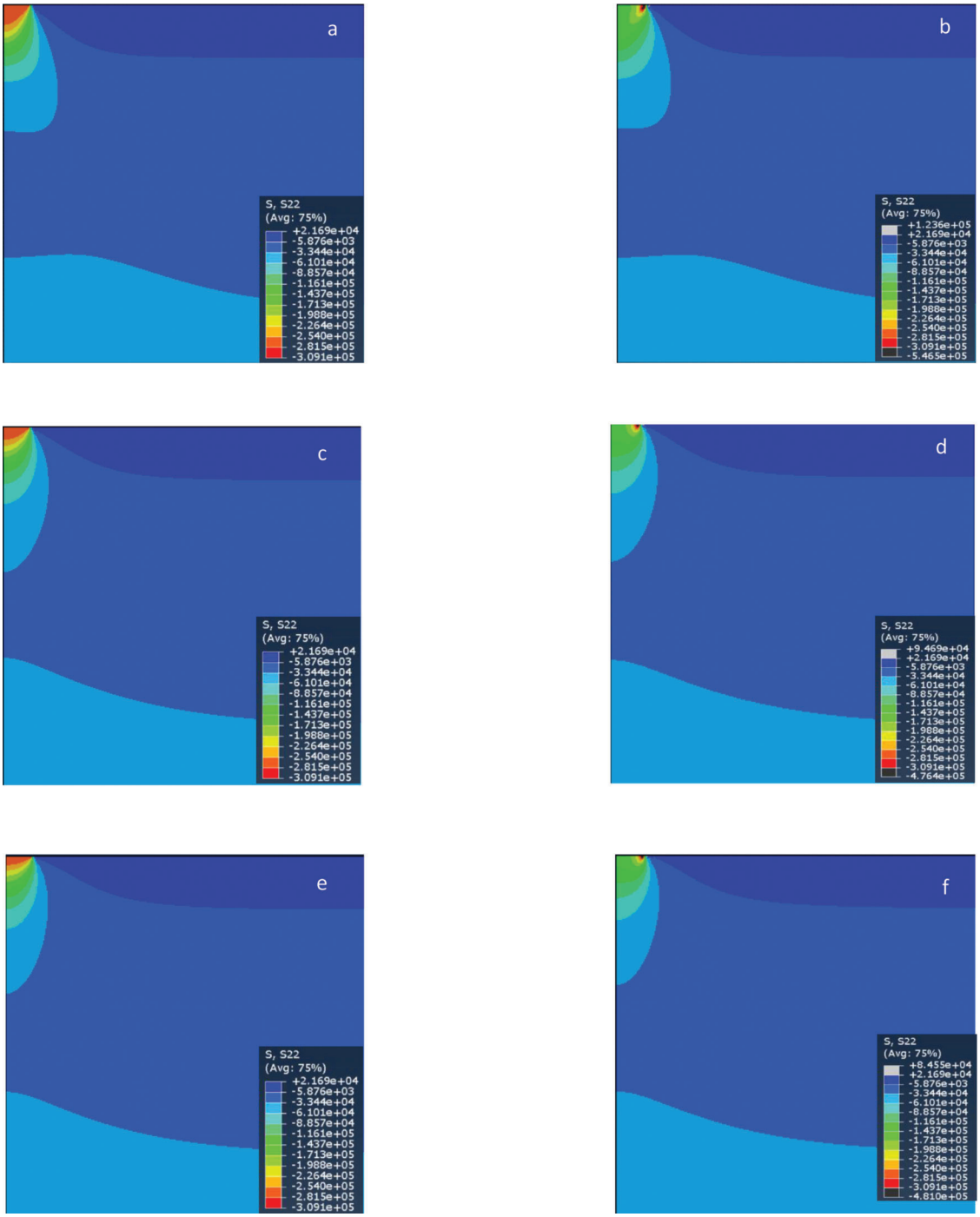

Figure 4.4 Vertical stress contours under flexible plate (left panels) and rigid plate (right panels) loaded with 275 kPa for (a)–(b) n = 0.2, (c)–(d) n = 1; (e)–(f) n = 5. Stresses in legend are in Pa (negative sign denotes compressive stresses).

the plate as flexible leads to predict stresses under the centerline of the plate approximately 30%–40% higher than for a rigid plate. The difference between the stresses reduces with radial distance and is negligible beyond ~2r from the center of the plate.

Modeling the plate as rigid versus flexible also impacts the strains produced by the applied stress and the resulting plate settlement. Graphs of incremental strain with depth under the centerline of the plate are presented in Figure 4.6 for n = 1, with the different colors representing different values of the Poisson ratios. As expected, lower values of strain are predicted under the rigid plate. The difference is as large as 70% within a depth equal to the radius, r, of the plate. With increasing depth, the differences between the two analyses are reduced, and at a depth of ~3r the influence of plate stiffness is no longer significant (difference < 20%).

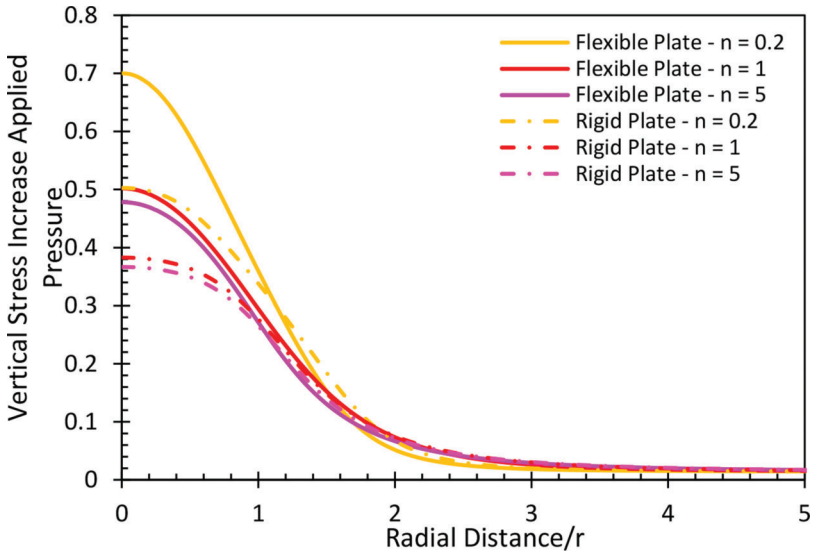

Figure 4.5 Vertical stress increase versus radial distance at a depth of 1.33r for different values of n for flexible and rigid plate (v_{hh} = 0.4, v_{hv} = 0.2 in all cases; r is plate radius).

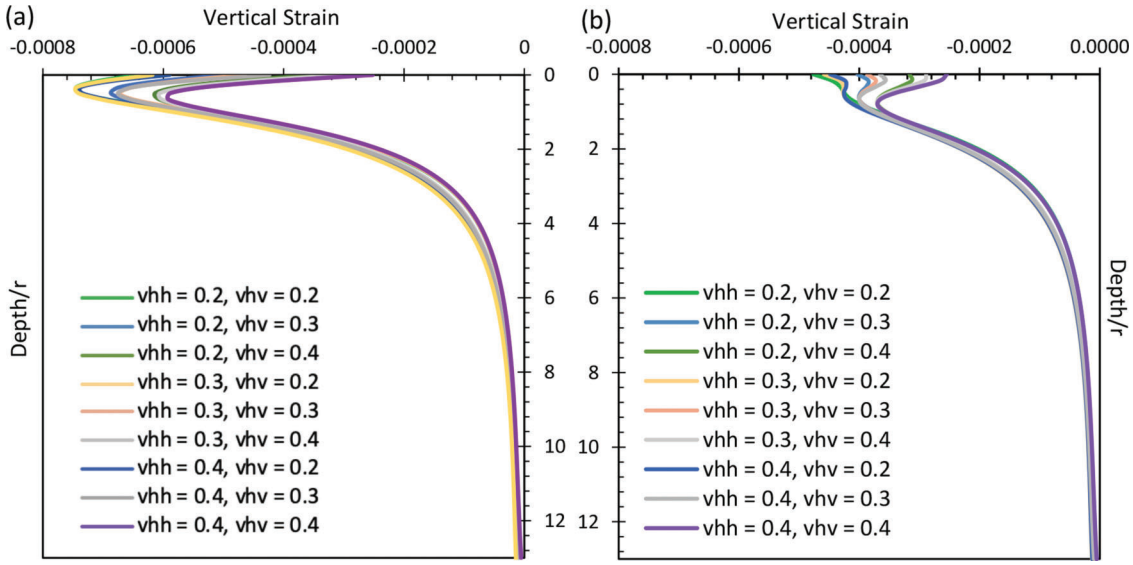

Figure 4.6 Vertical strain versus normalized depth for different values of the Poisson ratios: (a) flexible plate, and (b) rigid plate (n = 1 for all cases; r is plate radius). Note that negative strains denote compressive strains

Finally, Figure 4.7 shows the variation of the plate settlement as a function of n for loading of both a flexible and rigid plate. In general, independent of the degree of anisotropy (discussed in the following section) and of the value of the Poisson ratio, the settlement predicted under the rigid plate is approximately 20% lower than for a flexible plate.

4.2.2.2 Effect of material anisotropy. As discussed previously, five different values of the modulus anisotropy ratio n (0.2, 0.5, 1, 2, 5) were examined, covering the range reported in the literature for aggregate materials (see Section 4.2.1). As shown in Figure 4.4, for a given plate stiffness, the degree of modulus anisotropy affects the vertical stress distribution under the loaded area. This is reflected in the shape of the pressure bulbs, which for n = 0.2 and n = 5 appear, respectively, "plumper" and slenderer relative to the n = 1 case. For n = 0.2, up to a depth of approximately 3r, the stress increase propagates further both laterally and in depth, compared to what is observed for n = 1. The opposite effect is seen for n = 5. The faster vertical stress attenuation with depth with increasing modulus anisotropy ratio is further illustrated in Figure 4.8, which shows plots of the vertical stress increase under the centerline of the applied load for both a flexible and a rigid plate. These figures also show that below a depth of 3r, the

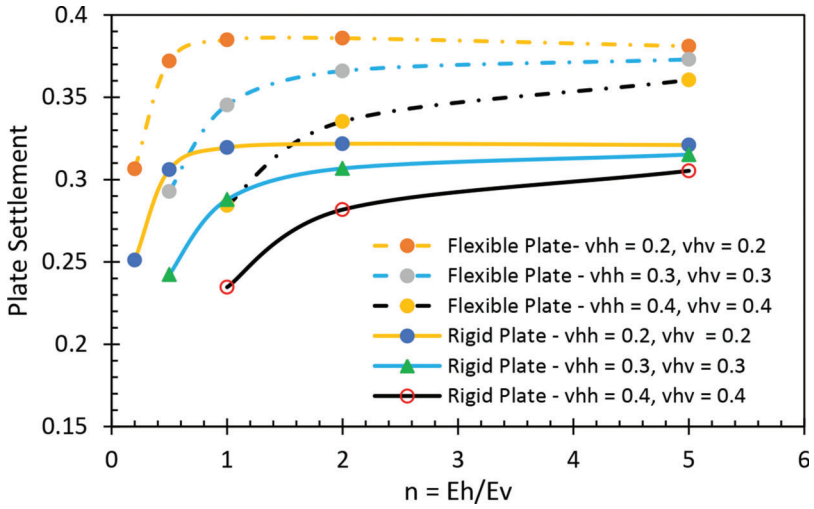

Figure 4.7 Effect of modulus anisotropy ratio, n, and plate stiffness on plate settlement.

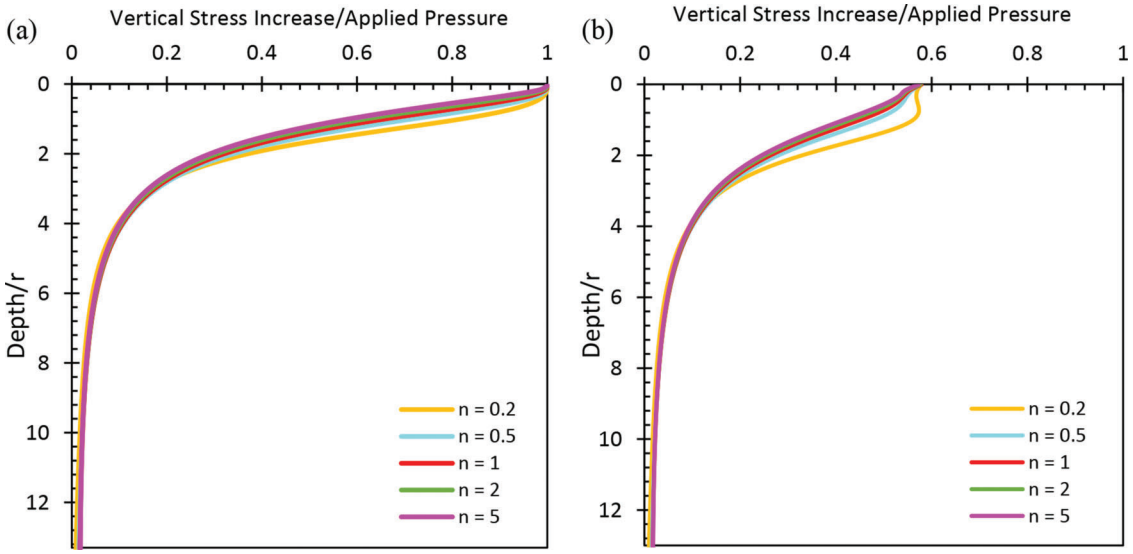

Figure 4.8 Vertical stress increase with depth under the centerline of plate for different values of the modulus anisotropy ratio, n: (a) flexible plate, and (b) rigid plate (v_{hh} = 0.4, v_{hv} =0.2 in all cases; r is plate radius).

vertical stress increases under the center of the plate are effectively independent of n.

Again, it is of interest in the context of this work, to examine the effect of the degree of modulus anisotropy, as measured by n, on the vertical stresses increases generated at a depth of 1.33r (0.2 m ~ 8 in), corresponding to the position of interface between subbase and subgrade in the plate load tests analyzed for this research. Plots of vertical stress increase versus radial distance are presented in Figure 4.9a and Figure 4.9b for flexible plate and rigid plate, respectively. In these figures, the different colors represent different values of the modulus anisotropy ratio n. For each value of n, several curves are presented, each corresponding to different values of the two Poisson ratios. To start, it is observed that changes in the Poisson ratio values have minor impact on the stress increases generated in the granular layer. The modulus anisotropy ratio, n, is found, instead, to play a significant role. For example, in the case of a flexible plate, for n = 0.2 the vertical stress increase under the centerline of the plate is predicted to be approximately 30% higher than for n = 1, and over 45% higher than for n = 5. Similar but slightly smaller differences are observed for a rigid plate (Figure 3.9b). Beyond a radial distance of ~1.5 r the curves all converge indicating no effect of material anisotropy.

Finally, Figure 4.10 illustrates the variation of the plate settlement as a function of n for flexible (Figure 4.10a) and rigid plate (Figure 4.10b). In these figures, values of the plate settlement are normalized by the settlement calculated for the same plate type (flexible or rigid) with the base case input parameters

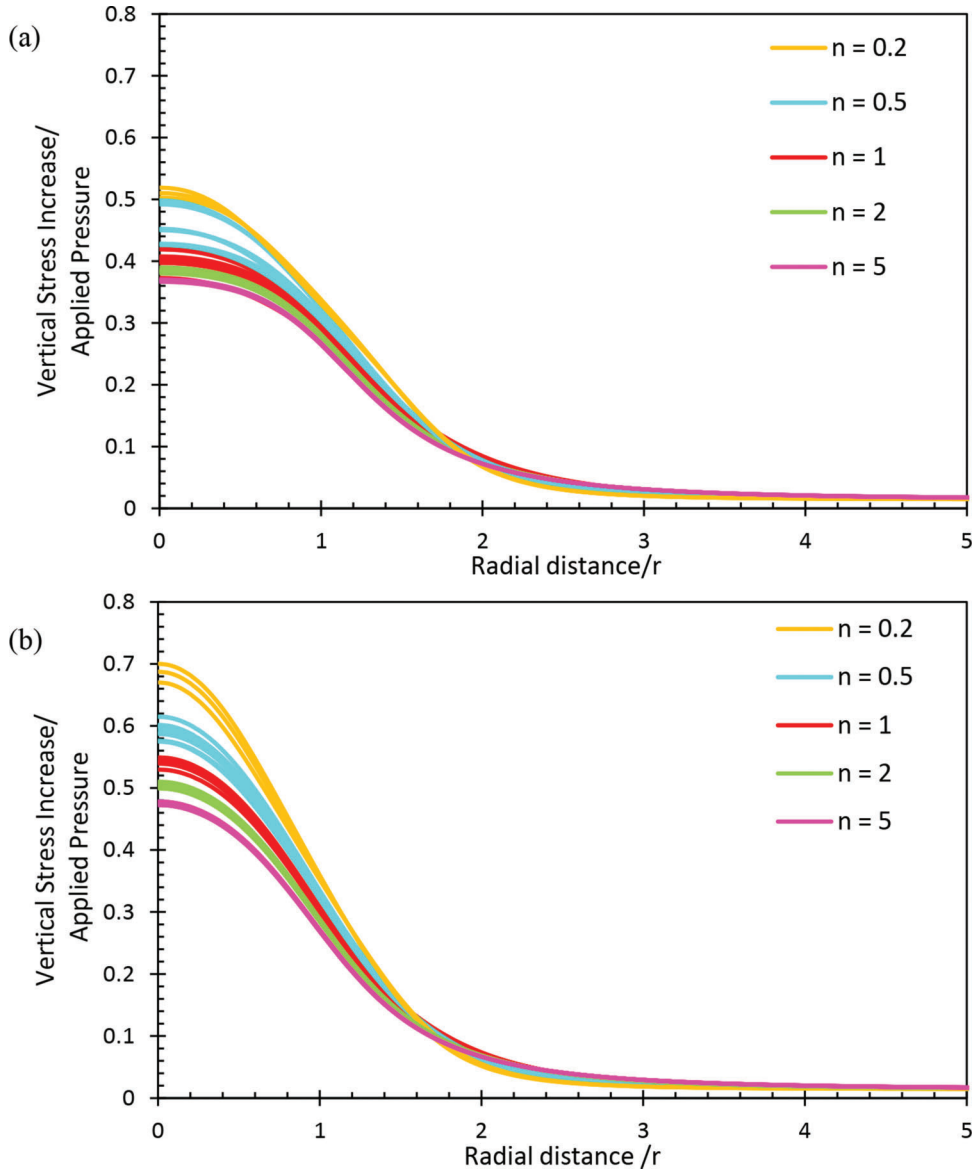

Figure 4.9 Vertical stress increase with radial distance at a depth of 8 inches (1.33 r) for five different anisotropy ratios and nine Poisson ratio combinations: (a) flexible plate, and (b) rigid plate (r is plate radius).

(n = 1, homogeneous conditions with $\nu_{hh} = \nu_{hv} = 0.3$ and G_{hv} = 93 GPa, see Table 4.1). The curves corresponding to the base case are identified in both graphs with dashed lines. Focusing on the left portion of the curves, for both flexible and rigid plate, the predicted plate settlement is observed to be significantly affected by changes in the modulus anisotropy ratio between 0.2 and 1, with smaller settlements predicted with decreasing n. As shown in Figure 4.10a–b the impact of n is influenced by the input value for ν_{hv}, with the results for ν_{hv} = 0.4 showing the greatest effect of n on the predicted settlement. For example, for n = 0.5, the predicted settlement is reduced by approximately 45% relative to that predicted for n = 1, when ν_{hv} = 0.4. This percentage is reduced to 15% and 3% for ν_{hv} = 0.3 and a ν_{hv} = 0.2, respectively.

While the same trend of increasing settlement with increasing modulus anisotropy ratio generally extends to values of n>1, the changes in predicted plate settlement are smaller as n increases further, and the curves remain essentially flat for n>2. A deviation from this trend is observed only for the analyses with ν_{hv} = 0.2, all of which show a small decrease in plate settlement as n increases from 2 to 5. As discussed in Chapter 2, typical values of the modulus anisotropy ratio n for aggregate materials fall below 1. This indicates that modeling granular aggregate materials as isotropic (n = 1) would lead to significantly overestimate plate settlements (or, conversely, underestimate moduli derived from plate load tests).

Note that to isolate the effect of n, the settlements shown in Figure 4.7 and Figure 4.10 all refer to cases with a common value of G_{hv} equal to 93 MPa.

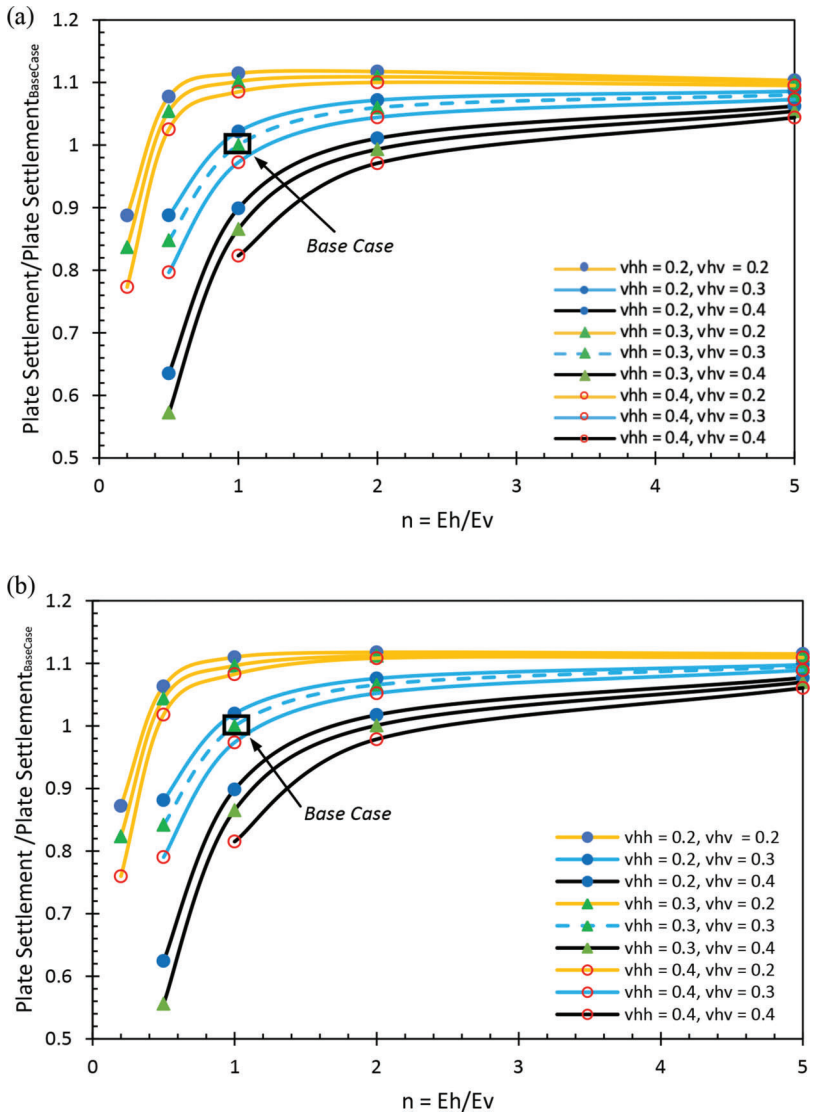

Figure 4.10 Variation of plate settlement with modulus anisotropy ratio n: (a) flexible plate, and (b) rigid plate.

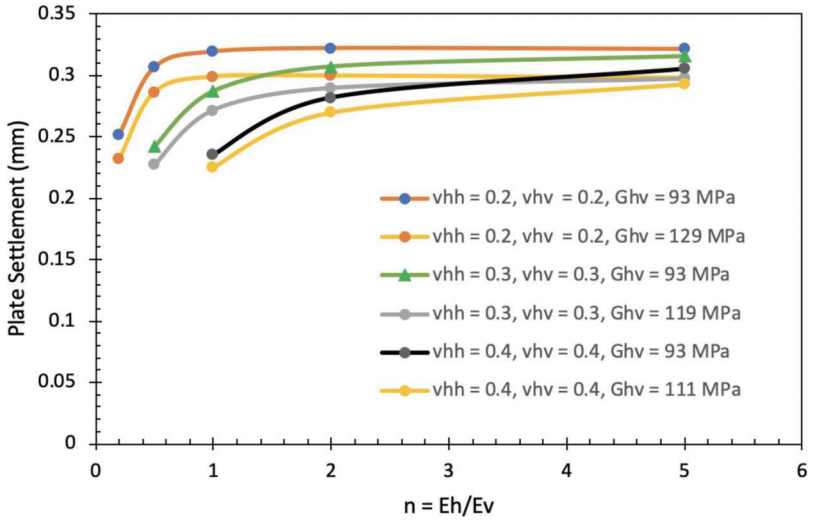

Figure 4.11 Variation of plate settlement with modulus anisotropy ratio n: (a) flexible plate, and (b) rigid plate.

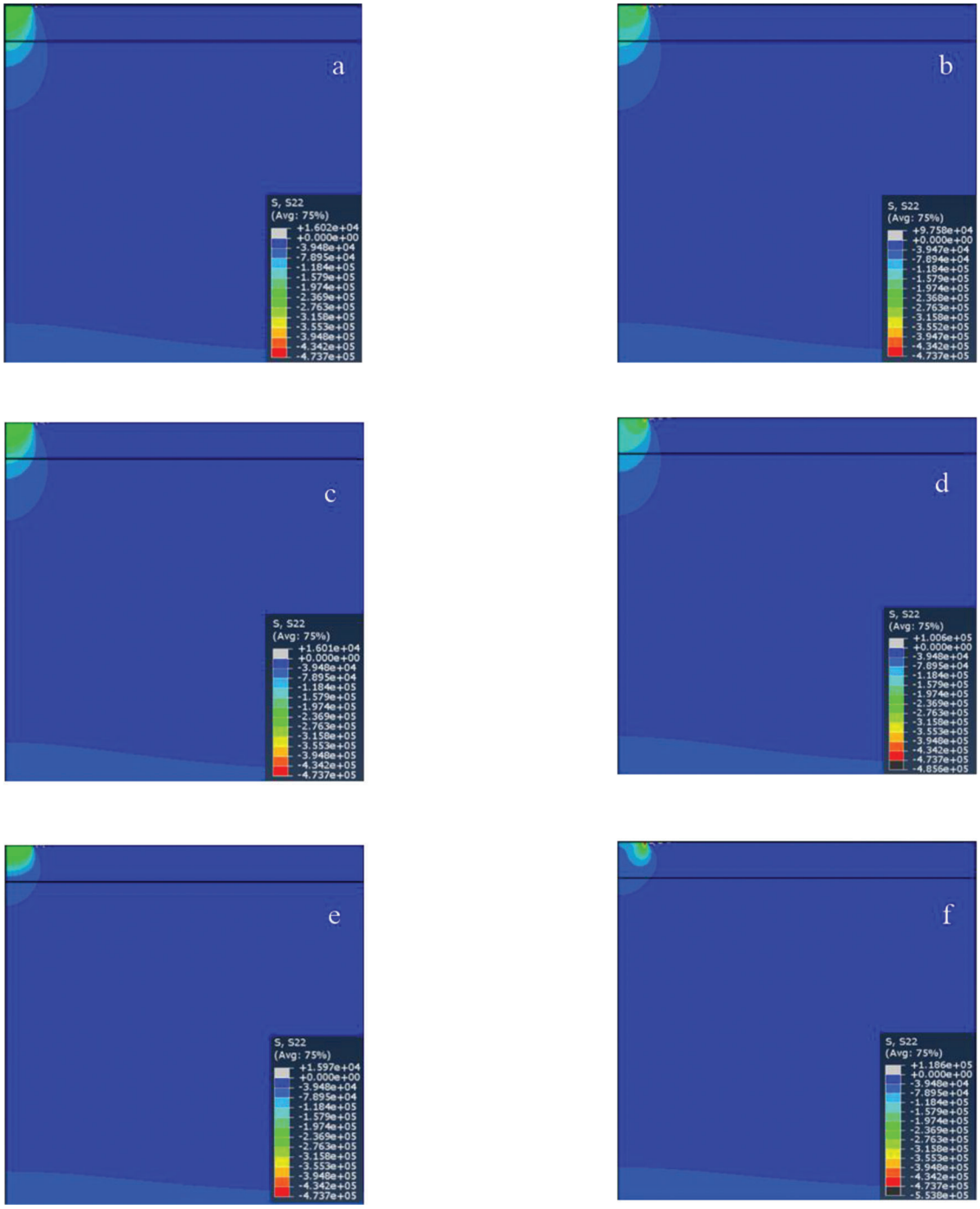

Figure 4.12 Vertical stress contours under flexible plate (left panels) and rigid plate (right panels) loaded with 275 kPa for different values of the layer modulus ratio, R: (a)–(b) R = 0.5; (c)–(d) R = 1; (e)–(f) R = 10 (n = 1, ν_{hh} = 0.3, ν_{hv} = 0.3 for all cases). Stresses in legend are in Pa (negative values denote compressive stresses).

The input value for G_{hv} does, of course, affect the results. This is shown in Figure 4.11 which, for the rigid plate case, compares the settlements plotted in Figure 4.7 to those predicted using as input for G_{hv} the value corresponding to true isotropic conditions (G = E/(2[1+ν])). While, as expected, smaller plate settlements are calculated for higher values of G_{hv}, the trend with n remains unchanged. For simplicity, all subsequent discussion refers to analyses performed with the same value of G_{hv} equal to 93 MPa.

4.2.2.3 Effect of stratification. To analyze the effect of the presence of stratified layers on the interpretation of plate load test data, a parametric analysis was performed for a two-layer system comprised of a 0.2 m subbase layer over a 1.8 m subgrade layer (Figure 4.1b). In these

analyses the layer modulus ratio, R, ($R = E_{vSubbase}/E_{vSG}$) was varied between 0.5 and 10, in all cases holding the modulus of the top layer constant (see Table 4.2). As discussed previously, this range reflects conditions that are representative of those existing in the tests analyzed as part of this research (aggregate layer overlying a stiffer cement treated subgrade, or a softer compacted but untreated subgrade). For each case, analyses were performed varying the modulus anisotropy ratio of the top (subbase) layer to evaluate the combined effect of stratification and anisotropy on the predicted behavior.

Figure 4.12 shows plots of the vertical stress distribution throughout the model for three different values of R (R = 0.5, 1, 10) for both a flexible and a rigid plate (n = 1, $\nu_{hh} = 0.3$, $\nu_{hv} = 0.3$ in all cases). For both plate stiffness conditions, as R increases, the pressure bulbs extend less deep into the model, i.e., stress attenuation is more rapid. This trend is more apparent for the rigid plate case.

Figure 4.13a shows the vertical stress increase with depth under the center of a flexible plate for all cases analyzed. Different colors are used to identify the results obtained for different values of R, while the curves shown for each R pertain to different degrees of material anisotropy (n = 0.5, 1, and 2) and different Poisson ratio values (see Table 4.2 for details). The inset figures show the detail for the top layer. As one can observe, for R = 10 vertical stress increases in the top subbase layer are approximately half those for a homogeneous system (R = 1) and three times smaller than for R = 0.5. Both changes in material anisotropy and in the Poisson ratio are found to have secondary effects, with only negligible variations between the different cases.

Figure 4.13b presents the corresponding plots of vertical strain with depth under the centerline of a flexible plate. The following two trends are observed with an increase in the layer modulus ratio R: a decrease in the vertical strain above the interface between the two layers (1.33r), and the reverse behavior for the material below the interface. As the vertical modulus of the top layer was kept constant in all the analyses (see Table 4.3), the reduction in vertical strain above the interface reflects the increased stress attenuation with increasing R shown in Figure 4.13a. At the same time, an increase in R translates into a decrease in the modulus of the subgrade layer, which controls the vertical strain increase in that layer. This effect overrides the influence of the increased stress attenuation.

For six of the cases examined, the presence of positive (tensile) strains was observed close to the surface up to a depth of 0.4r. A more detailed investigation of these cases identified that positive strains were developed when n = 0.5, $\nu_{hv} = 0.4$, and R > 1, with R = 10 having the most significant impact. Contours of the vertical strain for this last case are shown in Figure 4.15a. Given that the model is elastic, tensile strains for $\nu_{hv} = 0.4$ can be expected at locations where the horizontal stress is larger than the vertical stress, and the effect of the horizontal strain on the vertical strain is significant (high Poisson ratio). To further investigate the influence of ν_{hv} on the measured vertical strain, further analyses were performed for all the cases that showed incremental tensile strains utilizing two different ν_{hv} inputs: 0.1 and 0.4. Figure 4.15 shows that as the input value for ν_{hv} decreases from 0.4 to 0.1, the region in which the model predicts vertical tensile strains is reduced.

Overall, the results of the analyses conducted for loading of a rigid plate (Figure 4.13) are similar to those described above for a flexible plate. Again, an increase in R leads to more rapid stress attenuation, and modulus anisotropy ratio and Poisson ratio have a secondary effect. The occurrence of tensile strains was not observed in any of the cases analyzed with a rigid plate.

Finally, Figure 4.16 illustrates the variation of the plate settlement as a function of n and R for the case of a flexible plate. In this figure, which includes the results for 9 cases, values of the plate settlement are normalized by the settlement calculated for the same plate type with the base case input parameters (isotropic, homogeneous conditions with $\nu_{hh} = \nu_{hv} = 0.3$). The other cases of analysis for R = 5 and R = 10 are not included in the plot given the positive strains generated at the surface. As expected, the plate settlement increases with an increase in layer modulus ratio R, given that a weaker subgrade modulus is introduced in the model. More interestingly, the figure also shows that the modulus anisotropy ratio, n, of the 0.2 m subbase layer continues to affect the plate settlement. Specifically, for all values of R, the plate settlement increases with an increase of the modulus anisotropy ratio, n, of the subbase. This effect is especially significant for $R \leq 1$, where the contribution to the overall settlement from the upper layer increases.

For example, for R = 0.5 and R = 1, as n increases from 0.5 to 1, the plate settlement increases by 26% and 15%, respectively.

4.3 Conventional Interpretation of M_r Plate Load Test Data

4.3.1 Theoretical Framework

For homogenous ground conditions, conventional interpretation of the plate load test data makes use of Boussinesq's (1885) half space solution for evaluating the elastic modulus of the tested soil material. In addition to material homogeneity, this approach assumes isotropic linear-elastic material behavior.

$$M_r = \frac{(1-\nu^2) \cdot q \cdot r}{\delta_r} \cdot f \qquad \text{(Eq. 4.3)}$$

where,

M_r = resilient modulus used here to represent the elastic modulus,

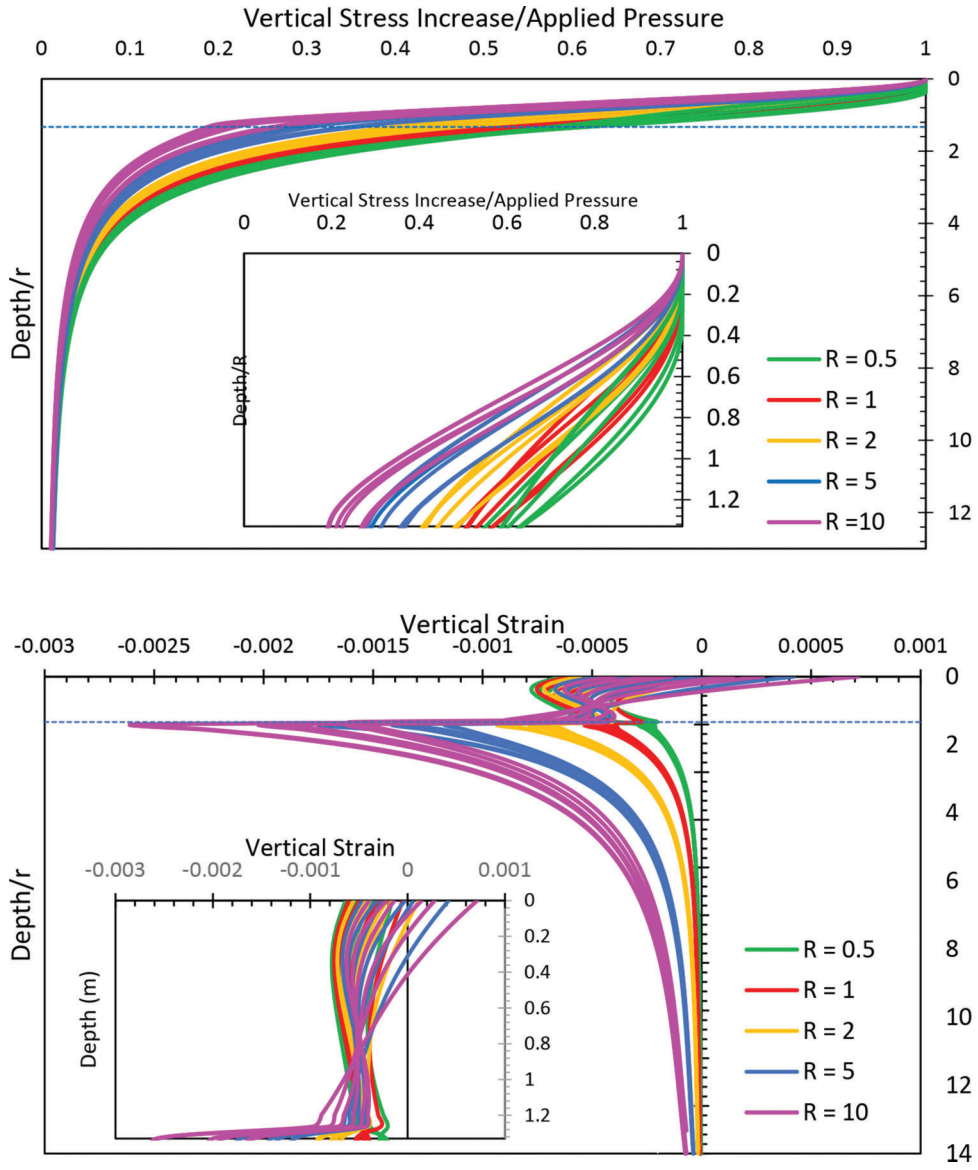

Figure 4.13 Effect of stratification on (a) vertical stress increase, and (b) vertical strain with depth for loading of a flexible plate (r is plate radius).

δ_r = resilient (elastic) deflection of the plate,
ν = Poisson's ratio,
q = applied contact stress,
r = radius of bearing load plate, and
f = shape factor.

The equation can also be used to analyze data for layered systems to obtain what is referred to as a composite modulus.

As discussed in Chapter 2, the shape factor f that appears in Equation 4.3 is intended to reflect the stress distribution beneath the plate. Based on Ullitdz (1987), in the case of a rigid plate on a granular material, f is generally assumed to be equal to 8/3 or $\pi/2$, depending on whether the loaded soil is cohesionless or cohesive (White & Vennapusa, 2017). Additionally, use of Equation 4.3 requires assuming a value of the Poisson ratio.

Interpretation of the APLT tests performed on a two-layer system relies on the data obtained from the sensor kit that provides resilient deflections at radii of 2r, 3r, and 4r away from the plate center. This data is used in combination with measurements of the plate deflection to perform the layered analysis of two-layer pavement system, as described by White and Vennapusa (2017); White et al. (2016, 2019). This approach, which is herein referred to as the conventional approach for the interpretation of plate load tests on two-layer systems, involves two main steps. In the first, the equation below (AASHTO, 1993) is used to calculate the modulus of the subgrade layer from the resilient deflection measurements at radii 2r, 3r, and 4r:

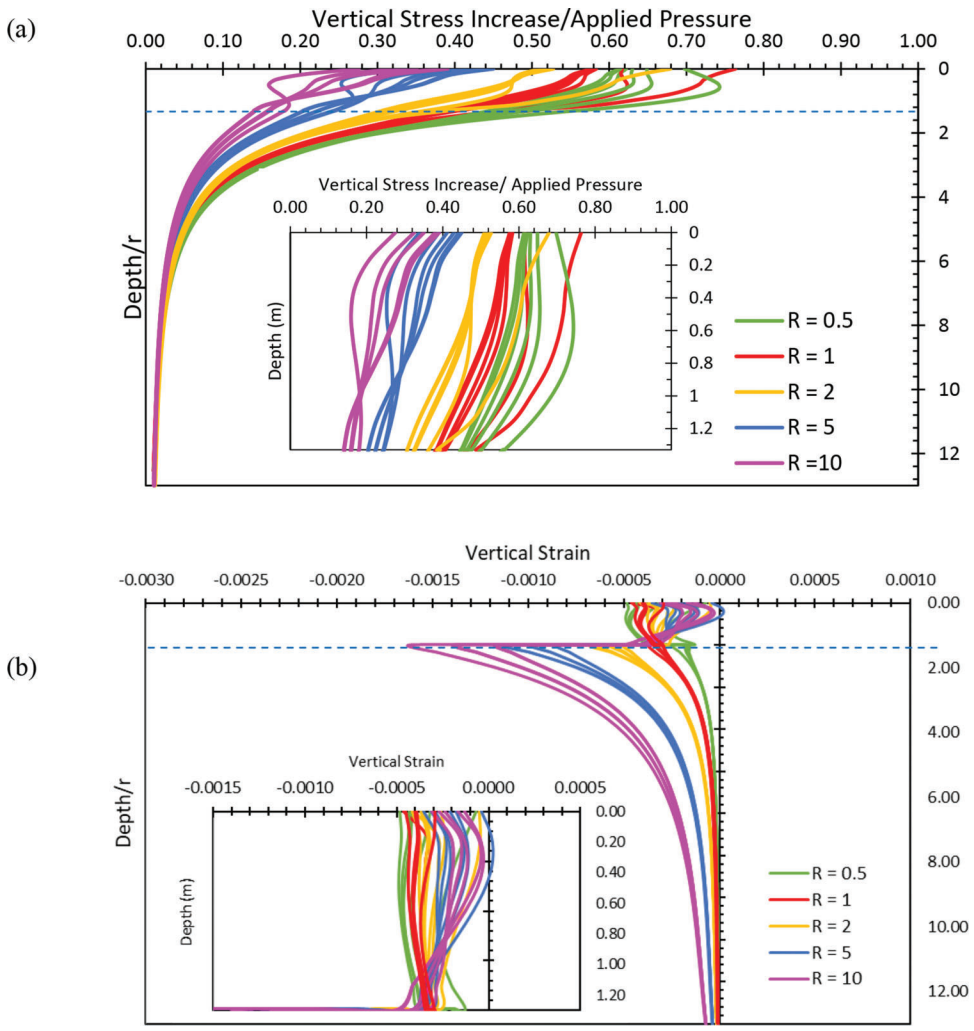

Figure 4.14 Effect of stratification on (a) vertical stress increase, and (b) vertical strain with depth for loading of a rigid plate (r is plate radius).

$$M_{rsubgrade} = \frac{(1-\nu^2)\cdot P}{\delta_{r,r'}\cdot \pi \cdot r'} \qquad \text{(Eq. 4.4)}$$

where,

$M_{rsubgrade}$ = resilient modulus of subgrade used here to represent the elastic modulus,

ν = Poisson's ratio (most commonly assumed as 0.4 for both layers),

P = applied cyclic load,

r′ = radial distance away from plate center where the surface settlement (2r, 3r, 4r in the APLT setup), and

$\delta_{r,r'}$ = resilient deflection of the plate at r′ = 2r, 3r, and 4r away from the plate center.

While AASHTO (1993) states that the design resilient modulus should be calculated from the sensor closest to the loading plate that is still outside of 0.7 times the "radius of the stress bulb at the subgrade-(subbase) interface," this study followed the approach used by White and Vennapusa (2017) based on which the subgrade resilient modulus is given by the lowest of the values of M_r derived from calculations using Equation 4.4 for the three locations at r′ = 2r, 3r, and 4r. This value is then used to compute the modulus of the subbase layer utilizing the measured plate settlement data, the Boussinesq solution and the Odemark equivalent-layer-thickness method. The latter is an approximation method used in the analysis of pavement systems, to convert a multi-layer structure into an equivalent single layer (Horak et al., 2015). This method is incorporated into Bousinessq's settlement expression to compute the modulus of the top layer (which for the tests performed in this project is the subbase) through Equation 4.5.

$$\delta_r = (1-\nu^2)\cdot\Delta\sigma_0\cdot r\cdot f \left[\frac{1}{M_{r(subbase)}\cdot\sqrt{1+\left(\frac{h}{r}\cdot\sqrt[3]{\frac{M_{r(subbase)}\cdot(1-\nu_1^2)}{M_{r(subgrade)}\cdot(1-\nu_2^2)}}\right)^2}} + \frac{\left(1-\frac{1}{\sqrt{1+\left(\frac{h}{r}\right)^2}}\right)}{E_{(base)}}\right] \qquad \text{(Eq. 4.5)}$$

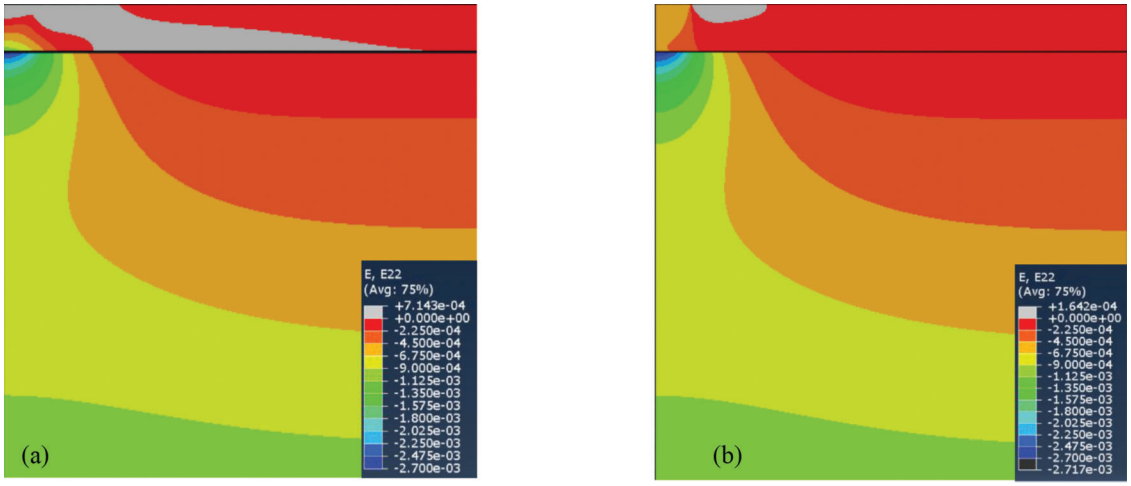

Figure 4.15 Vertical strain contours under a uniformly loaded ($\Delta\sigma$ = 275 kPa) flexible plate on a two-layer model having R = 10 and n = 0.5 with (a) ν_{hv} = 0.4, and (b) ν_{hv} = 0.1.

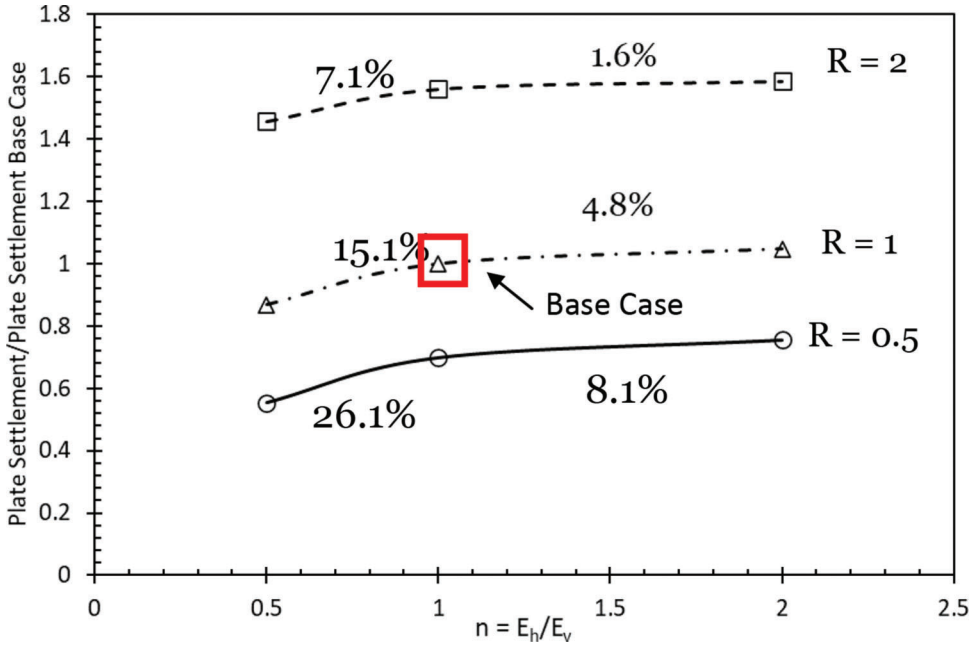

Figure 4.16 Effect of modulus anisotropy ratio (n) and layer modulus ratio (R) on settlement under uniformly loaded flexible plate. The percentages shown refer to the increase in normalized plate settlement with increasing n under constant R.

where,

$M_{r(subbase)}$ = modulus of subbase layer,
$M_{r(subgrade)}$ = modulus of subgrade layer,
$\nu_{1,2}$ = Poisson ratios of base and subgrade layer (generally assumed as 0.4 for both layers),
$\Delta\sigma_0$ = applied contact cyclic stress,
r = radius of load plate,
f = shape factor (as the top layer loaded by the rigid plate is comprised in this testing program by a granular material, f = 8/3),
δ_r = resilient deflection of the plate, and
h = thickness of the subbase layer.

There are several assumptions associated with employing this approach for calculating the elastic modulus of subgrade and subbase. First, all the assumptions inherent in the use of the Boussinesq solutions (e.g., isotropic elasticity, fixed value of the shape factor, selection of Poisson ratio), as discussed earlier in this report, continue to apply, and affect the predicted values of the moduli in the same way. Additional assumptions are associated with the calculation of the subgrade modulus from resilient deflection measurements at locations 2r, 3r, and 4r away from the center of the plate using Equation 4.4. The first is that, moving away from the center of the

plate, the contribution of the subbase layer to the deflection measured at the surface is negligible, i.e., that the deflection is controlled by the compression of the subgrade layer. The second assumption is that the distributed load from the plate at the surface can be approximated by a concentrated load acting along the axis of symmetry of the plate at the interface between subbase and subgrade. Depending on the site conditions, this method may produce unreliable estimates of the subgrade modulus. For example, White and Vennapusa (2017) note that based on Ullidtz (1987) the application of the two-layered analysis using the Odemark method should be restricted to "conditions with moduli values decreasing with depth (i.e., hard over soft), preferably by a factor of at least two between the consecutive layers." This condition is not met in the tests performed in this research project on the cement-treated strip. There is also a broader question related to the degree to which elasticity can be used to interpret the surface deflection basin. These questions are addressed further below. Finally, note that erroneous predictions of the modulus of the subgrade based on the use of Equation 4.4 will be mapped to the value of the subbase modulus predicted using Equation 4.5.

4.3.2 Analysis of MR Tests at S-BRITE Site

The data from the MR APLT tests performed at the S-BRITE site were first analyzed using the approaches outlined above. The results of these analyses, which were conducted by the company that performed the APLT testing program, are summarized in Table B.1 and Table B.2.

Table B.1 provides M_r values for both the untreated and cement-treated subgrade derived from the analysis, using Equation 4.3, of the data from the 5 tests performed directly on the subgrade using an 18-in diameter plate. For each test, six values are presented corresponding to the six loading stages that followed the conditioning stage. A constant value of the shape factor, $f = \pi/2$ and a Poisson ratio, ν, equal to 0.4 were assumed in all calculations. As shown in the table, the applied cyclic stresses deviated somewhat from the target nominal stresses. For simplicity, the subsequent text references the nominal maximum stresses applied during the six loading stages (4, 8, 13, 18, 28, and 38 psi) when discussing the tests results collectively.

Focusing on the results for the two tests at the locations (J6 and L3) on the *untreated subgrade*, for which the assumptions of material homogeneity on which the formulation is based more closely approximate actual field conditions, the following is observed.

- In each test over the range of the applied cyclic stresses examined (4–38 psi), M_r values vary by less than 15%.
- Estimates of M_r obtained at the two testing locations differ significantly, with M_r = 3,680–4,240 psi at location J6 and M_r = 10,727 psi–11,965 psi at location L3. For reference, M_r data obtained from laboratory resilient modulus tests performed according to AASHTO T 307-99 on soil collected from the site (K. Gupta, personal communication, February 2023) ranged between 7,900 and 14,700 psi (note that in lab tests the maximum applied deviatoric stress was 10 psi).
- The discrepancy in the values of M_r estimated at the two testing locations is consistent with the LWD data collected at the site (2.214 mm and 0.413 mm average deflections for locations J6 and L3, respectively).

The same approach based on Equation 4.3 was applied to derive M_r values of the subgrade from the tests performed at locations C5, J2, and M2 on the *cement-treated subgrade* (see Table B.1 in Appendix B). Note that in this case, the assumption of homogeneity is not representative of the actual field conditions as, due to the treatment, the top 14″ of the soil are significantly stiffer than the underlying natural soil (by a factor of five or more based on laboratory tests on the same soil (Gupta, personal communication, 2023).

The following is observed.

- All tests show the same trend of increasing modulus with increasing applied cyclic stress (an increase of 50%–100% as the applied cyclic stresses goes from 4 to 38 psi).
- Collectively the values of M_r derived for the cement-treated subgrade from this analysis vary from ~26,700–40,400 psi under the smallest applied cyclic stress of 4 psi to 40,600–70,100 under the highest applied cyclic stress of 38 psi. For reference, M_r data obtained from laboratory resilient modulus tests performed according to AASHTO T 307-99 (AASHTO, 2021a) on the cement treated soil (Gupta, personal communication) ranged between ~21,000 and 75,000 psi after 28 days of curing (note that in lab test maximum applied deviatoric stress = 10 psi).
- For any given applied cyclic stress, M_r values estimated at the three testing locations differed by ~35%–50%. This variation does not find direct correspondence in the LWD deflections measured at the same locations.

Table B.2 provides a summary of the M_r values for both subgrade and subbase derived from the five *tests conducted on the subbase layer* (3 on the cement-treated strip and 2 on the untreated strip) using the approach for two-layer systems outlined in Equation 4.4–Equation 4.5. This analysis, conducted by the company that performed the APLT testing program, assumed values of the Poisson ratio of 0.4 for both layers and a shape factor of 8/3. The following is observed.

- Values of $M_{rSubgrade}$ predicted using off center surface deflections using Equation 4.4 are consistently greater than those derived from tests performed directly on the subgrade, even once stress attenuation effects are accounted for (based on Figure 4.13a stress attenuation at the subbase-subgrade interface varies between 40% and 80% depending on the layer modulus ratio R). The difference is less than 50% in the case of the cement-treated subgrade, but much more significant in the case of the untreated subgrade (factor of 3 or greater), and in particular for test J6 (weakest subgrade conditions).
- For all tests, values of $M_{rSubgrade}$ predicted using off center surface deflections show no consistent pattern of variation with stress level. In particular, for the case of the cement-treated the $M_{rSubgrade}$ data do not exhibit the same trend of increasing modulus with increasing applied

stress observed for the data derived from the tests performed directly on the subgrade.
- M_r values of the aggregate subbase derived from the tests on the cement-treated strip (30,000–88,000 psi across three tests and six stress levels) significantly exceed the values derived from the tests on the untreated strip (3,600–22,400 psi across two tests and six stress levels).
- Values of the layer modulus ratio (R) derived from the tests on the cement treated strip show an increasing trend with stress level (with the exception of the data for the lowest stress level in test CTM2SG), with the majority of the values falling in the 0.4–0.9 range.
- Values of the layer modulus ratio (R) derived from the tests on the untreated strip are generally smaller (R = 0.40-0.64), with no clear trend with stress level.

Finally, Table B.3 summarizes values of the universal model parameters (k_1, k_2, k_3—see Equation 2.2 in Chapter 2) derived for the aggregate subbase from each of the five plate load tests performed at the site, based on analysis performed by the company that conducted the APLT testing program. The assumptions used for this analysis are discussed in Ingios (2021). For reference Table B.3, also includes statistics for these same parameters from the FHWA study (Yau & Von Quintus, 2002) that compiled data for 423 unbound aggregate base and subbase materials (see also Figure 2.5 in Chapter 2). As seen in Table B.3, the values of k_1, k_2, k_3 vary greatly across the tests, even for the tests conducted on the same strip. For example, k_2 values derived from the three tests performed on the cement treated strip alone vary between 0.154 (CT-M2) and 0.833 (CT–C5), effectively covering the entire range reported in the FHWA study based on tests on over 400 aggregate materials. For all tests on both strips values of k_1 fall at the high end or above of the range reported for similar materials (FHWA study and additional database assembled for this study, see Figure 2.5). Values of k_3 derived from the five tests values fall outside the range reported for unbound granular materials in the FHWA study and at the low end of the range of values from the database assembled for this study.

4.4 Further Finite Element Analyses of S-BRITE Data

4.4.1 Plate Load Tests on Untreated Subgrade

While the upper portion of the subgrade is compacted, when modeling these tests using ABAQUS, homogeneous conditions were assumed, i.e., the model included a single layer (layer modulus ratio R = 1). Plate geometry and material density values for the FE analyses were based on actual test and site conditions (see Sections 3.2–3.3). For each loading stage, the following iterative procedure was used to derive the modulus of the tested subgrade from the field data.

- An initial estimate of the modulus obtained from the Boussinesq equation (with $f = \frac{\pi}{2}$ and $\nu = 0.4$) is used as input for the FE analysis. Note that this is the value of M_r obtained from the conventional analysis discussed previously.
- The resulting plate settlement obtained from ABAQUS is then compared to the field measurement obtained under that stress level. The input modulus is adjusted, and the analysis repeated until the difference between the predicted and measured values of the plate settlement falls below 1%.

As the results of the parametric study presented previously (Figure 4.10) demonstrate that the plate settlement is affected by the soil's degree of modulus anisotropy, this analysis was repeated for three different values of the soil's modulus anisotropy ratio, n (0.5, 1, 5). Given the secondary effect of the Poisson ratio on the plate settlement (Figure 4.10), all analyses were performed assuming ν_{hh} and $\nu_{hv} = 0.4$ (where a value of 0.4 could not be used as the constraints posed by the thermodynamic requirements for positive strain energy for a cross-anisotropic material were not satisfied, the highest possible value was employed).

Figure 4.17 summarizes the values of M_r obtained from FE analysis of data for the test on the untreated subgrade at location UNTJ6 assuming isotropic conditions (n = 1). Also included in the figure are the values of the modulus derived for each loading stage using the conventional approach discussed previously, which relies on the Boussinesq solution, with $f = \frac{\pi}{2}$ to represent rigid plate loading conditions on a cohesionless soil, and $\nu = 0.4$ (e.g., Vennapusa et al., 2020; White & Vennapusa, 2017; White et al., 2019). As shown in Figure 4.17, the approach based on the Boussinesq solution provides an approximately constant (3,900 $\pm$ 400 psi) value of the elastic modulus across the six cyclic stress levels applied in the test (see also Table B.1). In contrast, the finite element analyses with n = 1 led to values of the modulus that decrease non-linearly with stress level, from 11,250 psi (cyclic stress of 4 psi) to 4,350 psi (cyclic stress of 38 psi). Such a trend of decreasing subgrade moduli values with increasing deviatoric stress is expected and has been reported in the literature (e.g., Maher et al., 2000; Malla & Joshi, 2006; Ooi et al., 2006). The discrepancy between the values of M_r predicted using the FE analyses and the conventional approach is highest at the lowest stress level and diminishes as the stress applied during loading increases (ratio of the values or M_r predicted using the two methods goes from ~3 (4 psi) to 2 (8 psi), to 1.2 (18 psi) to 1.12 (38 psi)).

Data for three stress levels (4, 18, and 39 psi) for the test performed at location UNTL3 were analyzed in a similar manner. Also in this case, the values of the moduli derived from the FE analysis decreased with increasing applied stress (32,600, 16,200, and 13,000 psi for 4, 18, and 39 psi, respectively), in all cases exceeding the values predicted using the Boussinesq solution (10,900; 11,650; and 10,727 psi for the same stress levels). As for the data shown in Figure 4.17, the difference between the two predictions decreased with increasing stress level. Overall, this shows that under the same assumption of isotropic material response, the conventional approach outlined in

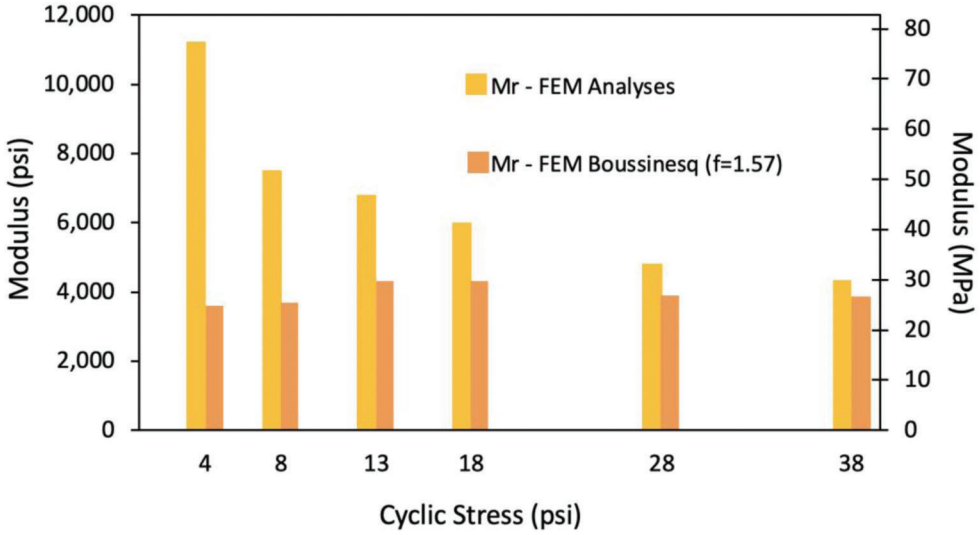

Figure 4.17 FE predictions based on isotropic behavior (n = 1) of resilient modulus for plate load test conducted at UNTJ6SG.

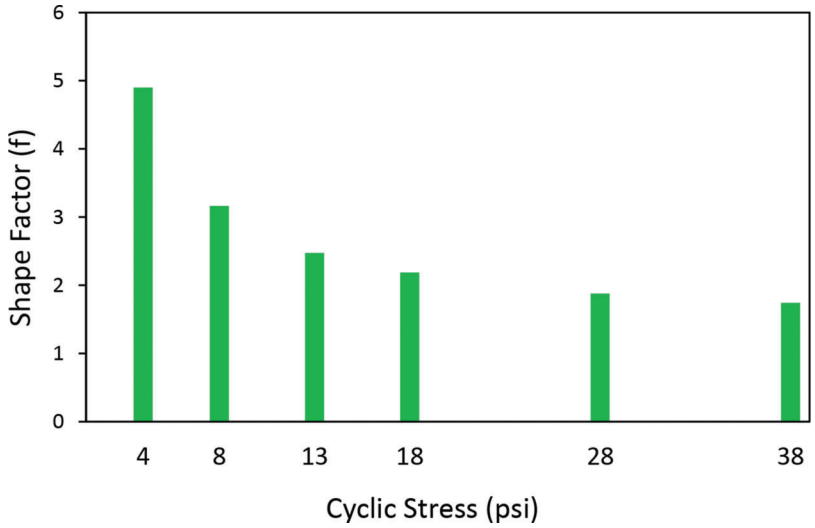

Figure 4.18 Values of shape factor (f) derived from FE analyses (with n = 1) for plate load test conducted at UNTJ6SG location.

Section 4.3 leads to underestimate the modulus, by as much as a factor of 3 for the lowest applied deviatoric stress.

Utilizing Equation 4.3 and the elastic modulus values derived for each stress level from the FE analyses, values of the shape factor were back-calculated for all 6 stress levels (4–38 psi) applied in the field in test UNTJ6-SG. These values which are summarized in Figure 4.18 show that f decreases with increasing stress level, from a maximum value of 4.90 (4 psi applied cyclic stress) to a minimum value of 1.74 for the highest stress (38 psi) applied in the plate load test. The latter value approaches $\frac{\pi}{2}$, the value conventionally used. A similar analysis of the data for test UNTL3-SG yielded similar values of f: 4.65, 2.28, and 1.84 for applied stresses of 4, 18, and 39 psi, respectively. This variation demonstrates that beyond the well-known influence of plate stiffness and stress distribution underneath the loading plate, other factors impact the shape factor, and that assuming a constant a-priori value of the shape factor has no justification and can lead to incorrect values of the modulus.

Further FE analyses were conducted to examine the impact that consideration of the soil's cross-anisotropy has on the predicted values of the elastic modulus, by repeating the iterative procedure described previously for different input values of the soil's modulus anisotropy ratio, n. In these simulations the input value of G_{hv} was set equal to 0.3 times the vertical modulus (equal in this case to M_r) and was thus also adjusted at each iteration.

Figure 4.19 shows the values of M_r predicted for one stress level (18 psi) in test UNTJ6SG. As expected, based on the parametric study presented previously, the modulus increases with increasing value of the modulus

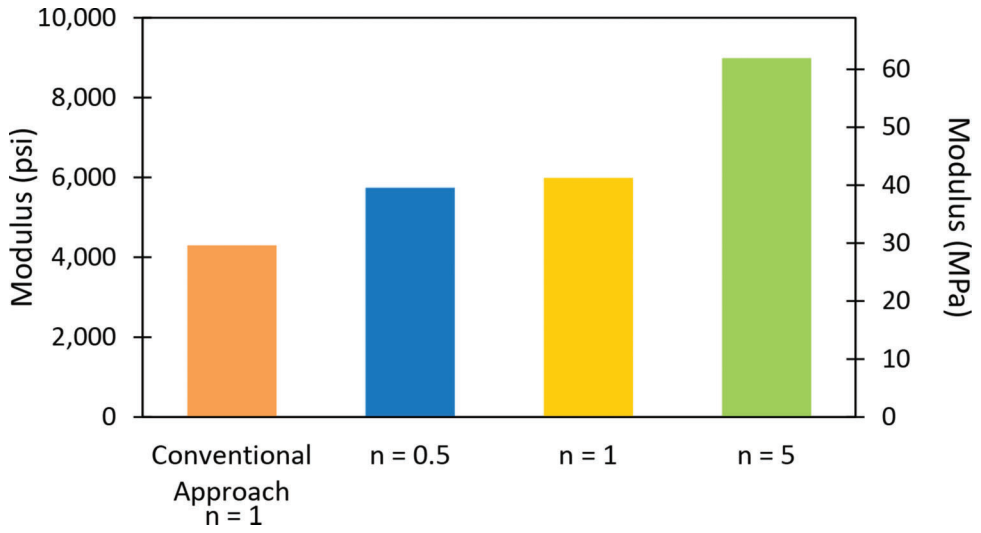

Figure 4.19 Resilient modulus predicted from FE analyses for different values of the modulus anisotropy ratio, n: data for plate load test conducted at UNTJ6SG location (cyclic stress = 18 psi).

anisotropy ratio, n. As field compaction is expected to generate a non-isotropic stress state, material anisotropy should require consideration when analyzing field data.

4.4.2 Plate Load Tests on Cement-Treated Subgrade

Similar analyses can be performed for the tests conducted on the cement-treated subgrade. In this case, the assumption of material homogeneity is clearly not satisfied, and the layer modulus ratio (R) is not known a priori. As a result, only a limited set of data from the test conducted at location CTC5 were re-analyzed with ABAQUS using the iterative procedure described previously. Also, in this case it was observed that the values of M_r derived from the finite element results with n = 1 and R = 1 exceeded the values predicted using the Boussinesq equation (e.g., by ~25%, from ~70,000 to ~87,000 psi (483 to 600 MPa) for the 40-psi cyclic stress level in test CTC5SG). While representing an improvement relative to the value obtained from the conventional approach based on Equation 4.3 this estimate of the modulus continues to rely on the unrealistic assumption of material homogeneity.

As suggested by the results presented in Section 4.3.2, consideration of the presence of the softer underlying untreated soil (i.e., R>1) leads to predict even larger values of M_r for the cement treated soil. For example, for the same data set (40 psi stress level in test CTC5SG), the FE analysis performed following the same iterative procedure but assuming R = 5 instead of R = 1, yields an estimate of the M_r of the cement-treated subgrade of ~217,000 psi (1,500 MPa).

4.4.3 Plate Load Tests on Compacted Aggregate

4.4.3.1 Validity of Equation 4.4 for deriving $M_{rSubgrade}$ from off-center surface deflections. To start, it is of interest to assess the accuracy of Equation 4.4 in predicting the subgrade modulus. This was done using as a reference the results of the FE analyses presented earlier in this chapter for an isotropic two-layer system loaded through a rigid plate, considering three different values (0.5, 1, and 5) of the layer modulus ratio, R. In each case, the stress applied on the plate was 276 kPa (~40 psi), the modulus of the top subbase layer was held constant and equal to 310 MPa (44,962 psi), while the modulus of the subgrade layer was controlled by the layer modulus ratio, R (and equal to 620 (89,923 psi), 310 and 62 MPa (8,992 psi), for R = 0.5, 1, 5, respectively). For both layers a value of 0.4 was used for the Poisson ratio.

For each case, the FE analysis produced predictions of the surface deflections at radial distances 2r, 3r, and 4r. These values were then input in Equation 4.4 to calculate "predicted" values of the elastic modulus, the smallest of which (see Section 4.3.1) could then be compared to the known input values used in the FE analyses.

The comparison, presented in Figure 4.20, shows that, relative to the elastic FE results, the use of Equation 4.4 leads to underestimate the subgrade modulus, by a factor of over 2 for all the values of R analyzed.

4.4.3.2 Plate load tests on aggregate compacted on cement-treated subgrade. Additional analyses with ABAQUS focused on data from the three plate load tests performed at the S-BRITE site on the aggregate subbase layer compacted on top of the cement treated subgrade. This set of tests were chosen for further analysis as soil stabilization (by cement or lime treatment) is used in most pavement construction projects in Indiana. Plate geometry and material density values for the FE analyses were based on actual test and site conditions (see Chapter 3). As in the conventional approach, the analysis relied on measurements of off-center surface deflections to derive the modulus of the underlying subgrade.

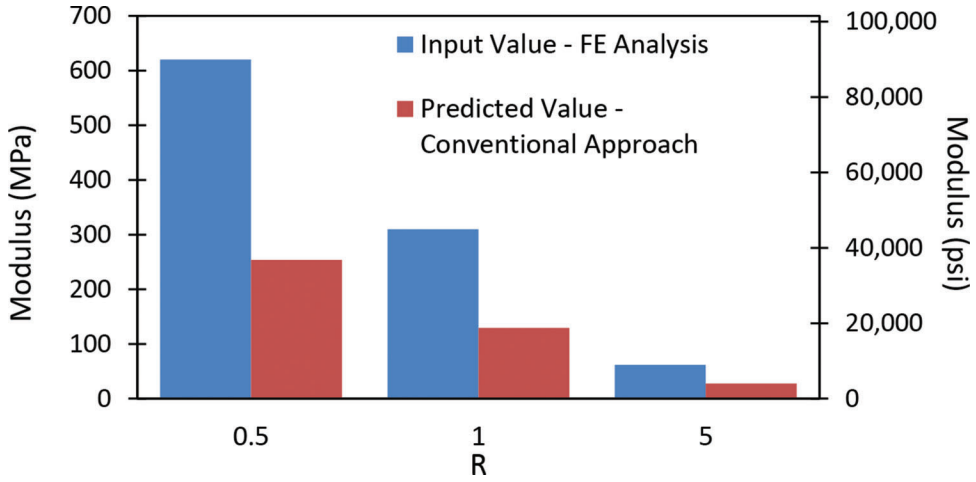

Figure 4.20 Comparison of known values of the subgrade modulus used in the FE analyses to values predicted using Equation 4.4.

The analyses performed using ABAQUS employed the following two-stage iterative procedure.

- Using the measured deflections at 2, 3, and 4r and the plate settlement, initial estimates of M_r for subbase and subgrade a are derived using the conventional approach (Equation 4.4 and Equation 4.5).
- A first FE analysis is performed using the modulus values derived using the conventional approach, and the predicted surface deflections at locations 2r, 3r, and 4r are compared to the field measurements.
- The value of the subgrade modulus is adjusted, and the analysis is repeated. This is continued until the predictions from the FE analysis at all three locations are within 1% of the field measurements.
- Once the value of subgrade modulus is determined using the procedure above, additional FE iterations are performed adjusting the modulus of the upper subbase layer until the predicted value of the plate settlement matches the field measurement.

For each test, this analysis was performed for three different values of the subbase modulus anisotropy ratio (n = 0.5, 1, and 2).

Examples of the results of these analyses for the highest cyclic stress level (39–40 psi (269–276 kPa), depending on the test) are shown in Figures 4.21, 4.22, and 4.23 for tests CTC5SB, CTM2SB, and CTJ2SB, respectively. For all testing locations, relative to the conventional approach, the FE analyses predict subgrade M_r values which are significantly higher and subbase M_r values that are significantly lower. This is expected given the discussion of Equation 4.4 in Section 4.4.3.1. The modulus anisotropy ratio is found to play a significant role on the FE results, with both moduli increasing with increasing n. In particular, for all three tests, the modulus of the subbase layer increases approximately two-fold as n goes from 0.5 to 2: the greater the modulus anisotropy ratio, the greater the difference between the FE results and the values predicted from the conventional analysis. As shown in the figures, the layer modulus ratio R predicted from the FE analyses varies between 0.1–0.2 for all tests, significantly lower than the R values obtained using the conventional approach (R = 0.7–1.2).

Similar results are observed at other stress levels, with increasing deviation from the values obtained using the conventional approach as the applied stress decreases. This is illustrated in Figure 4.24, which shows predictions of subbase and subgrade moduli at the CTC5SB testing location for the 8-psi cyclic stress loading stage.

Comparison of the subgrade modulus values derived from the tests performed on the aggregate subbase based on the off-center surface deflections to those obtained directly from the plate load test on the (cement) treated subgrade continues to show some discrepancies. These are, however, reduced once the effect of the layer modulus ratio on stress level attenuation (see Figures 4.13 and Figure 4.14) is considered, and consideration is given in the analysis of the tests performed on the subgrade to the presence of the underlying softer layer (i.e., by assuming a value of R>1). For example, in the case of test CTC5SB (40 psi stress level), the value of M_r of the cement-treated layer predicted for n = 1 from the off-center measurements is ~290,000 psi (2,000 MPa). This falls in the range of values estimated from the analysis of the data obtained from the test performed directly on the cement-treated subgrade at the same location assuming R = 5 (M_r = 217,000–361,000 psi for 8–40 psi stress levels).

4.4.3.3 Plate load tests on aggregate compacted on untreated subgrade. Analyses like those discussed in the previous section were conducted for the plate load tests performed on the aggregate subbase layer constructed on top of the untreated subgrade. Figure 4.25 summarizes the values of $M_{rSubbase}$ and $M_{rSubgrade}$ obtained from the analysis of the data for test UNTJ6SB (38.5 psi stress level). The following is observed.

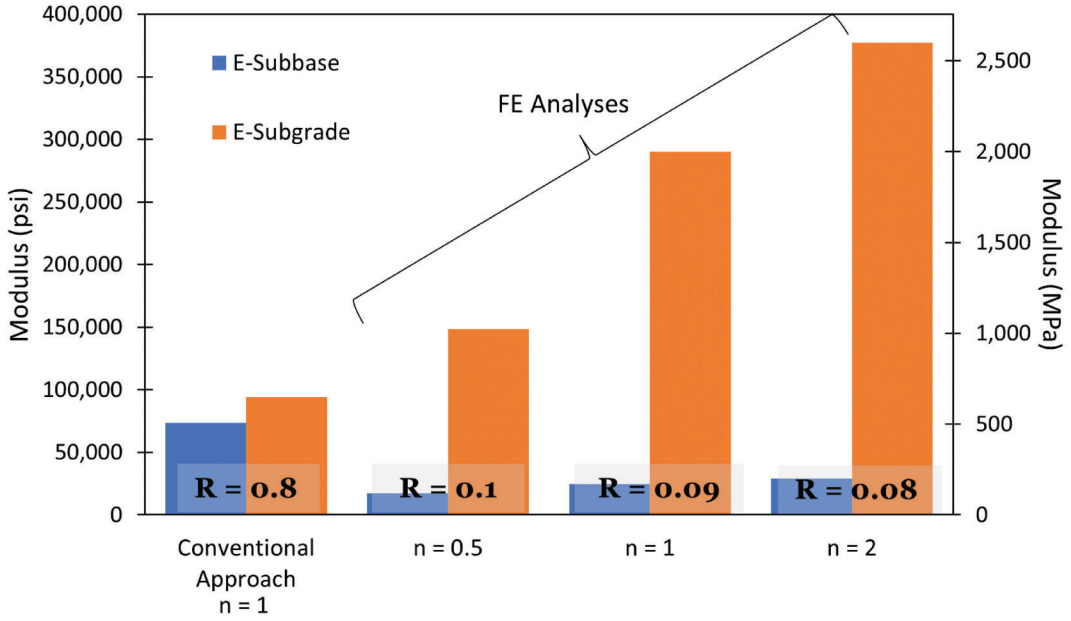

Figure 4.21 Comparison of the predictions of subbase and subgrade moduli from tests CTC5SB obtained using the conventional approach and FE analyses with different values of the modulus anisotropy ratio (n) (data for 40 psi (276 kPa) applied cyclic stress).

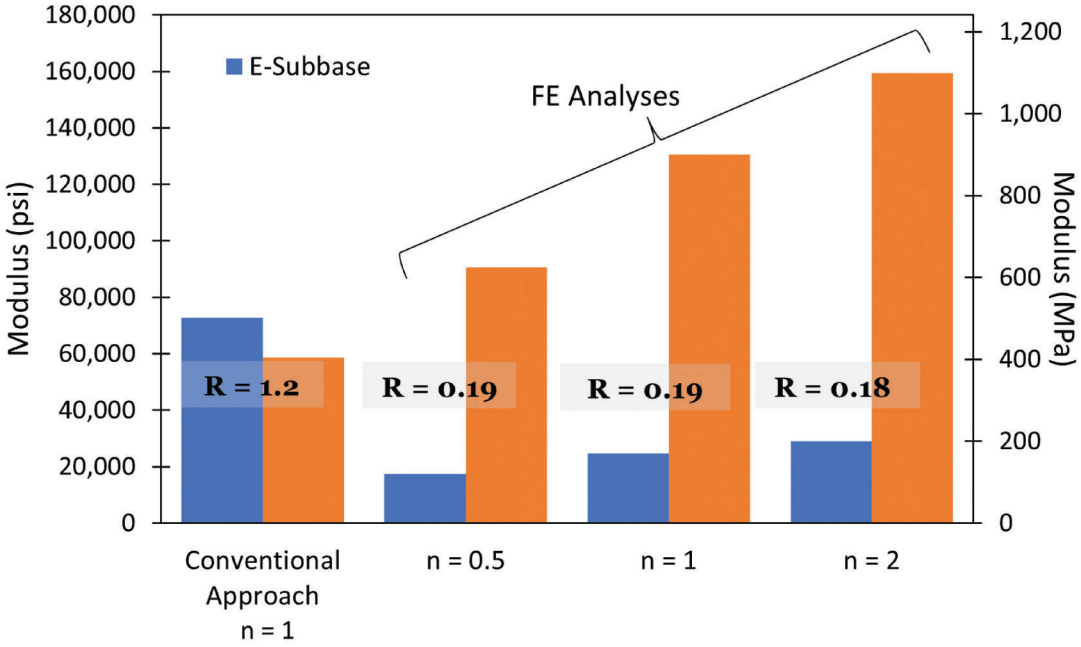

Figure 4.22 Comparison of predictions of subbase and subgrade moduli from test CTM2SB obtained using the conventional approach and FE analyses with different values of the modulus anisotropy ratio (n) (data for 40 psi (276 kPa) cyclic stress).

- As in the case of the tests on the cement-treated strip, the iterative analysis with ABAQUS yields a value of $M_{rSubgrade}$ greater than $M_{rSubbase}$. For the highest cyclic stress (38.5 psi) this corresponds to a layer modulus ratio R of 0.12. This is in the range of values shown in Figures 4.21, 4.22, and 4.23 for the cement treated strip, despite the very different nature of the subgrade.
- As in the case of the tests on the cement-treated strip, the analysis yields a higher $M_{rSubgrade}$ and lower $M_{rSubbase}$ relative to the estimates based on the conventional approach.

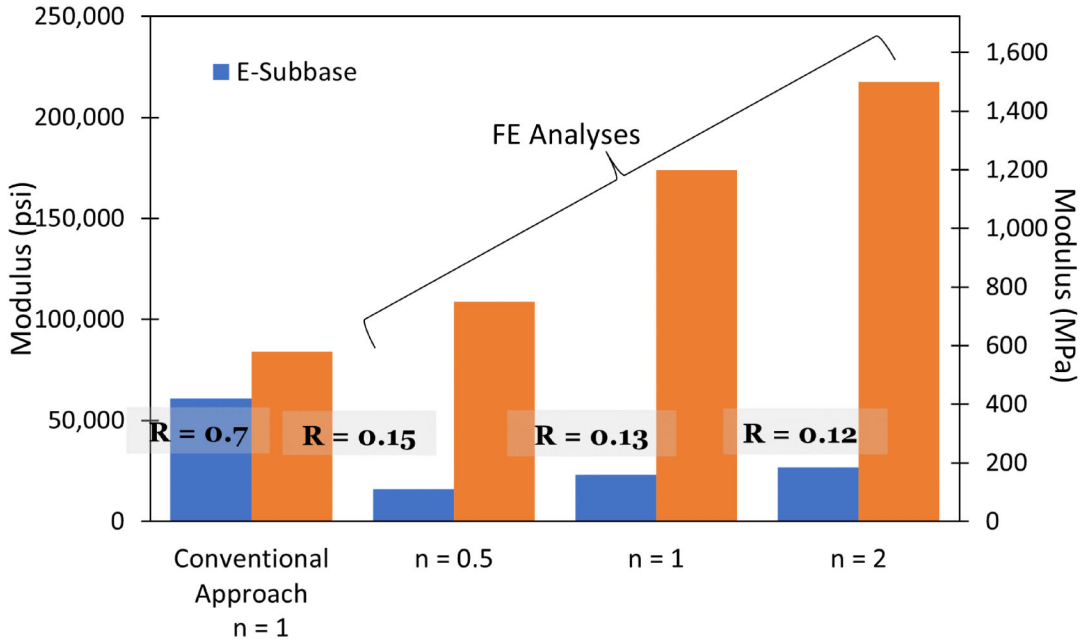

Figure 4.23 Comparison of predictions of subbase and subgrade moduli from test CTJ2SB obtained using the conventional approach and FE analyses with different values of the modulus anisotropy ratio (n) (data for 39 psi (269 kPa) cyclic stress).

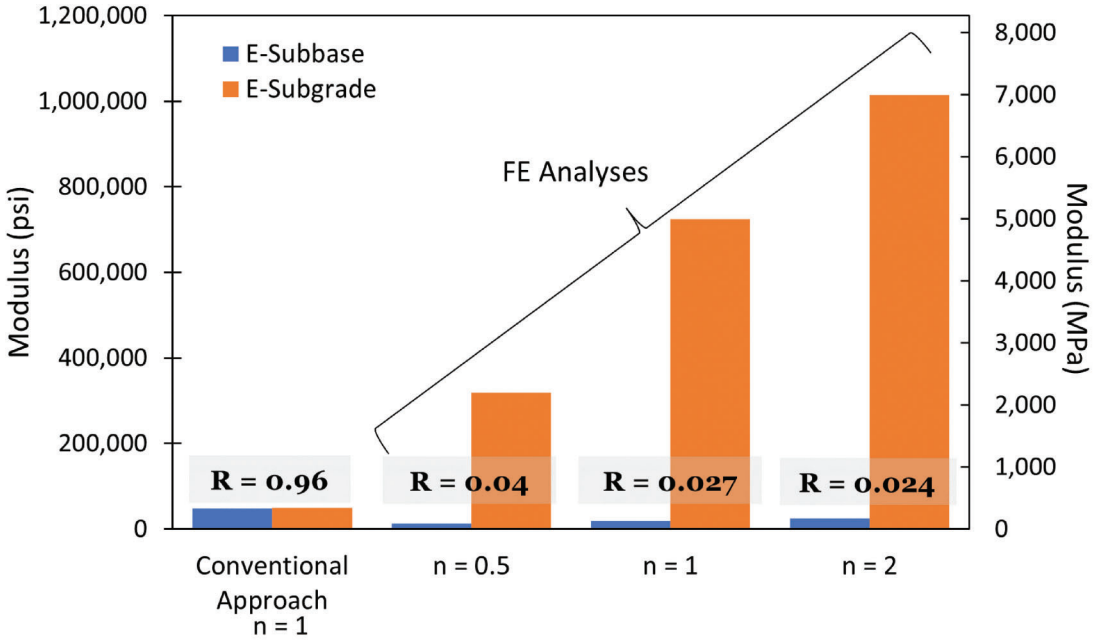

Figure 4.24 Comparison of predictions of subbase and subgrade moduli from test CTC5SB obtained using the conventional approach and FE analyses with different values of the modulus anisotropy ratio (n) (data for 9.4 psi (65 kPa) cyclic stress).

- As seen in the case of the tests on the cement-treated strip, despite the relatively small thickness of the subbase layer, the subbase modulus anisotropy ratio (n) has a significant influence on the values of $M_{rSubgrade}$ and $M_{rSubbase}$ derived from the FE analysis, with both moduli increasing with increasing n.
- The value of $M_{rSubgrade}$ predicted from the off-center surface deflections using ABAQUS significantly exceed those derived from the analysis of the tests performed directly on the subgrade. For example, compare $M_{rSubgrade}$ = 24,650 psi (~170 MPa) (Figure 4.25) to the values reported in Figure 4.17 for cyclic stresses of 8–18 psi (corresponding to stress attenuations of 50%–80%), which fall below 7,500 psi (~52 MPa). The same discrepancy was observed in the results obtained using the conventional approach (see Section 4.3.2 and Tables

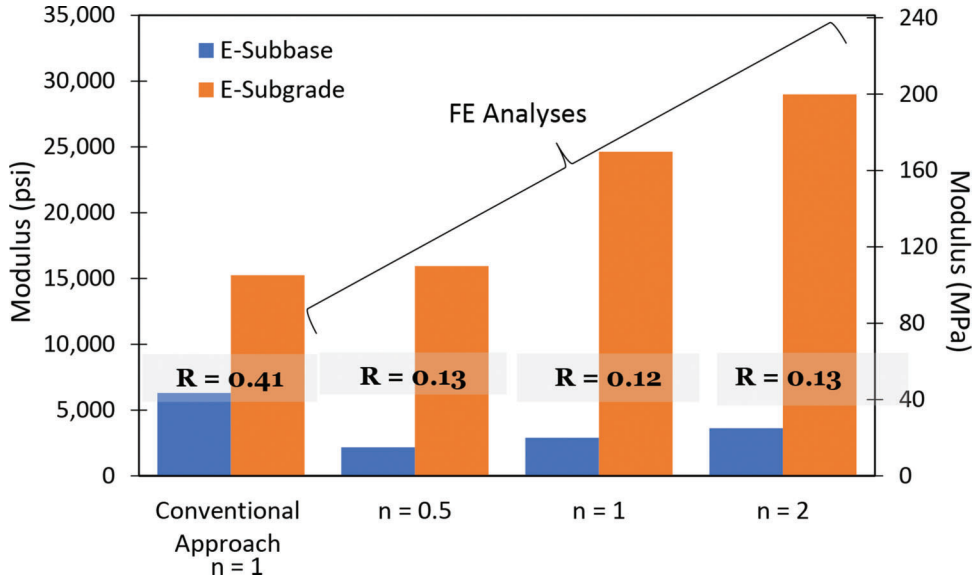

Figure 4.25 Comparison of predictions of subbase and subgrade moduli from test UNTJ6SB obtained using the conventional approach and FE analyses with different values of the modulus anisotropy ratio (n) (data for 38.5 psi (265 kPa) cyclic stress).

B.1–B.2). This may arise from the fact that the test on the subgrade was performed after a complex history of loading produced by the test previously conducted at the same location on the overlying layer. Additionally, there is evidence from experimental observations (e.g., Bourdeau, 1986) that the deflection basin predicted from elasticity is wider than what is observed both in the field and in the lab. As a result, reliance on off-center surface deflections for deriving $M_{rSubgrade}$ leads to overestimate $M_{rSubgrade}$.

- Finally, values of $M_{rSubbase}$ are significantly lower than those estimated for the same aggregate from the tests on the cement-treated strip (e.g., compare $M_{rSubbase}$ = 2,900 psi for n = 1 in Figure 4.25 to the values (~23,200–24,600 psi) almost an order of magnitude greater reported in Figures 4.21, 4.22, and 4.23). Note that the same discrepancy was observed in the moduli derived using the conventional approach (see Tables B.1–B.2).

This last observation warrants additional discussion given the specific focus of this work on the modulus of aggregate bases and subbases. A number of factors can contribute to the discrepancy, and exact correspondence of the values of $M_{rSubbase}$ derived from the two strips should not be anticipated. To start with this may be due to differences in the state of bulk compaction of the aggregate layer. As discussed in Chapter 3, different procedures were followed in constructing the aggregate layer on the two strips (single lift on the untreated strip versus two lifts on the cement-treated strip). The presence of a stiffer underlying layer is also generally considered to promote more effective compaction. Dry unit weight values of the aggregate layer measured using the nuclear density meter (see Table 3.3 in Chapter 3) in proximity to the testing locations on the untreated strip fall, indeed, slightly below those measured in proximity to the testing locations on the cement-treated strip (133–133.6 pcf for locations UNTJ6 and UNTL3 vs. 134.8–139.2 pcf for locations CTC5, CTM2, and CTJ2). The difference in interface conditions between subbase and subgrade (smoother in the case of the cement-treated subgrade) between the two strips may also play a role, possibly by contributing to different degrees of compaction-induced modulus anisotropy. Overall, these factors do not appear sufficient to explain the ten-fold difference in modulus highlighted previously. Instead, they raise questions on the method used to derive the subbase modulus. As any error in estimating $M_{rSubgrade}$ will affect the modulus estimated for the overlying subbase layer, it is proposed here that reliance on off-center surface deflections measured in the field to derive $M_{rSubgrade}$ leads to overestimate the true modulus of this material, and as result to underestimate $M_{rSubbase}$. It is suggested that, in general, tests performed directly on the subgrade will provide more reliable estimates of $M_{rSubgrade}$. Additional analyses of the data for test UNTJ6SB were conducted with n = 1 using as input for the subgrade modulus values derived from the tests performed directly on the subgrade (Figure 4.22). These analyses yield values of $M_{rSubbase}$ closer to those derived for the cement-treated strip. For example, for the data obtained for a cyclic stress level of 38 psi in test UNTJ6-SB, using as input $M_{rSubgrade}$ = 5,800 psi (based on Figure 4.22) leads to an estimate of $M_{rSubbase}$ of 11,600 psi (four times greater than the value shown in Figure 4.25).

5. ANALYSIS AND INTERPRETATION OF STATIC AND RDL PLATE LOAD TESTS

5.1 Introduction

In addition to the MR tests analyzed in Chapter 4, the plate load testing program at the S-BRITE site also included six extended cycle performance tests with randomly distributed load (RDL) performed on the testing strips and three static plate load tests performed

on the neighboring pit filled with compacted aggregate. Details on the testing locations, setup and loading protocols are presented in Chapter 3.

Section 5.2 summarizes the analysis of the three static load tests, which focused on deriving values of the angle of internal friction from the ultimate bearing pressure that are required for estimating the stability of pavement subbases to construction loading (e.g., see Getchell et al., 2020).

Section 5.3 presents the analysis of the results of the RDL tests performed on the two strips and discusses the validity of existing models relating the increase in permanent deformation with number of cycles to describe the data obtained at the S-BRITE site.

5.2 Analysis of Static Tests

5.2.1 Derivation of Aggregate Angle of Internal Friction from Plate Load Tests

Plate load tests, when pursued to failure, can provide a measure of the soil ultimate bearing capacity. Although the resulting ultimate bearing pressure should not be extrapolated to larger foundations because of scale effects, especially on stratified ground, the three static plate load tests (see Chapter 3) that were performed at the S-BRITE site, in a pit filled with compacted aggregate and deep enough for the boundaries not to interfere with the bearing capacity mechanism, provide the opportunity to estimate the angle of internal friction of the material. Data from these tests include plate settlement in function of time for each load increment, as well as load versus final settlement curves, which are used in this section.

There exist several approaches in the literature for determining the bearing capacity from load-deformation curves in plate load tests (Bowles, 1996; Garg, 2004; Sowers & Sowers, 1970). The method proposed by Sowers and Sowers (1970) defines the ultimate bearing capacity as the intersection of the tangents of the load deformation curve or the point in the curve which defines a break or the maximal curvature point. Following this method (Figure 5.1), depending on the points selected for drawing the tangents, values of ultimate bearing pressure ranging between 117 and 129 psi (806–889 kPa) are obtained from the 12-in diameter plate load test data. Similar determinations of the ultimate bearing capacity for the other two tests, using the Sowers and Sowers (1970) method, are shown in Figure 5.2 and Figure 5.3.

Computations were performed using the general bearing capacity equation for square footings of the same surface area as the circular testing plates. Bearing capacity factors in the equation were according to Vesic (1963), and the soil unit weight was assumed equal to 134.8 pcf (21 kN/m^3).

Comparison with the theoretical results show that the ultimate bearing capacity values from the three static tests (Table 5.1) correspond to an angle of internal friction in the 48° to 50° range.

This is consistent with values reported in the literature for aggregate materials that were tested under similarly low confining stresses, as discussed in the synthesis presented in an earlier JTRP study by Getchell et al. (2020).

5.2.2 Remark on the Mechanism of Bearing Capacity Failure of Coarse-Grained Soil

The mechanism of failure for small-scale footings on sand with various states of compaction was demonstrated by Vesic (1963). A "general shear" failure (Figure 5.4a) is observed for dense-behaving sands (i.e., dilating under shear), whereas loose-behaving sand (i.e., compressing under shear) exhibit a punching mode of failure (Figure

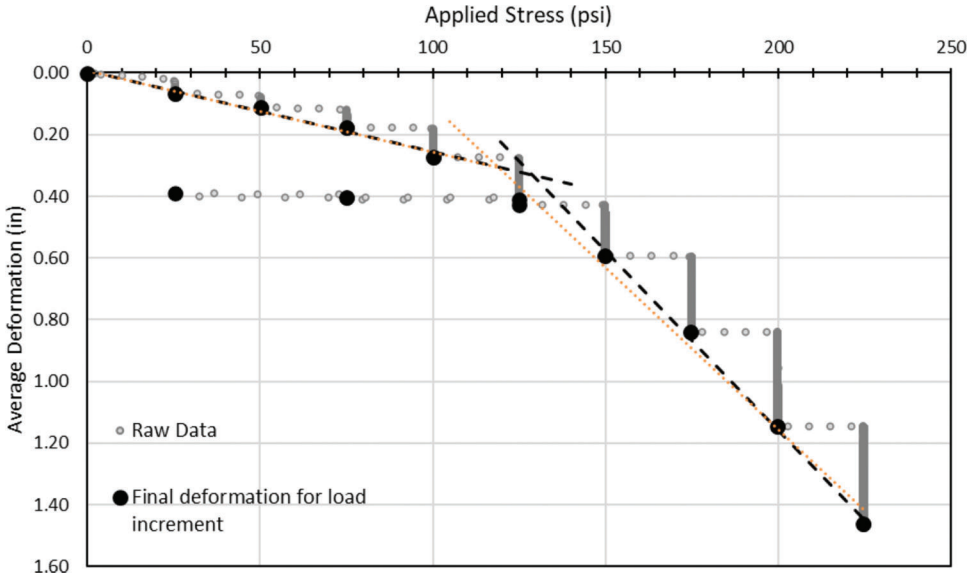

Figure 5.1 Determination of ultimate bearing capacity from 12-inch diameter static plate load test data.

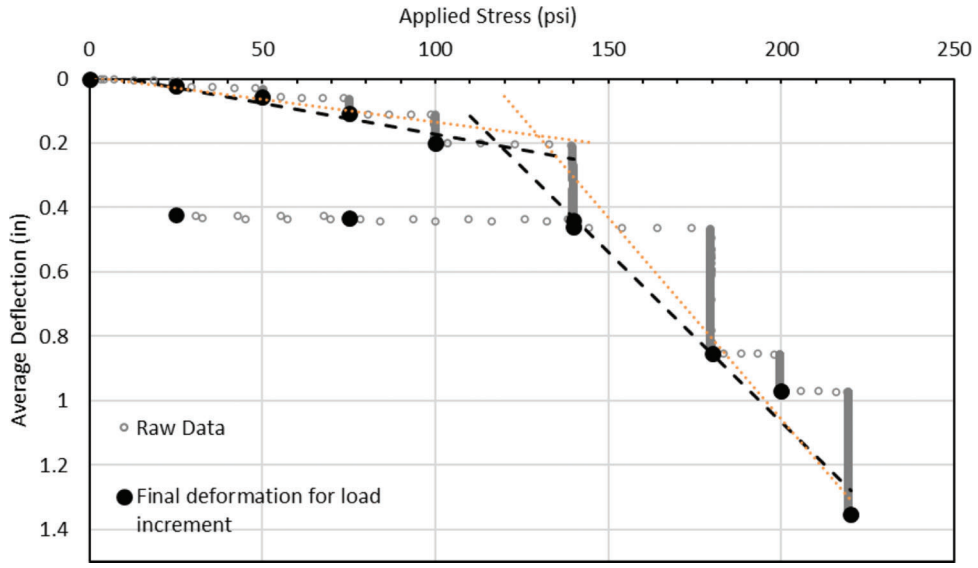

Figure 5.2 Determination of ultimate bearing capacity from 8-inch diameter static plate load test data.

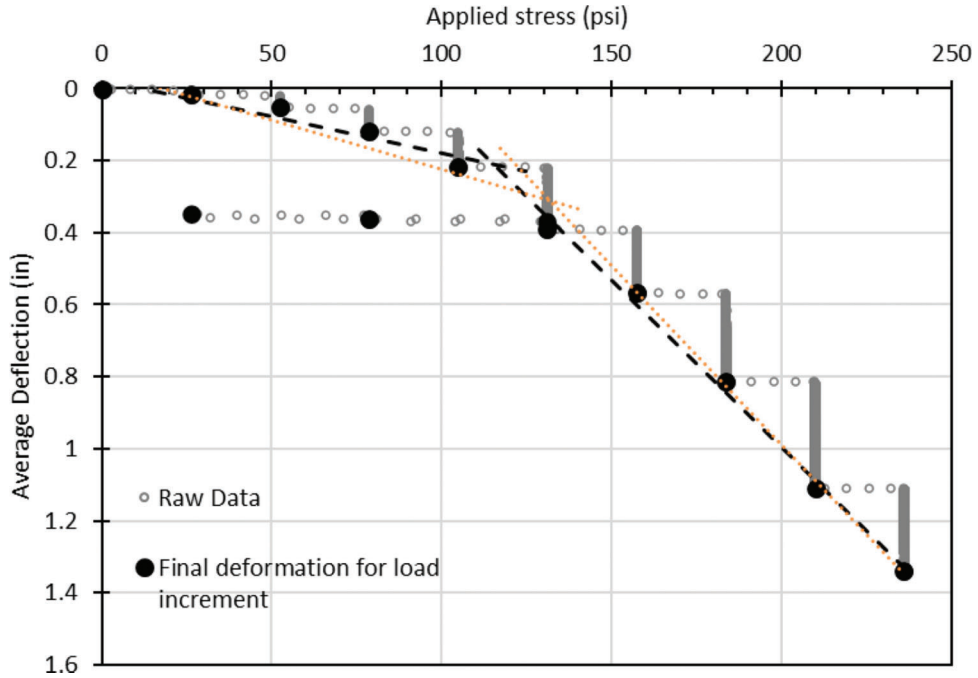

Figure 5.3 Determination of ultimate bearing capacity from 9.75-inch diameter static plate load test data.

TABLE 5.1
Values of the Angle of Internal Friction of Aggregate Back-Calculated from Experimental Bearing Capacity Data

Static Test Plate Diameter	Bearing Capacity (psi) (kPa)	Angle of Internal Friction, ϕ'
8 in	118 (813.6)–132 (910)	49.8°–50.3°
9.75 in	116 (800)–133 (917)	48.7°–49.4°
12 in	117 (806)–129 (889)	47.9°–48.3°

5.4c). The intermediate case (Figure 5.4b) corresponds to medium-dense material and shows local, instead of general failure, with no peak in the load-deformation curve.

The load-settlement curves of the static plate load tests performed for this study suggest an intermediate, medium-dense, type of failure, like Vesic's case (b) in

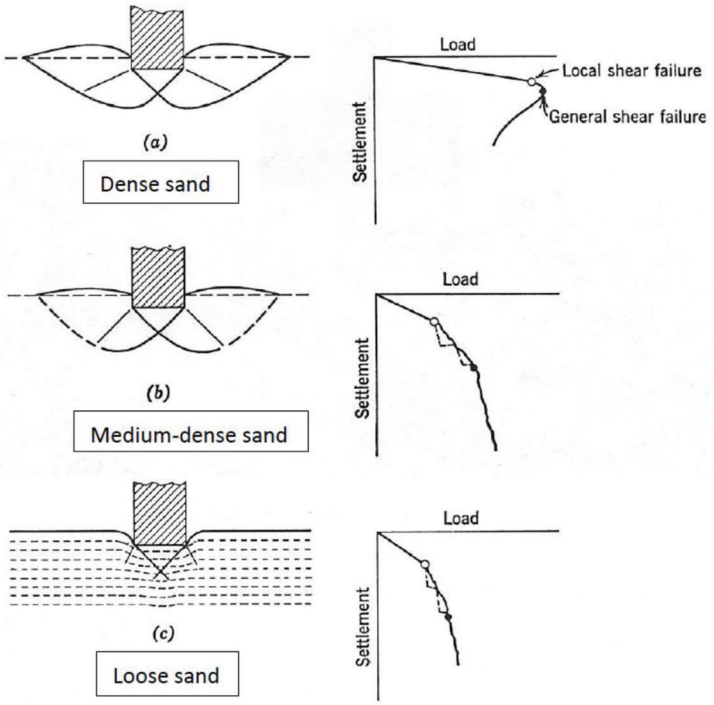

Figure 5.4 Bearing capacity failure mechanisms observed in sand (Vesic, 1963).

Figure 5.4. The method of compaction (light, hand-held roller compactor) and the value of the material unit weight of 134.8 pcf (21 kN/m^3) suggest the material was not very dense. However, since deformation gages were not installed outside of the plates for these tests and only the plate settlements were recorded, the absence of lateral heave cannot be confirmed by measurements. If indeed a medium-sense failure mechanism developed with local failure controlling the load-deformation curve, the ultimate shear strength may be higher than the values shown in the above analysis.

5.2.3 Derivation of Aggregate Angle of Internal Friction from Correlations with SPT

Standard Penetration Tests (SPT) were performed at three locations in the test pit as described in Section 3.4. The measured values were corrected to a 60% energy level. For the overburden correction, a soil unit weight of 134.8 pcf (21 kN/m^3) was used. Table 5.2 presents the data collected from all three SPT tests. Values of the angle of internal friction were derived from three different empirical correlations, as shown in Table 5.2. The resulting values are also within the range reported for aggregate materials tested at similarly low confining stresses as shown in the review of literature data by Getchell et al. (2020). The values of internal friction angle derived from the SPT test data are generally consistent with those back calculated from the bearing capacity plate load tests. Some discrepancy is observed when the Peck at al. (1974) SPT correlation is used, as this method gives lower values, in the 40° to 43° range. It is noted that the interpretation of SPTs in coarse-grained, frictional, soil depends on the overburden pressure at the depth of testing, and the correction applied to the blow count in order to account for this effect is itself empirical. At depths as small as only a few inches where the tests were performed, the correction for overburden pressure is extremely sensitive and should be considered as a source of uncertainty.

5.3 Analysis of RDL Tests

5.3.1 Effect of Site Conditions on Accumulation of Permanent Deformation with Loading Cycles

Granular materials manifest two types of deformation when subjected to repeated loading: resilient deformation and permanent deformation. The large number of load repetitions leads to a gradual accumulation of permanent deformation which can be detrimental for pavement structures. For this reason, analyzing the variation of permanent deformation with the number of cycles is critical for understanding the long-term performance of pavement systems (Lekarp & Dawson, 1998).

As detailed in Chapter 3, six extended cycle performance tests with randomly distributed load (RDL tests) were performed on the testing strips: three on the cement treated strip, three on the strip with the untreated subgrade. On each strip, one test was performed on the aggregate subbase (tests with 10,000 loading cycles), and a second (5,000 loading cycles) at the same location on the underlying subgrade. The third test (5,000 loading cycles) on each strip was

TABLE 5.2
SPT Data and Resulting Values of the Angle of Internal Friction of Aggregate

Location	First Mark	Second Mark	Third Mark	N60	N1(60)	Peck et al. (1974) Hatanakaa et al. (1996) ϕ'	Schmertmann (1975) ϕ'	ϕ'
1	8	9	10	19	47.3	40.1	50.8	47.0
2	17	11	10	21	52.3	41.3	52.4	48.0
3	22	12	11	23	57.3	42.5	53.9	48.9

Note:
Peck et al., (1974): $\phi' = 27.1 + 0.3(N_1)_{60} - 0.0054[(N_1)_{60}]^2$

Hatanaka Uchida (1996): $\phi' = \sqrt{20(N_1)_{60}} + 20$

Schmertmann (1975): $\phi' = \tan^{-1}\left[\frac{N_{60}}{12.2 + 20.3\left(\frac{\sigma'_0}{P_a}\right)}\right]^{0.34}$

TABLE 5.3
Overview of Conditions at RDL Testing Locations (Extracted from Table 3.3)

Location	LWD Deflection Data (mm) Subbase Large Plate	Subbase Small Plate	Subgrade Large Plate	Subbase Layer Thickness (in)	Subbase Dry Unit Weight (pcf)	Subbase Water Content (%)	Median Feature Index (mm)
CTO4	0.229	0.133	0.146	9.75	134.8	4.54	4.11
CTQ2	0.279	0.176	0.153	8.40	137.3	4.30	4.18
UNTI2	0.384	0.283	2.368	7.00	133.0	3.19	4.94
UNTQ3	0.375	0.399	1.412	6.85	131.7	3.21	5.24

performed on the aggregate subbase on the portion of the strip where a nonwoven geotextile fabric had been placed between subgrade and subbase. Table 3.5 summarizes the testing protocol followed in these tests. For easier reference, data on the layer characteristics at the testing locations already presented in Table 3.3 is reproduced in Table 5.3.

Curves of permanent deformation versus the number of loading cycles for the tests performed on the aggregate subbase at locations CTO4 and UNTI2 are shown in Figure 5.5a. From Table 5.3, at these two locations the values of the aggregate dry density were quite consistent. Figure 5.5a clearly highlights the significantly higher permanent deformation accumulated in the test conducted on the untreated strip (factor of 4.5–5 over the 10,000 cycles applied). The softer subgrade is responsible for the larger deformations accumulated in the test at UNTI2, as demonstrated by the fact that at this location (Figure 5.5c) the curves of permanent deformation versus number of loading cycles for the tests on subbase and subgrade essentially overlap. In contrast, in the case of the cement treated strip, the primary contribution to the permanent deformation is from the aggregate subbase, as can be seen by comparing the curves for the RDL tests on the subbase and subgrade at CTO4 (Figure 5.5b).

With regard to the other two tests performed on the aggregate subbase at locations CTQ2 and UNTQ3, any contribution from the geotextile separator layer is excluded, as the fabric was chosen to function as separator layer not as reinforcement, Moreover, upon exhumation of the fabric after completion of the plate load testing program, significant damage of the geotextile, in the form of bursts, perforations and abrasions, was observed (see pictures in Appendix D). The results for these tests are overall consistent with the data from the other locations. The RDL test on the subbase at location CTQ2 which had characteristics similar to those at location CTO4 (compare LWD results for both subbase and subgrade, and layer thickness, subbase dry unit weight, water content and median feature index data in from Table 5.3) yields a curve of permanent deformation versus number of loading cycles very close to that for the test at CTO4 (Figure 5.5b).

In the case of the two tests performed on the aggregate subbase on the untreated strip, the smaller values of the permanent strain accumulated in the test at UNTQ3 relative to UNTI2 (Figure 5.5c) are consistent with the smaller value (by a factor of 1.7) of the LWD deflection measured on the subgrade (Table 5.3). Again, this emphasizes that in the case of the untreated subgrade, it is the deformation of this layer that controls the accumulation of permanent deformation with loading cycles.

5.3.2 Applicability of Select Existing Models for Describing Development of Permanent Deformation with Loading Cycles Measured in RDL Tests

Several studies have investigated the behavior of unbound granular materials under repeated loading, leading to several models for describing the relationship between permanent deformation and number of loading cycles. Lekarp and Dawson (1998), Lekarp et al. (2000), and Chow et al. (2014) present a comprehensive review of these studies. Select models used below to fit the field data are shown in Table 5.3. Differences in the form of the equations of the models reflect variations in the granular materials, the type

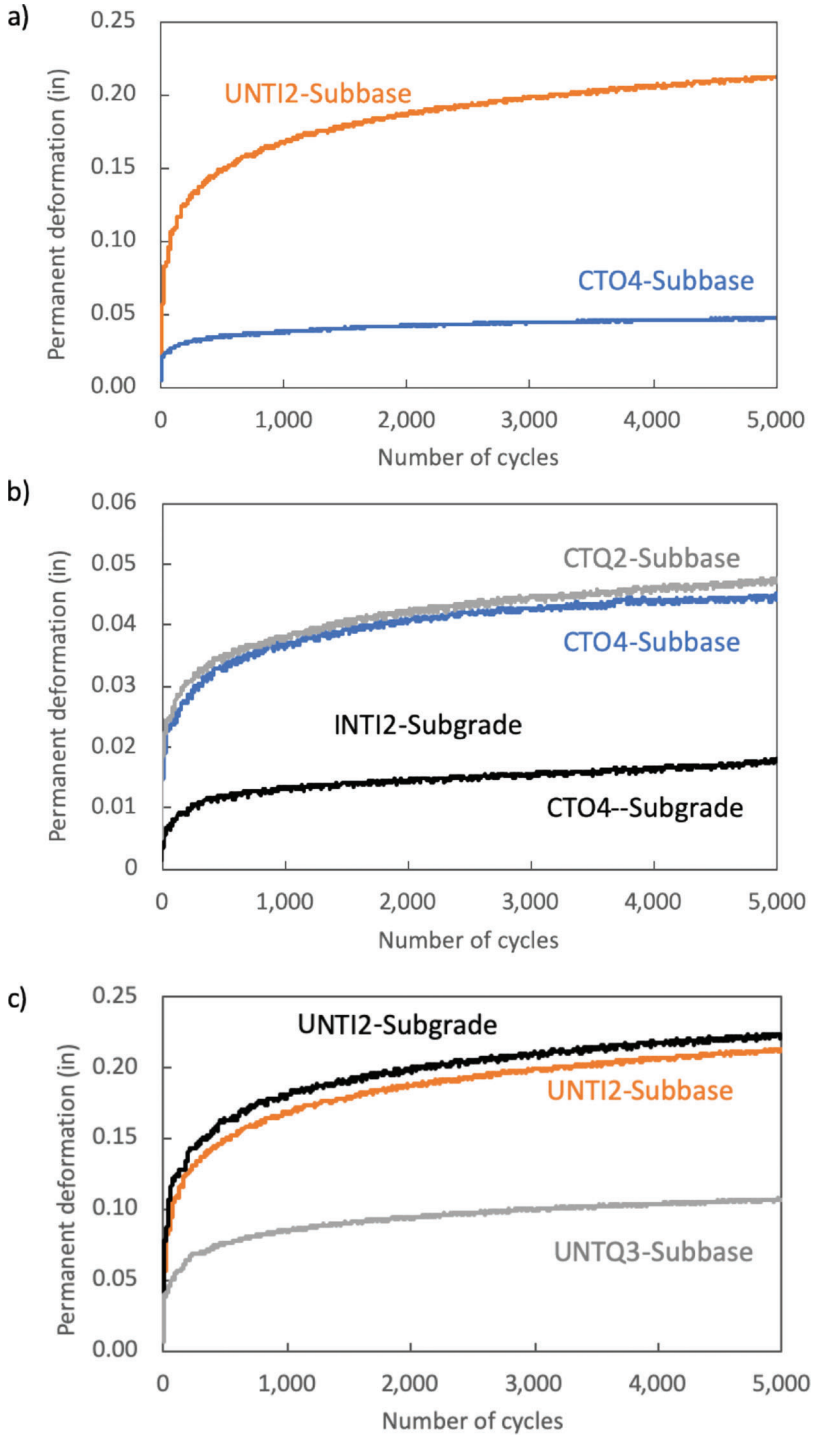

Figure 5.5 Accumulated permanent deformation versus number of loading cycles for (a) RDL tests performed on subbase at CTO4 and UNTI2, (b) RDL tests on a cement-treated strip, and (c) RDL tests on an untreated strip.

TABLE 5.4
Select Models for Correlating Permanent Deformation to Loading Cycles

Author	Model Equation	Source of Data	Material	Notes
Barksdale (1972)	$\delta_p = a + b \log(N)$ N = *number of cycles,* *a, b = fitting parameters*	Repeated load triaxial tests: 100,000 load cycles	Crushed stone (basecourse materials)	–
Monismith et al. (1975), Sweere (1990)	$\delta_p = aN^b$ N = *number of cycles,* *a, b = fitting parameters*	Triaxial tests: 1,000,000 load cycles	–	b falls in the range 0.1–0.2. a is dependent on stress state and strength of material.
El-Mitiny (1980), Khedr (1985)	$\frac{\delta_p}{N} = aN^{-b}$ N = *number of cycles,* *a, b = fitting parameters*	Variable confining pressure triaxial tests	Crushed limestone	Permanent strain rate inversely proportional to number of load cycles a, which represents rutting susceptibility, is highly dependent on stress state and M_r
Wolff & Visser (1994)	$\delta_p = (cN + a)(1 - e^{-bN})$ N = *number of cycles,* *a, b, c = fitting parameters*	Full-scale heavy vehicle simulator tests with several million loading cycles	Unbound aggregate base and subbase layers	Initial phase (1.2 mln cycles)– rapid development of permanent deformation 2nd phase (constant rate of increase of perm. def)
Ullitdz (1997)	$\delta_p = a\left(\left(\frac{\sigma_d}{p}\right)^b\right)N^c$ N = *number of cycles,* σ_d = *deviator stress,* *a, b, c = fitting parameters*	Discrete element method (DEM) simulations	–	Parameter an independent of applied stress

of test, the number of load repetitions, and the stress level in the tests based on which each model was developed. The model by Tseng and Lytton (1989) (Equation 2.5) that is used in the MEPDG software was not considered in the analysis of the field data. This is because of the uncertainty associated with the large number of parameters present in the model.

Note that, except for the model by Ullitdz (1997), the models shown in Table 5.4 relate permanent deformation only to the number of cycles applied, i.e., they do not consider the stress level effects. In addition to the model by Ullitdz (1997), other models consider this effect. However, their use requires knowledge of quantities (e.g., the length of stress path in the models by Lekarp and Dawson (1998) and by Gidel et al. (2001)) that cannot be quantified in a straightforward manner in the case of field plate load tests.

The permanent deformation data obtained from the six RDL tests discussed above were analyzed to establish the degree to which the models by Barksdale (1972), Monismith et al. (1975), El-Mitiny (1980), Wolff and Visser (1994) and Ullitdz (1997) can describe the measured increase in permanent deformation with loading cycles.

Table 5.5 and summarizes the results of this analysis performed using the *Curve Fitting Toolbox* in *Matlab.* It includes the values of the parameters derived for each model from the fitting process and the coefficient of determination (R^2) as a measure of the goodness of fit. Note that the Ullitdz (1997) model is a modified version of the Monismith et al. (1975) model with an extra term introduced to account for the magnitude of the deviator stress. As a result, when fitting the data using this model, the cyclic stress data are also included. Figure 5.6 compares the curves of measured and predicted permanent deformation versus number of cycles for each of the five models considered for the RDL test performed on the cement treated subgrade at location CTO4. For each model, two plots are presented: one that shows the two curves over the entire duration of the test (5,000 cycles for the test shown), the other for the first 500 cycles, representing the initial loading phase, where the rate of increase of the permanent deformation is very rapid. For the same tests plots of predicted versus measured permanent deformation are presented in Figure 5.7. Similar plots for the other five RDL tests are included in Appendix C. Table 5.6 summarizes the permanent strain values measured at the end of each test and compares them to the predictions from each model.

The following conclusions can be drawn with regard to the performance of the different models.

- Overall, all models capture the rapid accumulation of permanent strain that occurs during the first few hundred cycles, which is responsible for over half of the permanent deformation at the end of the test (5,000 cycles), and the subsequent slower rate of progression of the permanent deformation.
- The model by Wolff and Visser (1994) underperforms the other models, as reflected in the lower values of the

TABLE 5.5
Results of Fitting Analysis (Cells Highlighted in Yellow Identify Highest Value of the Coefficient of Determination)

Testing Location and No. of Cycles	Fitting Parameters	Barksdale (1972)	Monismith et al. (1975)	El-Mitiny (1980)	Wolff & Visser (1994)	Ullitdz (1997)
CTO4SB	a	0.0060	0.017	0.017	0.039	0.017
10K	b	0.010	0.112	0.888	0.007	-0.009
	c	–	–	–	9.51E-07	0.112
	R^2	0.9750	0.9482	0.9482	0.8254	0.9503
CTO4SG	a	-0.024	0.004	0.004	0.012	0.004
5K	b	0.005	0.175	0.826	0.010	-0.018
	c	–	–	–	1.17E-06	0.175
	R^2	0.9760	0.9806	0.9806	0.9579	0.9847
CTQ2SB	a	0.0036	0.015	0.015	0.035	0.015
5K	b	0.012	0.137	0.863	0.019	-0.009
	c	–	–	–	2.80E-06	0.137
	R^2	0.9894	0.9947	0.9947	0.8842	0.9963
UNTI2SB	a	0	0.057	0.057	0.171	0.058
10K	b	0.064	0.154	0.846	0.006	-0.004
	c	–	–	–	7.22E-06	0.154
	R^2	0.9959	0.9928	0.9928	0.9311	0.9931
UNTI2SG	a	-0.002	0.064	0.064	0.167	0.064
5K	b	0.060	0.148	0.852	0.012	-0.006
	c	–	–	–	1.29E-05	0.148
	R^2	0.9967	0.9837	0.9839	0.9145	0.9844
UNTQ3SB	a	-0.004	0.028	0.028	0.079	0.029
5K	b	0.030	0.157	0.843	0.010	-0.007
	c	–	–	–	6.43E-06	0.157
	R^2	0.9927	0.9903	0.9903	0.9163	0.9910

Note: The highest values of R^2 are indicated in red for each test.

TABLE 5.6
Comparison of the Measured and Predicted Values of the End of Test Accumulated Permanent Deformation

Testing Locationand No. of Cycles	End of Test Deformation[1]	Barksdale (1972)	Monismith et al. (1975)	El-Mitiny (1980)	Wolff & Visser (1994)	Ullitdz (1997)
CTO4SB	Measured value (in)			0.046		
10K	Difference (%)	1.9	2.6	2.6	3.6	5.2
CTO4SG	Measured value (in)			0.017		
5K	Difference (%)	-2.4	-0.2	-0.2	3.2	-1.8
CTQ2SB	Measured value (in)			0.048		
5K	Difference (%)	-1.4	-0.1	-0.1	3.3	3.8
UNTI2SB	Measured value (in)			0.234		
10K	Difference (%)	-0.5	0.9	0.9	3.9	1.7
UNTI2SG	Measured value (in)			0.222		
5K	Difference (%)	0.1	1.6	1.6	4.2	1.4
UNTQ3SB	Measured value (in)			0.16		
5K	Difference (%)	0.7	2.2	2.2	4.8	3.4

[1]Difference is calculated as (predicted-measured)/measured × 100.

coefficient of determination calculated for all tests. As indicated in Figure 5.6, it is the fit in the first few hundred cycles which is particularly poor. This might be expected as the model was derived based on tests with several million loading cycles.

- The model by Wolff and Visser (1994) also consistently overpredicts the end of test permanent deformation, by 3.2% to 4.8%.
- The remaining models show similar performance (R^2>0.975 in all cases), with the models by Barksdale (1972) and Ullitdz (1997) providing the best fit in four and two of the tests, respectively.
- For all tests, fitting the data using the model Ullitdz (1997) yields a very small value (-0.0044 to -0.018) of the parameter *b* (exponent of the term that accounts for the influence of the deviator stress). This implies that, at least for the range of deviator stresses used in this testing program, the magnitude of the deviator stresses plays a secondary role, and that the increase in permanent deformation is driven primarily by the number of cycles.

As a result, the other two parameters that appear in the Ullitdz (1997) model (*a* and *c*) effectively coincide with those calculated using the Monismith model (termed *a* and *b*), and the performance of these two models is virtually identical.

The results of the fitting analysis presented in Table 5.5 also support the observations in Section 5.3.1 on the effects of the site conditions on the permanent deformation behavior, specifically the following effects.

- The fitting parameters for the tests on the untreated strip all reflect higher accumulation of permanent deformation relative to the tests on the cement treated strip. Compare, for example, the values of parameter *b* in the Barksdale model that quantifies the rate of increase in permanent deformation with log(cycles) (0.005–0.01 for the tests at locations CTO4 and CTQ2 versus 0.03–0.06 for the tests at locations UNTI2 and UNTQ3) or the values of parameter *a* in the models by El-Mitiny (1980) which quantifies the rutting potential (0.004–0.02 for the tests at locations CTO4 and CTQ2 versus 0.03–0.06 for the tests at locations UNTI2 and UNTQ3).
- At location UNTI2, no significant difference is observed in the fitting parameters derived from the test on the subgrade and that on the subbase.

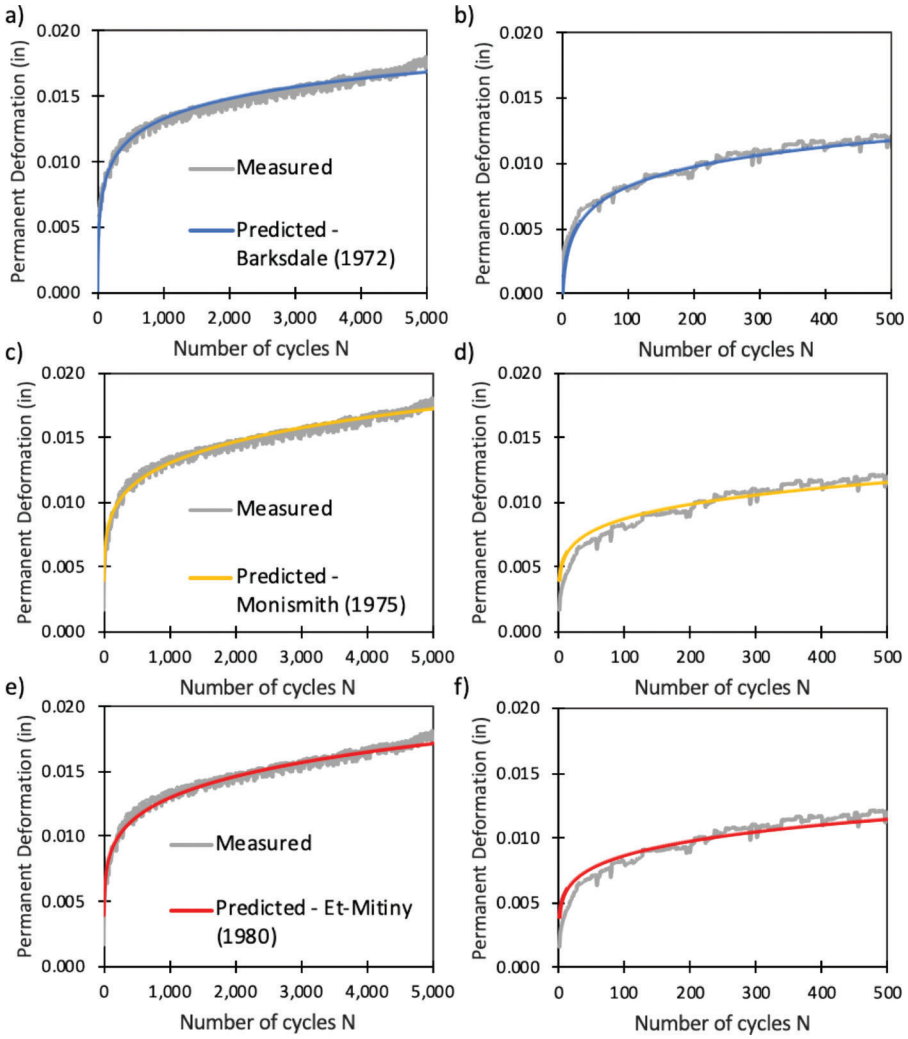

Figure 5.6 Continued to next page.

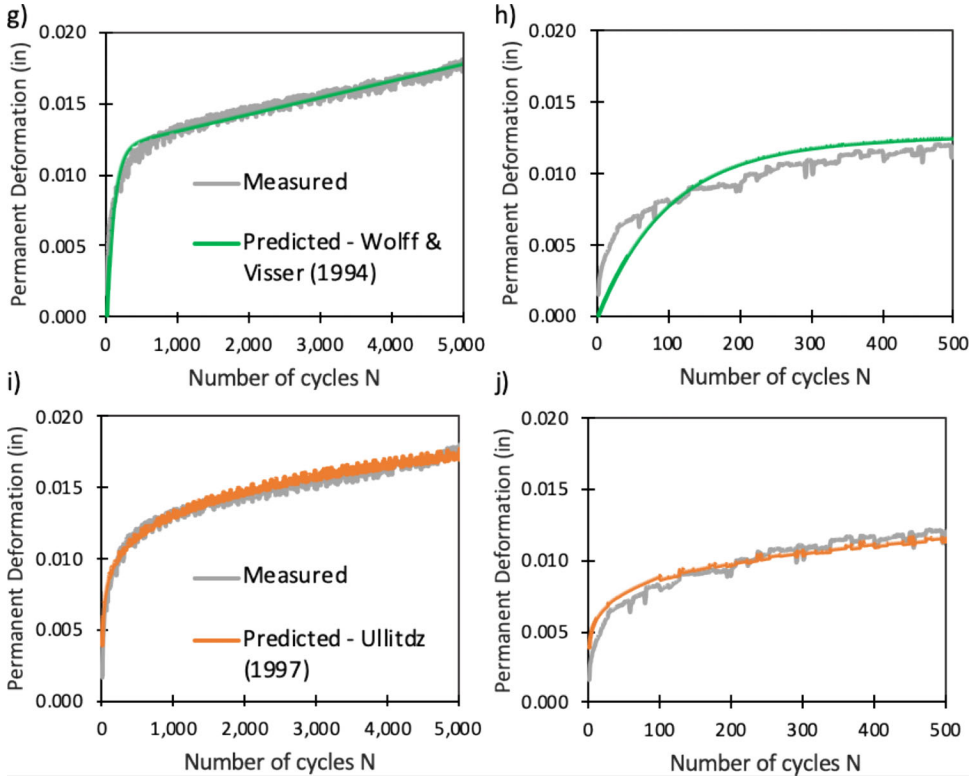

Figure 5.6 Comparison of predicted versus measured curves of permanent deformation versus number of loading cycles for test CTO4SG (5,000 cycles): (a–b) Barksdale (1972) model, (c–d) Monismith et al. (1975) model, (e–f) El-Mitiny (1980) model, (g–h) Wolff and Visser model (1994), and (i–j) Ullitdz model.

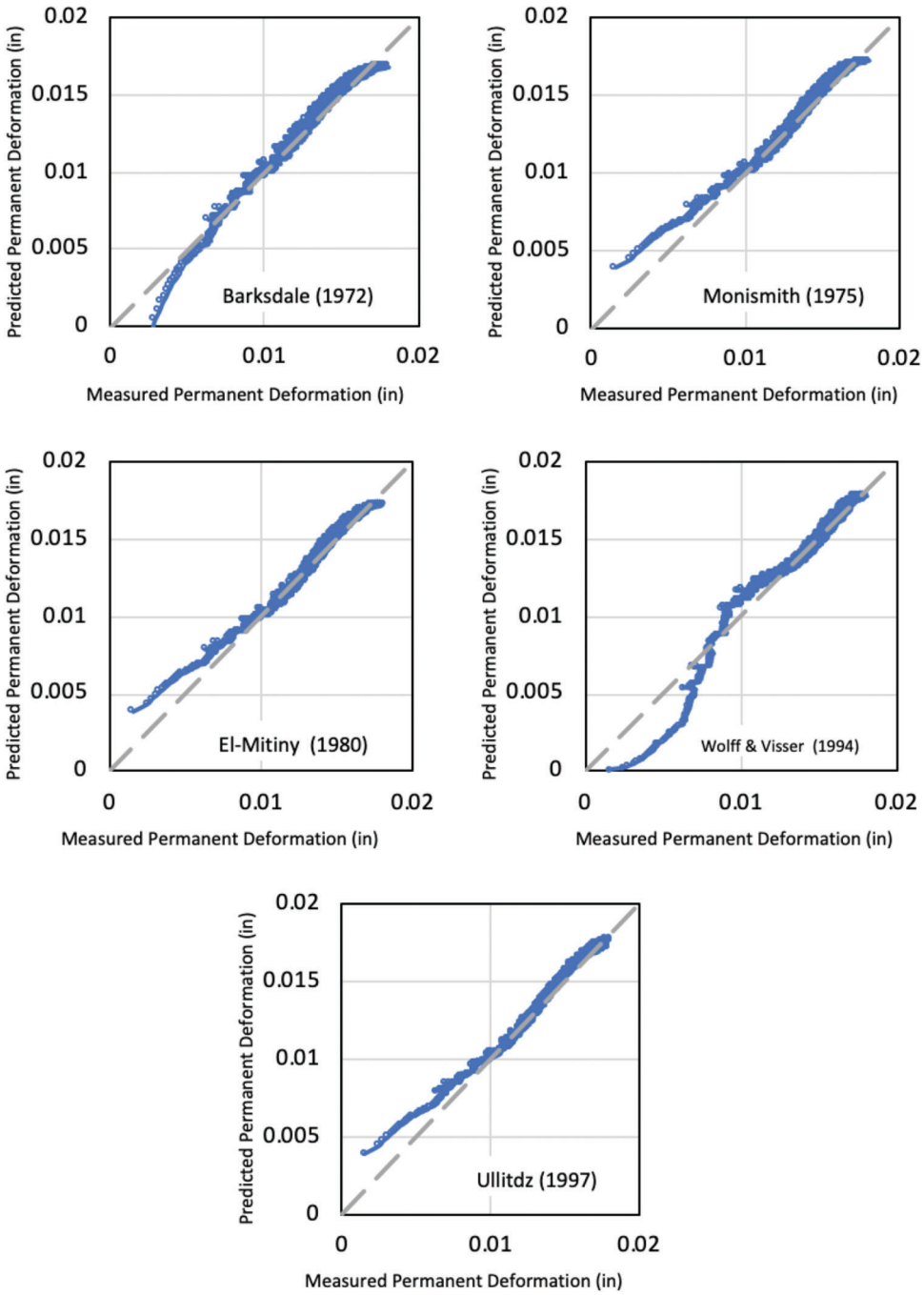

Figure 5.7 Comparison of predicted versus measured permanent deformation for test CTO4SG: (a) Barksdale (1972), (b) Monismith (1975), (c) El-Mitiny (1980), (d) Wolff & Visser model (1994), and (e) Ullitdz model.

6. CONCLUSIONS AND RECOMMENDATIONS

6.1 Overview of Work

The research presented in this report was aimed at advancing the understanding of the resilient and permanent deformation properties of pavement subgrade and subbase materials used in the state of Indiana and at exploring the use of automated plate load tests (APLT) for determining such properties.

The work performed included the following.

- A *review of the literature* pertaining to the interpretation of plate load tests and to the resilient modulus and the permanent deformation behavior of unbound aggregates. As the primary focus of this work was on the resilient modulus of aggregates with characteristics similar to those of Indiana #53, a database of M_r values for these materials was also assembled.
- A *parametric elastic finite element study* was conducted using the commercial software ABAQUS to investigate the factors affecting the interpretation of plate load test data. The model geometries used in the analyses were

chosen to represent both homogeneous as well as layered sections, with consideration of material input parameters (modulus and Poisson ratio), stiffness of the loading plate, and material anisotropy, as measured by the anisotropy modulus ratio ($n = E_h/E_v$, where E_v represents the vertical resilient modulus, M_r).

- *Analysis of field data* from automated plate load tests conducted as part of a previous research project on two testing strips consisting of a layer of Indiana #53 aggregate (average thickness across both strips = 7.1 in) compacted on top of either the untreated or the cement-treated subgrade. The testing program on the testing strips included two sets of tests: multistage resilient modulus (MR) tests with 1,550 cycles (500 conditioning cycles followed by 175 cycles at increasing applied cyclic stress) and extended cyclic performance tests with random distributed loading (RDL tests) (5,000 or 10,000 cycles at 10 different cyclic stress levels between 5 psi and 50 psi). In most cases, MR and RDL tests were performed first on the aggregate subbase using a 12-in diameter plate, and then on the underlying subgrade using an 18-in diameter plate. MR tests on the subbase included measurements of surface deflection at distances of 2r, 3r, and 4r away from the center of the plate. Two of the RDL tests were performed at strip locations where a nonwoven geotextile had been placed between subgrade and subbase. Additionally, three static load tests (with plates of diameter equal to 8, 9.75, and 12 in) were conducted to a maximum stress of 225 psi (1,551 kPa) on the #53 aggregate compacted in a 3.6 ft deep pit constructed in proximity to the two strips.

Analysis of the MR test data relied on elastic finite element analyses performed using ABAQUS and conventional approaches used for the interpretation of plate load tests on both homogenous and layered systems.

6.2 Conclusions

The discussion of the conclusions drawn from this research is organized to reflect findings related to the interpretation of the MR field plate load tests, the resilient and permanent deformation behavior of the materials tested, and the impact of the foundation layer.

6.2.1 Interpretation of MR Field Plate Load Tests

The primary conclusions drawn from analysis of the MR plate load tests conducted using (1) conventional approaches based on the use of the Boussinesq-based solution (Equation 4.3) for single layer systems, and of Equation 4.4 and Equation 4.5 for two-layer systems, and (2) elastic finite element (FE) analyses performed with the software ABAQUS are summarized below.

For tests conducted on a homogenous untreated subgrade layer:

- Use of the Boussinesq-based solution (Equation 4.3) with a constant shape factor ($\pi/2$ to represent loading of a cohesive soil by a rigid plate) leads to values of M_r (which identifies the vertical elastic modulus E_v) consistently lower than those derived from FE analyses conducted using the same hypotheses of homogeneity and isotropic behavior. For the two tests conducted at the S-BRITE site, the discrepancy increases with decreasing stress level, from ~20% at the highest applied cyclic stress (38 psi) to as much as a factor of 3 at the lowest applied cyclic stress (4 psi).
- The shape factor, which is conventionally assumed to be a constant value, is found, based on the elastic FE analyses, to decrease with increasing stress level, from a value close to 5 for the lowest cyclic stress applied (~4 psi) to a value of ~1.7–1.8 at the highest (~38 psi). This indicates that factors other than plate stiffness and stress distribution underneath the plate influence this parameter. Assumption of a constant a priori value of the shape factor does not appear justified.
- Consideration of material anisotropy (measured by the anisotropy modulus ratio, $n = E_h/E_v$, where E refers to the resilient modulus), impacts the moduli derived from the FE analyses, with M_r values increasing with increasing n.
- Estimates of M_r obtained from the FE analyses for the untreated soil decrease non-linearly with cyclic stress level, a trend that is consistent with literature data. This trend is not observed in the predictions obtained using the Boussinesq-based solution.

For tests conducted on a cement-treated subgrade layer:

- Use of the solution (Equation 4.3) based on Boussinesq leads to underestimate M_r of the cement treated layer relative to solutions from FE analyses which account for the presence of the softer underlying natural soil.

For tests performed on the compacted aggregate layer overlying the untreated or cement treated subgrade:

- Significant differences are observed between the values of $M_{rSubgrade}$ and $M_{rSubbase}$ back-calculated from FE analyses (in which the moduli are derived following an iterative procedure that minimizes differences between predicted and measured surface deflections) and those derived using current practice that relies on prediction of the subgrade modulus from off center deflection measurements and the Boussinesq-Odemark method (Equations 4.4 and 4.5). In general, the FE analyses yield higher values of $M_{rSubgrade}$ and lower values of $M_{rSubbase}$ and increasing deviation between the results from the two approaches is observed as the applied cyclic stress decreases.
- The assumed degree of anisotropy (as measured by the modulus anisotropy ratio, n, varied in this study between 0.5 and 2) of the aggregate subbase has a significant impact on the values of $M_{rSubgrade}$ and $M_{rSubbase}$ derived from the FE analyses, with both these moduli increasing with increasing n.
- The expression (see Equation 4.4 in Chapter 4) commonly used in practice and included in AASHTO (1993) for deriving M_r of the subgrade from surface elastic deflections measured away from the plate is found to yield inaccurate predictions, as verified through FE analyses. The method rests on two assumptions: the first one, that surface deflections at a distance from the plate are mainly due to deformation in the subgrade, is legitimate but the second one, that actual subgrade deformation can be calculated as equal to the deforma-

tion produced by a concentrated load applied directly on the subgrade, is conceptually inadequate.
- Values of M_r for the untreated subgrade back calculated using ABAQUS from off-center surface deflection measurements exceed those obtained from tests performed directly on the subgrade, which are considered more reliable.
- Values of $M_{rSubbase}$ derived from the tests performed on the untreated strip are significantly lower (in some cases by almost an order of magnitude) than those estimated for the same aggregate from the tests on the cement-treated strip. This is observed in both the results of the conventional approach and in the FE results. This discrepancy is in part due to overestimates of M_r of the untreated subgrade due to the use of off-center surface deflections (see above), as any error in estimating $M_{rSubgrade}$ will affect the modulus derived for the overlying subbase layer. Foundation conditions also play a role, as discussed in Section 6.2.3.

Overall, a number of factors and assumptions impact the interpretation of plate load tests, leading to significant uncertainty in the values of the resilient moduli of the tested layers derived from the test data. Compounded with their high cost, which necessarily limits the number of tests that can be performed in the field, this level of uncertainty indicates that plate load tests are not suitable for performing fundamental behavioral studies (e.g., to quantify the variation of M_r with stress level) or to derive M_r values of pavement materials for use in design.

6.2.2 Resilient and Permanent Deformation Behavior of the Materials Tested

The primary conclusions regarding the resilient behavior can be summarized as follows.

- Estimates of M_r of the #53 aggregate compacted on the cement treated subgrade vary in a very broad range, with values ranging between 15,000 psi (103 MPa) and 72,000 psi (496 MPa) depending on the testing location, the applied cyclic stress, the assumed modulus anisotropy ratio, and the approach used to derive M_r from the test data.
- Lower values of $M_{rSubbase}$ are derived for the aggregate layer compacted on the untreated subgrade. Again, these values vary in a wide range, from less than 3,000 psi to ~20,000 psi (~21–138 MPa), the testing location, the applied cyclic stress, the assumed modulus anisotropy ratio, and the approach used to derive M_r.
- No conclusion from the plate load testing program performed as part of this research project can be drawn regarding the stress level dependency of the resilient modulus of #53 aggregate. This aspect is better addressed through laboratory tests.
- The values of M_r of the cement treated subgrade derived from the plate load tests in this research are significantly higher than Level 3 values (12,500–15,000 psi (86–103 MPa)) included in current INDOT guidelines (N. Siddiki, personal communication, August 2023). They also exceed the values provided in the MEDPG Manual of Practice (AASHTO, 2020) (15,000–16,500 psi (103–114 MPa), assuming the A-4 classification for the cement-treated S-BRITE soil).

With regard to the permanent deformation behavior.

- The models by Barksdale (1972), Monismith et al. (1975), El-Mitiny (1980) and Ullitdz (1997) all provide a satisfactory description of the accumulated permanent deformation behavior under repeated loading of the subbase and subgrade (untreated and cement treated) layers tested in this work, at least for the cyclic stresses, and the number of loading cycles (<10,000) applied in the tests.
- For the majority of the tests the accumulated permanent deformation behavior under repeated loading is best modeled using a logarithmic growth model.
- The fitting parameters derived for these models capture the impact of the foundation layer discussed in Section 6.2.3.

Finally, based on the three static plate load tests on the #53 aggregate compacted in the testing pit, values of the angle of internal friction in the 48°–50° range may be used for estimating the stability of #53 aggregate subbases to construction loading, provided that similar levels of density are achieved. This range is consistent with values reported in the literature for similar materials.

6.2.3 Impact of Foundation Layer

The following significant differences are observed in the results of the MR and RDL tests performed on the two strips, reflecting the impact of the foundation layer.

- As stated above, there is a significant discrepancy in the values of M_r of the #53 subbase layer derived from the MR tests performed on the two strips, which can only in part be ascribed to the approaches used to derive the moduli (see above). The data suggest that differences in the foundation layer also play a role, with a stiffer underlying layer promoting more effective compaction as evident also from the nuclear density data. In addition, differences in the subbase-subgrade interface conditions between the two strips may contribute to different degrees of compaction-induced modulus anisotropy. This aspect requires additional research.
- The permanent deformation behavior of the two-layer system is determined by foundation layer, with significantly higher permanent deformations accumulated in the tests on the untreated strip (factor as large as 4.5–5 over the duration of the test) compared to the tests on the cement treated strip.
- The permanent deformations measured in the RDL test on the untreated strip appear primarily because of deformations within the subgrade, with negligible contribution from the aggregate layer. In contrast, the subbase layer appears responsible for the larger fraction (60%–70%) of the accumulated permanent deformation measured in the test on the cement treated strip. These values are to be considered indicative as they are based only on two tests. Moreover, as the RDL test on the subgrade was performed immediately below the subbase testing location, it is unclear to what degree the results are influenced by the loading history associated with the RDL test performed earlier on the overlying subbase.
- In general, the results of the tests performed on the cement-treated strip display less spatial variability than

those obtained on the untreated strip (e.g., see LWD data in Table 3.1 as well as APLT test results). This suggests that cement treatment contributes to more homogeneity in both the subgrade and the overlying compacted aggregate.

Finally, an additional objective of the current study was to quantify the effect of the geotextile used as separator between subgrade and subbase on permanent deformations. The results of the RDL tests performed at location where the geotextile had been placed, indicate that the geotextile used, a nonwoven fabric (GEOTEX® 601 manufactured by Propex) did not provide any mechanical contribution. This geotextile meets the Class 2 survivability requirements based on Holtz et al. (2008) (see also Getchell et al., 2020) and qualifies as Type 2A geotextile for "underdrains, subsurface drains, and filtration applications" per INDOT standard specification 918.02(b) (INDOT, 2024). The lack of mechanical contribution was expected as the geotextile was chosen to provide filtration and separation functions. Observations on samples of the fabric exhumed from the RDL test locations show evidence of significant damage (tearing, bursting, abrasion) caused by compaction of the aggregate and/or the repeated loading during the RDL tests and indicate that the filtration and separation functions were likely also compromised.

6.3 Recommendations

Based on the work performed, the following recommendations for implementation are provided.

Plate Load Tests Versus Laboratory Tests

- Given the assumptions that impact the interpretation of plate load tests, including APLTs, laboratory tests, in which boundary conditions are clearly defined, and specimen density can be carefully controlled, are deemed more appropriate for investigating fundamental aspects of material behavior, including resilient and permanent deformation behavior.

Interpretation of Plate Load Tests

- Use of the Boussinesq-based solution with a constant shape factor is not recommended for interpreting MR plate load tests on untreated subgrade, as this approach is expected to underestimate the subgrade's resilient modulus, and yield values of M_r that do not reflect actual soil behavior. Instead, elastic finite element analyses such as those presented in this study are preferred, when possible, accounting for material anisotropy.
- Use of the solution based on Boussinesq is not recommended for interpreting MR plate load tests on cement-treated subgrade, as the assumption of homogeneity cannot be considered valid. A more reliable estimate of M_r of the cement treated subgrade may be obtained through FE analyses, assuming a realistic value of the layer modulus ratio, R, that reflects the presence of the underlying untreated soil.
- For plate load tests on two-layer (subbase over subgrade) systems, M_r of the bottom subgrade layer should not be derived from off-center surface deflections. Tests performed directly on the subgrade should be used to obtain more reliable estimates of $M_{rSubgrade}$.
- Once a reliable estimate of the subgrade M_r is obtained, finite element analyses should be considered the preferred method for deriving M_r of the overlying aggregate subbase layer, when possible, accounting for material anisotropy.

Plate Load Testing Protocols

- When performing plate load tests on both subbase and subgrade, the position of the plate should be sufficiently offset in the two tests so as to ensure that the results of the tests performed on the subgrade layer are not impacted by the loading history produced by the test previously performed on the overlying layer.
- While their use for back-calculating the modulus of the underlying layer is discouraged, off-center measurements of surface deflections should be included in all plate load tests whenever possible. In this study, these measurements were performed only in the MR tests on the aggregate subbase. They would have proven useful also in the case of the MR tests on the subgrade to establish whether analysis of test results required consideration of the presence of the untreated natural soil below the cement treated subgrade. For the same reason they would have aided the interpretation of the RDL tests performed on the subbase layers. The additional measurement points could also help assess the anisotropy ratio of the subbase using numerical optimization in the FEM model. Finally, they would have provided the means to confirm the mechanism of failure in the static plate load tests.

Selection of Parameters for Use in Design

- Given the above documented uncertainty in deriving M_r values for the #53 aggregate subbase from plate load test results, no recommendations can be made regarding minimum values for use in pavement design for this material.
- Under conditions similar to those encountered at the S-BRITE soil (A-6 (CL) natural soil, slurry cement stabilization with 4% cement—see Section 3.2), 25,000 psi (172 MPa) represents a conservative estimate for the resilient modulus of the cement modified soil, i.e., type IBC subgrade treatment.
- Based on the static plate load tests conducted in this work, values of the angle of internal friction in the 48°–50° range may be used for estimating the stability of medium-dense #53 aggregate subbases.

Construction Procedures

- Under conditions similar to those encountered at the S-BRITE site (see Section 3.2) cement treatment of the subgrade is recommended as it provides, as expected, better performance in terms of increased resilient modulus, reduced permanent deformation and less variable conditions (see data in Table 3.1). Moreover, the results from the S-BRITE site also suggest that the presence of the stiffer cement treated layer promotes more effective compaction of the overlying aggregate.
- Given the significant damage produced by the compaction process and/or the repeated loads applied in the RDL tests on the Class 1 geotextile (Geotex® 601

manufactured by Propex) used at the S-BRITE site, a higher-class product is recommended for use between subgrade and #53 aggregate to provide separation and filtration functions.

The study also highlighted areas where additional research is warranted. In particular, it is suggested that future efforts be directed towards the following.

- Further investigating the impact of the foundation layer on the compaction of #53 aggregate. This research is warranted given the differences in the values of dry density and resilient modulus derived from the two strips tested in this project.
- Quantifying the degree of anisotropy generated when compacting coarse aggregates such as #53, and, in particular, examining to what degree n evolves with increasing number of cycles and accumulated permanent deformation, and to what degree differences in the subbase-subgrade interface conditions contribute to different degrees of compaction-induced modulus anisotropy. It is suggested that this type of fundamental investigation, which is motivated by the significant impact that the modulus anisotropy ratio has on settlements produced under loaded areas, would be best pursued through laboratory tests.
- Exploring what other factors in addition to plate stiffness and stress distribution under the plate affect the shape factor.
- Comparing the results of the APLT testing program to the falling weight deflectometer (FWD) and light weight deflectometer (LWD) test data was also collected at the S-BRITE site.
- Comparing the results of the APLT testing program to M_r values collected in the laboratory for the Indiana #53 aggregate and the natural and cement treated S-BRITE soil as part of separate investigations.
- Interpreting the S-BRITE APLT data using models developed for the analysis of triaxial tests once the full data for individual cycles are made available, to explore additional avenues for predicting the evolution of permanent deformation due to cyclic loading.

REFERENCES

AASHTO. (1993). *AASHTO guide for design of pavement structures*. American Association of State Highway and Transportation Officials.

AASHTO. (2020). *Mechanistic-empirical pavement design guide: A manual of practice* (3rd ed.). American Association of State Highway and Transportation Officials.

AASHTO. (2021a). *Standard method of test for determining the resilient modulus of soils and aggregate materials* (AASHTO T307-99). American Association of State Highway and Transportation Officials.

AASHTO. (2021b). *Standard method of test for nonrepetitive static plate load test of soils and flexible pavement components for use in evaluation and design of airport and highway pavements* (AASHTO T222-81). American Association of State Highway and Transportation Officials.

AASHTO. (2021c). *Standard method of test for repetitive static plate load tests of soils and flexible pavement components for use in evaluation and design of airport and highway pavements* (AASHTO T221-90). American Association of State Highway and Transportation Officials.

Abu-Farsakh, M. Y., Alshibli, K., Nazzal, M. D., & Seyman, E. (2004). *Assessment of in-situ test technology for construction control of base courses and embankments* (Report No. FHWA/LA. 04/389). Louisiana Transportation Research Center.

Adu-Osei, A., Little, D. N., & Lytton, R. L. (2001). *Structural characteristics of unbound aggregate bases to meet AASHTO 2002 design requirements: Interim report* (Texas Transportation Institute Report No. ICAR/502-1). Aggregates Foundation for Technology Research & Education.

Allen, J. J., & Thompson, M. R. (1974). Resilient response of granular materials subjected to time-dependent lateral stresses. *Transportation Research Record*, *510*, 1–13.

Andrei, D., Witczak, M. W., Schwartz, C. W., & Uzan, J. (2004). Harmonized resilient modulus test method for unbound pavement materials. *Transportation Research Record*, *1874*(1), 29–37.

Arnold, A., Laue, J., Espinosa, T., & Springman, S. M. (2010). Centrifuge modelling of the behaviour of flexible raft foundations on clay and sand. In *Physical Modelling in Geotechnics, Two Volume Set* (pp. 705–710). CRC Press.

Ashtiani, R. S., & Little, D. N. (2009, August 31). *Methodology for designing aggregate mixtures for base courses* (Texas Transportation Institute Report No. ICAR/508). International Center for Aggregates Research (ICAR). https://repositories.lib.utexas.edu/bitstream/handle/2152/35379/508.pdf?sequence=2&isAllowed=y

ASTM. (2011). *Standard test method for standard penetration test (SPT) and split-barrel sampling of soils* (ASTM D1586-11). American Standards for Testing and Methods International.

ASTM. (2017). *Standard test methods for in-place density and water content of soil and soil-aggregate by nuclear methods (shallow depth)* (ASTM D6938-17a). American Standards for Testing and Methods International.

ASTM. (2020). *Standard test method for measuring deflections with a light weight deflectometer (LWD)* (ASTM E2583-07). American Standards for Testing and Methods International.

ASTM. (2021a). *Standard test method for nonrepetitive static plate tests of soils and flexible pavement components for use in evaluation and design of airport and highway pavements* (ASTM D1196/D1196M). American Standards for Testing and Methods International.

ASTM. (2021b). *Standard test method for repetitive static plate tests of soils and flexible pavement components for use in evaluation and design of airport and highway pavements* (ASTM D1195/D1195M-21). American Standards for Testing and Methods International.

Barden, L. (1963). Stresses and displacements in a cross-anisotropic soil. *Géotechnique*, *13*(3), 198–210.

Barksdale, R. D. (1972, September 11–15). Laboratory evaluation of rutting in base course materials. In *Proceedings of the Third International Conference on the Structural Design of Asphalt Pavements*, *1*, 161–174.

Bellotti, R., Jamiolkowski, M., Lo Presti, D. C. F., & O'neill, D. A. (1996). Anisotropy of small strain stiffness in Ticino sand. *Géotechnique*, *46*(1), 115–131.

Boussinesq, J. (1885). *Application des potentiels à l'étude de l'équilibre et du mouvement des solides élastiques: principalement au calcul des déformations et des pressions que produisent, dans ces solides, des efforts quelconques exercés sur une petite partie de leur surface ou de leur intérieur: mémoire suivi de notes étendues sur divers points de physique, mathematique et d'analyse* (Vol. 4). Gauthier-Villars.

Bourdeau, P. L. (1986). *Analyse probaliste des tassements d'un massif de sol granulaire* [Doctoral dissertation, Swiss Federal Institute of Technology].

Bowles, J. E. (1996). *Foundation analysis and design* (5th ed.). The McGraw-Hill Companies.

Brown, P. T. (1969). Numerical analyses of uniformly loaded circular rafts on elastic layers of finite depth. *Géotechnique*, *19*(2), 301–306.

Brown, S. F., & Hyde, A. F. L. (1975). Significance of cyclic confining stress in repeated-load triaxial testing of granular material. *Transportation Research Record*, *537*, 49–58.

Burmister, D. M. (1945). The general theory of stresses and displacements in layered systems. I. *Journal of Applied Physics*, *16*(2), 89–94. https://doi.org/10.1063/1.1707558

Casagrande, A., & Carrillo, N. (1944, April). Shear failure of anisotropic soils. *Contributions to Soil Mechanics 1941–1953* (pp. 122–135). Boston Society of Civil Engineers.

Chow, L. C., Mishra, D., & Tutumluer, E. (2014). *Aggregate base course material testing and rutting model development* (Report No. FHWA/NC/2013-18). North Carolina Department of Transportation.

Clough, R. W., & Rashid, Y. (1965, June 4). Finite element analysis of axi-symmetric solids. *Journal of the Engineering Mechanics Division*, *91*(1), 71–86.

Coffman, B. S., Kraft, D. C., & Tamayo, J. (1964, February). A comparison of calculated and measured deflections for the AASHO test road. In *Associated Asphalt Paving Technology Proceedings*, *33*, 54–91.

Dunlap, W. S. (1963). *A report on a mathematical model describing the deformation characteristics of granular materials* (Research project 2-8-62-27). Texas Transportation Institute of Texas A&M University.

El-Mitiny, M. R. (1980). *Material characterization for studying flexible pavement behavior in fatigue and permanent deformation* (Doctoral dissertation, Ohio State University).

Garg, S. K. (2004). *Soil mechanics and foundation engineering* (5th ed.). Khanna Publishers.

Garzon-Sabogal, L. E., Bourdeau, P. L., & Santagata, M. (2024). Grain portraits: Quantifying heterogeneity of aggregate layers through image analysis. In *Geo–Congress 2024* (pp. 329–339).

Getchell, A., Garzon Sabogal, L., Bourdeau, P. L., & Santagata, M. (2020). *Investigation of design alternatives for the subbase of concrete pavements* (Joint Transportation Research Program Publication No. FHWA/IN/JTRP-2020/03). West Lafayette, IN: Purdue University. https://doi.org/10.5703/1288284317114

Gidel, G., Hornych, P., Chauvin, J. J., Breysse, D., & Denis, A. (2001). A new approach for investigating the permanent deformation behaviour of unbound granular material using the repeated loading triaxial apparatus. *Bulletin des Laboratoire des Ponts et Chausées*, (233), 5–21.

Gu, C., Ye, X., Cao, Z., Cai, Y., Wang, J., & Zhang, T. (2020, December). Resilient behavior of coarse granular materials in three dimensional anisotropic stress state. *Engineering Geology*, *279*, 105848.

Gupta, S., Ranaivoson, A., Edil, T., Benson, C., & Sawangsuriya, A. (2007). *Pavement design using unsaturated soil technology* (Report No. Mn/DOT 2007-11). Minnesota Department of Transportation.

Hajj, E. Y., Thavathurairaja, J., Stolte, S., Sebaaly, P. E., Piratheepan, M., & Motamed, R. (2018, June). *Resilient modulus prediction models of unbound materials for Nevada* (Report No. WRSC-UNR-20180626). Western Regional Superpave Center.

Hanna, T. H. (1965, May). Discussion: The elastic properties of a dense glacial till deposit. *Canadian Geotechnical Journal*, *2*(2), 129–131.

Hatanaka, M., & Uchida, A. (1996). Empirical correlation between penetration resistance and internal friction angle of sandy soils. *Soils and Foundation*, *36*(4), 1–9.

Haynes, J. H., & Yoder, E. J. (1963). Effect of repeated loading on gravel and crushed stone base course materials used in the AASHO road test (Publication No. FHWA/IN/JHRP-63/04). *Highway Research Record*, *39*, 82–96.

Heydinger, A. G., Xie, Q., Randolph, B. W., & Gupta, J. D. (1996). Analysis of resilient modulus of dense- and open-graded aggregates. *Transportation Research Record*, *1547*(1), 1–6. https://doi.org/10.1177/0361198196154700101

Hicher, P. Y., & Chang, C. S. (2006). Anisotropic nonlinear elastic model for particulate materials. *Journal Geotechnic Geoenvironmental Engineering*, *132*(8), 1052–1061.

Hicks, R. G. (1970). *Factors influencing the resilient properties of granular materials* [Doctoral dissertation, University of California at Berkeley].

Hick, R. G., & Monismith, C. L. (1971). Factors influencing the resilient response of granular materials. *Highway Research Record*, *345*, 15–31.

Hoffman, M. S. (2004). Load-deformation behavior of fly-ash and bottom-ash capping and fill layers based on FWD deflection measurements. *Pavements Unbound; Proceedings of the 6th International Symposium on Pavements Unbound* (pp. 277–290).

Holtz, R. D., Christopher, B. R., & Berg, R. R. (2008, August). *Geosynthetic design & construction guidelines: Reference manual* (Publication No. FHWA NHI-07-092). Federal Highway Administration.

Hopkins, T. C., Beckham, T. L., & Sun, C. (2007). *Resilient modulus of compacted crushed stone aggregate bases* (Report No. KTC-05-27/SPR-229-01-1F). University of Kentucky Transportation Center. https://uknowledge.uky.edu/cgi/viewcontent.cgi?article=1284&context=ktc_researchreports

Horak, E., Hefer, A., & Maina, J. (2015). Modified structural number determined from falling weight deflectometer deflection bowl parameters and its proposed use in a benchmark methodology. *Journal of Traffic and Transportation Engineering*, *3*, 215–226.

Horikoshi, K., & Randolph, M. F. (1997). On the definition of raft—soil stiffness ratio for rectangular rafts. *Géotechnique*, *47*(5), 1055–1061.

Hossain, Z., Zaman, M., & Doiron, C. (2015). Regression modeling of resilient modulus of unbound aggregates. *Journal of Marine Science and Technology*, *23*(3), 388–398. https://doi.org/10.6119/JMST-014-0416-6

Huang, Y. H. (2004). *Pavement analysis and design* (2 ed.) (pp. 401–409). Pearson Prentice Hall.

Hveem, F. N. (1955). Pavement deflections and fatigue failures. *Highway Research Board Bulletin*, *114*, 43–87.

Hveem, F. N., & Carmany, R. M. (1949). The factors underlying the rational design of pavements. *Highway Research Board Proceedings*, *28*, 101–136.

INDOT. (2022, February 22). Design procedures for soil modification or stabilization. *Indiana Department of Transportation, Geotechnical Engineering Division*. https://www.in.gov/indot/engineering/files/Design_Procedures_for_Soil_Modification_or_Stabilization.pdf

INDOT. (2024). *Indiana Department of Transportation standard specifications 2024*. Indiana Department of Transportation. https://www.in.gov/dot/div/contracts/standards/book/sep23/2024%20Standard%20Specifications.pdf.

Ingios. (2021). *In situ resilient modulus characterization of cement treated subgrade research test section* [Unpublished manuscript]. Purdue University.

Jackson, K. D. (2015). *Laboratory resilient modulus measurements of aggregate base materials in Utah* (Master's thesis, Brigham Young University). BYU ScholarsArchive. https://scholarsarchive.byu.edu/etd/5721

Jiang, G.-L., Tatsuoka, F., Flora, A., & Koseki, J. (1997). Inherent and stress-state-induced anisotropy in very small strain stiffness of a sandy gravel. *Géotechnique*, *47*(3), 509–521.

Johnson, T. C., Berg, R. L., & Dimillio, A. (1986). Frost action predictive techniques: An overview of research results. *Transport Research Record*, *1089*, 147–161.

Kalcheff, I. V., & Hicks, R. G. (1973). A test procedure for determining the resilient properties of granular materials. *Journal of Testing and Evaluation*, *1*(6), 472–479.

Kamal, M. A., Dawson, A. R., Farouki, O. T., Hughes, D. A. B., & Sha'at, A. A. (1993). Field and laboratory evaluation of the mechanical behavior of unbound granular materials in pavements. *Transportation Research Record*, *1406*, 88–97.

Khedr, S. (1985). Deformation characteristics of granular base course in flexible pavement. *Transportation Research Record*, *1043*, 131–138. Transportation Research Board.

Kolisoja, P. (1997). *Resilient deformation characteristics of granular materials* (pp. 188–201). Tampere University of Technology.

Koning, H. L. (1957). Stress distribution in a homogeneous, anisotropic, elastic semi-infinite solid. In *4th International Conference on Soil Mechanics and Foundation Engineering* (pp. 335–338). International Society for Soil Mechanics and Geotechnical Engineering.

Kuhn, M. R., Sun, W. C., & Wang, Q. (2015). Stress-induced anisotropy in granular materials: fabric, stiffness, and permeability. *Acta Geotechnica*, *10*(4), 399–419.

Lashine, A. K. F. (1971). *Some aspects of the characteristics of Keuper marl under repeated loading* (Doctoral dissertation, University of Nottingham).

Lekarp, F., & Dawson, A. (1998). Modelling permanent deformation behaviour of unbound granular materials. *Construction and Building Materials*, *12*(1), 9–18.

Lekarp, F., Isacsson, U., & Dawson, A. (2000). State of the art. I: Resilient response of unbound aggregates. *Journal of Transportation Engineering*, *126*(1), 66–75.

Lemmen, H. E., Jacobsz, S. W., & Kearsley, E. P. (2017). The influence of foundation stiffness on the behaviour of surface strip foundations on sand. *Journal of the South African Institution of Civil Engineering*, *59*(2), 19–27.

Lenke, L. R., McKeen, R. G., & Grush, M. P. (2003). Laboratory evaluation of GeoGauge for compaction control. *Transportation Research Record*, *1849*(1), 20–30.

Li, L., Liu, J., Zhang, X., & Saboundjian, S. (2011). Resilient modulus characterization of Alaska granular base materials. *Transportation Research Record*, *2232*(1), 44–54.

Love, A. E. H. (1892). *A treatise on the mathematical theory of elasticity*. Cambridge University Press.

Maher, A., Bennert, T., Gucunski, N., & Papp, W. J., Jr. (2000). *Resilient modulus properties of New Jersey subgrade soils* (Report No. FHWA-NJ-2000-01). New Jersey Department of Transportation.

Malla, R. B., & Joshi, S. (2006). *Establish subgrade support values for typical soils in New England* (Report No. NETCR 57). University of Connecticut.

Mayne, P. W., & Poulos, H. G. (1999). Approximate displacement influence factors for elastic shallow foundations. *Journal of Geotechnical and Geoenvironmental Engineering*, *125*(6), 453–460.

Modoni, G., Flora, A., Mancuso, C., Viggiani, C., & Tatsuoka, F. (2000). Evaluation of gravel stiffness by pulse wave transmission tests. *Geotechnical Testing Journal*, *23*(4), 506–521.

Monismith, C. L., Ogawa, N., & Freeme, C. R. (1975). Permanent deformation characteristics of subgrade soils due to repeated loading. *Transportation Research Record*, *537*, 1–17.

Monismith, C. L., Seed, H. B., Mitry, F. G., & Chan, C. K. (1967). Prediction of pavement deflections from laboratory tests. *Proceeding of the 2nd International Conference Structural Design of Asphalt Pavements* (pp. 109–140).

Moossazadeh, J. M., & Witczak, W. (1981). Prediction of subgrade moduli for soil that exhibits nonlinear behaviour, *Transportation Research Record*. National Research Council.

Morgan, J. R. (1966). The response of granular materials to repeated loading. *Australian Road Research Board Proceedings*, *3*(Part 2), 1178–1192.

NCHRP. (2004a). *Laboratory determination of resilient modulus for flexible pavement design* (NCHRP Project 1-28A). National Cooperative Highway Research Program.

NCHRP. (2004b). *Summary of the 2000, 2001, and 2002 AASHTO guide for the design of new and rehabilitated pavement structures* (NCHRP Project 1-37A). National Cooperative Highway Research Program.

Nazarian, S., Pezo, R., Melarkode, S., & Picornell, M. (1996). Testing methodology for resilient modulus of base materials. *Transportation Research Record*, *1547*(1), 46–52.

Nazzal, M. D. (2007). *Laboratory characterization and numerical modeling of geogrid reinforced bases in flexible pavements* (Doctoral dissertation, Louisiana State University).

Nguyen, B. T., & Mohajerani, A. (2016). Resilient modulus of fine-grained soil and a simple testing and calculation method for determining an average resilient modulus value for pavement design. *Transportation Geotechnics*, *7*(3), 59–70. https://doi.org/10.1016/j.trgeo.2016.05.001

Ni, B., Hopkins, T. C., Sun, L., & Beckham, T. L. (2002). Modelling the resilient modulus of soils. *Proceeding of 6th international conference on the bearing capacity of roads, railways and airfield*, *2*, 1131–1142. A.A. Balkema Publishers.

Ooi, P. S. K., Sandefur, K. G., & Archilla, A. R. (2006). *Correlation of resilient modulus of fine-grained soils with common soil parameters for use in design of flexible pavements* (Report No. HWY-L-2000-06). Hawaii Department of Transportation

Pan, T., Tutumluer, E., & Anochie-Boateng, J. (2006). Aggregate morphology affecting resilient behavior of unbound granular materials. *Transportation Research Record*, *1952*(1), 12–20. https://doi.org/10.1177/0361198106195200102

Papagiannakis, A. T., & Masad, E. A. (2008). *Pavement design and materials*. John Wiley & Sons.

Patriot Engineering and Environmental, Inc. (2014). *Report of geotechnical engineering investigation* (Project No. 6-14-0015). Purdue University.

Peck, R. B., Hanson, W. E., & Thornburn, T. H. (1974). *Foundation engineering* (2nd ed.). Wiley.

Petersen, L., & Peterson, R. (2006). *Intelligent compaction and in-situ testing at Mn/DOT TH53* (Report No. MN/RC-2006-13). CNA Consulting Engineers.

Pezo, R. F. (1993). A general method of reporting resilient modulus tests of soils–A pavement engineer's point of view. *Proceedings of the 72nd Annual Meeting of the Transportation Research Board*. Transportation Research Board.

Pickering, D. J. (1970). Anisotropic elastic parameters for soil. *Géotechnique*, *20*(3), 271–276.

Poulos, H. G. (1968). Analysis of the settlement of pile groups. *Géotechnique*, *18*(4), 449–471.

Puppala, A. J. (2008). *Estimating stiffness of subgrade and unbound materials for pavement design* (NCHRP Synthesis 382). Transportation Research Board.

Puppala, A. J., Hoyos, L. R., & Potturi, A. K. (2011). Resilient moduli response of moderately cement-treated reclaimed asphalt pavement aggregates. *Journal of Materials in Civil Engineering*, *23*(7), 990–998.

Raad, L., & Figueroa, J. L. (1980). Load response of transportation support systems. *Transportation Engineering Journal*, *16*(TE1), 111–128.

Rada, G., & Witczak, M. W. (1981). Comprehensive evaluation of laboratory resilient moduli results for granular material. *Transportation Research Record*, *810*, 23–33.

Robinson, R. G. (1974). *Measurement of the elastic properties of granular materials using a resonance method* (TRRL Supplementary Report No. 111UC). Transport and Road Research Laboratory.

Schmertmann, J. H. (1975). Measurement of in-situ shear strength. *Proceedings of ASCE Spec. Conference on In-Situ Measurement of Soil Properties*, *2*, 57–138.

Seed, H., & Fead, J. (1960). Apparatus for repeated load tests soils (STP44306S). *Papers on Soils 1959 Meetings* (pp. 78–87). ASTM International.

Seed, H. B., & Chan, C. K. (1964, August). *Appendix C, pulsating loading tests on samples of clay and silt from Anchorage, Alaska*. Report on Anchorage Area Soil Studies to US Army Engineer District.

Seed, H. B., Mitry, F. G., Monismith, C. L., & Chan, C. K. (1967). Factors influencing the resilient deformations of untreated aggregate base in two-layer pavements subjected to repeated loading. *Highway Research Record*, *190*, 19–57.

Seyhan, U., & Tutumluer, E. (2002). Anisotropic modular ratios as unbound aggregate performance indicators. *Journal of Materials in Civil Engineering*, *14*(5), 409–416.

Shaw, P. (1980). *Stress-strain relationships for granular materials under repeated loading* (Doctoral dissertation, University of Nottingham). https://www.nottingham.ac.uk/research/groups/ntec/documents/theses/shawphdthesis.pdf

Siekmeier, J. A., Young, D., & Beberg, D. (2000). Comparison of the dynamic cone penetrometer with other tests during subgrade and granular base characterization in Minnesota. *ASTM Special Technical Publication*, *1375*, 175–188.

Sowers, G. B., & Sowers, G. F. (1970). *Introductory soil mechanics and foundations* (3rd ed.). The Macmillan Company.

Sweere, G. T. H. (1990). *Unbound granular bases for roads* (Doctoral dissertation, University of Delft). http://resolver.tudelft.nl/uuid:1cc1c86a-7a2d-4bdc-8903-c665594f11eb

Tam, W. A., & Brown, S. F. (1988). Use of the falling weight deflectometer for in situ evaluation of granular materials in pavements. *Proceeding of the 14th ARRB Conference*, *14*(5), 155–163.

Tanimoto, K., & Nishi, M. (1970). On resilience characteristics of some soils under repeated loading. *Soils and Foundations*, *10*(1), 75–92.

Thom, N. (2014). *Principles of pavement engineering* (2nd ed.). ICE Publishing.

Thompson, M. R., & Robnett, Q. L. (1979). Resilient properties of subgrade soils. *Transportation Engineering Journal*, *105*(TE1), 71–89.

Timoshenko, S. P., & Goodier, J. N. (1970). *Theory of elasticity*. McGraw-Hill.

Titi, H. H., & Matar, M. G. (2018). Estimating resilient modulus of base aggregates for mechanistic-empirical pavement design and performance evaluation. *Transportation Geotechnics*, *17*, 141–153.

Trollope, D. H., Lee, I. K., & Morris, J. (1962). Stresses and deformation in two layer pavement structures under slow repeated loading. *Proceedings of the First Conference of the Australian Road Research Board*, *1*(2), 693–721.

Tseng, K.-H., & Lytton, R. L. (1989). Prediction of permanent deformation in flexible pavement materials. *Implication of Aggregates in the Design, Construction, and Performance of Flexible Pavements (ASTM SPT 1016)* (pp. 154–172). American Society for Testing and Materials.

Tutumluer, E. (2009). State of the art: Anisotropic characterization of unbound aggregate layers in flexible pavements. In *Pavements and Materials: Modeling, Testing, and Performance* (pp. 1–16). https://doi.org/10.1061/41008(334)1

Tutumluer, E., Kazmee, H., & Mishra, D. (2016). *Development of anisotropic material models test plan*. Report for U.S. Army Engineer Research and Development Center.

Tutumluer, E., & Thompson, M. R. (1997). Anisotropic modeling of granular bases in flexible pavements. *Transportation Research Record*, *1577*(1), 18–26.

Ullidtz, P. (1987). Pavement analysis. *Developments in Civil Engineering*, *19*. The Technical University of Denmark.

Ullidtz, P. (1997). Modeling of granular materials using the discrete element method. *Proceedings of the 8th International Conference on Asphalt Pavements* (pp. 757–769).

Uthus, L. (2007). *Deformation properties of unbound granular aggregates* (Doctoral dissertation, Norwegian University of Science and Technology). NTNU Open. http://hdl.handle.net/11250/231354

Uzan, J. (1985). Characterization of granular material. *Transportation Research Record*, *1022*(1), 52–59.

Vennapusa, P. K., White, D. J., Wayne, M. H., Kwon, J., Galindo, A., & García, L. (2020). In situ performance verification of geogrid-stabilized aggregate layer: Route-39 El Carbón–Bonito Oriental, Honduras case study. *International Journal of Pavement Engineering*, *21*(1), 100–111. https://doi.org/10.1080/10298436.2018.1442576

Vesic, A. B. (1963). Bearing capacity of deep foundations in sand. *Highway Research Record*, *39*, 112–153.

Wang, H., & Al-Qadi, I. L. (2013). Importance of nonlinear anisotropic modeling of granular base for predicting maximum viscoelastic pavement responses under moving vehicular loading. *Journal of Engineering Mechanics*, *139*(1), 29–38.

White, D. J., & Vennapusa, P. K. R. (2017). In situ resilient modulus for geogrid-stabilized aggregate layer: A case study using automated plate load testing. *Transportation Geotechnics*, *11*, 120–132. https://doi.org/10.1016/j.trgeo.2017.06.001

White, D., Vennapusa, P., & Cackler, T. (2019). *In situ modulus measurement using automated plate load testing for statewide mechanistic-empirical design calibration* (Report No. ST-003). Ingios Geotechnics.

White, D. J., Vennapusa, P., & FitzPartrick, B. (2016). *Automated plate load testing report: Love's travel stop,*

Sadieville, KY - Medium-duty pavement test section (Report No. 2016-032). BreakThrough Technologies.

Wichtmann, T., Hernández, M. A. N., & Triantafyllidis, T. (2015). On the influence of a non-cohesive fines content on small strain stiffness, modulus degradation and damping of quartz sand. *Soil Dynamics and Earthquake Engineering*, *69*(2), 103–114. https://doi.org/10.1016/j.soildyn.2014.10.017

Wilson, E. L. (1963). *Finite element analysis of two dimensional structures* (Doctoral dissertation, University of California).

Witczak, M. (2003). *NCHRP 1-28A: Harmonized test method for laboratory determination of resilient modulus for flexible pavement design*. Transportation Research Board.

Witczak, M. W., & Uzan, J. (1988). *The universal airport pavement design system, Report I of V: Granular material characterization*. University of Maryland.

Wolff, H., & Visser, A. T. (1994). Incorporating elasto-plasticity in granular layer pavement design. *Proceedings of the Institution of Civil Engineers Transport*, *105*(4), 259–272. https://doi.org/10.1680/itran.1994.27137

Yau, A., & Von Quintus, H. L. (2002). *Study of LTPP laboratory resilient modulus test data and response characteristics: Final report* (Report No. FHWA-RD-02-051). Turner-Fairbank Highway Research Center.

Yoder, E. J., & Witczak, M. W. (1975). *Principles of pavement design* (2nd ed.) (pp. 504–519). John Wiley & Sons.

Zeghal, M. (2004). Discrete-element method investigation of the resilient behavior of granular materials. *Journal of Transportation Engineering*, *130*(4), 503–509.

APPENDICES

Appendix A. Database of M_r Values for Aggregates

Appendix B. M_r Values Derived From Conventional Analysis of M_r Tests

Appendix C. Supplementary Plots From Analysis of RDL Test Data

Appendix D. Images of Exhumed Geotextile Fabric

APPENDIX A. DATABASE OF M_r VALUES FOR AGGREGATES

Table A.1 Characteristics of aggregates contained in database

Material	Symbol	Reference	Gradation			Compaction Characteristics			Shape		Specimen Characteristics	
			Passing No 200 (%)	D_{50} (mm)	C_u	Max Dry Density (pcf)	Optimum Water Content (%)	Method of Compaction			Dry Density (pcf)	Water content w(%)
Bloomington	IN1		7.8	9.0	107.5					-	-	-
DGA (As received)	KY1	Hopkins et. al., (2007)	8.0	4.0	51.7	142.5	6.8	Standard Proctor Test: Method D		-	136.6	5.7
DGA Upper Gradation	KY2		13.0			142.3	6.9			-	118.9	2.3
DGA Center Gradation	KY3		9.0	5.5	92.9	144.1	6.9			-	128.5	4.9
DGA Lower Gradation	KY4		4.0			113.6		Shake Table		-	117.4	1.9
CSB Upper Gradation	KY5		8.0	3.5	66.7	144.8	6.2	Standard Proctor Test : Method D		-	139.5	4.8
CSB Center Gradation	KY6		4.0	9.5	142.2	144.1	5.5			-	140.9	3.5
CSB Lower Gradation	KY7		0.0	9.5		114.2		Shake Table		-	113.7	2.6
Arrowood Quarry	NC1	Chow et. al., (2013)	8.0	6.0	90.0	153.5	4.2	Standard Proctor Test: Method A	Angularity Index (1.0 - in)	431	159.5	3.9
Belgrade Quarry	NC2					131.3	7.4			560	131.6	7.4
Fountain Quarry	NC3					141.2	6.1			430	132.6	6.6
Harrison Franklin Quarry	NC4					151.5	4.7			428	150.6	5.5
Goldhill	NC5					142.2	6.4			463	141.9	6.8
Hendersonville	NC6					139.3	5.5			496	139.3	6
Jamestown	NC7					141.6	5.8			412	143.0	5
Lemon Spring	NC8					140.9	5.5			418	142.0	5
Moncure	NC9					148.2	5.2			432	147.9	6
Nash County	NC10					142.3	5.7			394	144.1	6.2
N. Wilkesboro	NC11					142.5	5			389	142.2	5.4
Princeton	NC12					141.3	5.1			458	140.7	5.7
Raleigh	NC13					139.6	6.1			401	138.2	7.3
Rockingham	NC14					141.4	6.1			524	142.1	5.9
Rocky Point	NC15					134.7	5.9			526	134.7	5.9
Rougemont	NC16					144.1	5.9			481	143.5	6.8
Limestone at Merridian	OK1	Hossain et. al., (2015)	6.3	9.0	72.2	Min = 133	Min = 4.6			-		
Limestone at RS	OK2		5.6	6.0	52.8	Mean = 142.5	Mean = 5.5			-		
Sandstone	OK3		4.8	10.4	123.1	Max = 149	Max = 7.5			-		
Norththern Region 6% FC	AK11	Li et. al., (2010)	6.0	5.0	34.4	146.1	5.2	Impact Compaction Method with Soil Compactor	Percent Fracture Face (%)	100	146.7	5.2
	AK12										145.16	6.3
Norththern Region 8% FC	AK21		8.0	4.8	53.3	148.0	5.3				148.01	5.3
	AK22										147.16	5.8
Norththern Region 10% FC	AK31		10.0	4.7	88.0	148.1	5.3				148.1	5.3
	AK32										146.89	5.8
Southeast Region 6% FC	AK41		6.0	5.0	34.4	156.2	5.3			91.7	156.18	5.3
	AK42										155.41	6.2
Southeast Region 8% FC	AK51		8.0	4.8	53.3	156.7	5.4				156.47	5.4
	AK52										156.67	5.8
Southeast Region 10% FC	AK61		10.0	4.7	88.0	156.8	5.5				156.83	5.2
	AK62										156.83	5.8
Central Region 6% FC	AK71		6.0	5.0	34.4	147.9	6			84.5	146.83	5.2
	AK72										147.86	6
Central Region 8% FC	AK81		8.0	4.8	53.3	150.2	5.4				150.1	5.2
	AK82										149.98	5.8
Central Region 10% FC	AK91		10.0	4.7	88.0	151.0	5.3				151.06	5.2
	AK92										150.45	5.9
Utah Mcguire	UT1	Jackson (2015)	5.0	5.2	28.9	139.3	5.8			-	-	-
Utah Trenton	UT2		4.8	4.9	27.6	142.2	5.6			-	-	-
Utah Vernal	UT3		10.2	4.7	92.9	140.3	6.6			-	-	-
Utah Elsinore	UT4		5.0	4.6	30.5	137.4	6.3			-	-	-
Utah Nielson	UT5		5.4	3.5	18.5	138.6	5.4			-	-	-
Dis 1 3546	NV1	Hajj et. al., (2018)	8.8	6.5	56.3	144.7	5	Standard Proctor Test: Method A,D		-	-	-
Dis 1 3583	NV2		8.7	5.2	78.8	147.3	5.6			-	-	-
Dis 1 3597	NV3		8.3	5.8	62.5	143.0	3.9			-	-	-
Dis 1 3605	NV4		7.7	8.0	64.7	147.5	5			-	-	-
Dis 1 3613	NV5		5.3	7.2	75.0	135.8	6.7			-	-	-
Dis 1 3607	NV6		10.0	6.5	140.0	141.6	3.5			-	-	-
District 2 B	NV7		7.8	5.3	43.3	138.2	8			-	-	-
District 3 B	NV8		7.5	3.2	31.3	129.7	8.4			-	-	-
District 4 B	NV9		9.7	3.2	68.0	132.8	7.2			-	-	-

Table A.2 Universal model parameters for aggregates in database

	Universal Model			
Material	k1	k2	k3	R2
KY1	1411.06	1.0497	-0.2511	0.996
KY2	4368.61	0.8176	-0.2634	0.983
KY3	972.63	1.0331	-0.1509	0.985
KY4	1154.47	1.1275	-0.2891	0.99
KY5	1960	0.8685	-0.1735	0.988
KY6	3170.99	0.7939	-0.1354	0.996
KY7	2198.65	0.903	-0.1874	0.991
NC1	1160	0.611	-0.027	0.999
NC2	857	0.611	0.105	0.997
NC3	511	0.74	0.018	0.999
NC4	723	0.672	0.068	0.996
NC5	814	0.652	-0.004	998
NC6	716	0.711	-0.011	1
NC7	875	0.597	0.031	0.997
NC8	829	0.589	0.053	0.997
NC9	886	0.542	0.091	0.997
NC10	610	1.018	-0.027	0.99
NC11	968	0.609	-0.024	0.999
NC12	725	0.681	0.062	0.993
NC13	952	0.713	-0.093	0.997
NC14	941	0.703	0.029	0.994
NC15	941	0.703	0.029	0.994
NC16	571	0.73	-0.006	0.994
UT11	810.3	1.583	-4.072	0.957
UT12	735.5	1.653	-4.018	0.96
UT13	669.8	1.177	-2.617	0.9
UT21	836.5	1.254	-3.415	0.9286
UT22	956.4	1.491	-3.766	0.9544
UT23	1086	1.604	-4.382	0.96
UT32	792.7	1.309	-3.04	0.9381
UT33	942.3	1.219	-3.067	0.9138
UT41	933.2	1.463	-3.943	0.9445
UT42	586.1	1.371	-3.071	0.956
UT43	558	1.243	-2.803	0.9226
UT44	744.5	1.718	-4.551	0.9343
UT51	1617	1.528	-4.606	0.9498
UT52	683.3	1.342	-3.165	0.9449
UT53	748.6	1.258	-3.024	0.94
UT54	1380	1.461	-4.514	0.9436
NV1	1506	0.4504	0.1313	0.9859
NV2	1273	0.4218	0.0973	0.98
NV3	1329	0.4366	0.2632	0.992
NV4	1116	0.5474	0.0293	0.9956
NV5	1227	0.4475	0.137	0.99
NV6	1054	0.5853	0.1009	0.9939
NV8	705.2	0.5247	0.1193	0.9859
NV9	610.7	0.5127	0.2559	0.9823
AK11	1206	0.2235	0.08576	0.87
AK12	1480	0.8645	-0.4055	0.96
AK22	1388	0.8343	-0.456	0.98
AK31	2335	0.5437	-0.6479	0.81
AK32	1735	0.8976	-0.4526	0.9868
AK41	852.9	0.3013	0.8386	0.85
AK42	1079	0.5925	0.1877	0.9433
AK51	1601	0.3928	-0.0674	0.8591
AK52	942.1	0.3888	0.7158	0.92
AK61	1261	0.3419	0.3145	0.9345
AK62	881.5	0.365	0.723	0.9275
AK71	1414	0.2536	-0.3032	0.9279
AK72	520.2	0.1381		0.86

APPENDIX B. M_r VALUES DERIVED FROM CONVENTIONAL ANALYSIS OF M_R TESTS

Table B.1 Subgrade Mr values predicted from plate load tests on subgrade using Equation 4.3, as reported by the company that performed the tests (Ingios, 2021)

CTC5SG		
σ cyclic [psi]	Mr [psi]	Mr [MPa]
13.5 (conditioning)	58,451	403
4.5	40,384	278
8.3	45,851	316
13.4	58,329	402
19.6	68,235	470
29.2	70,651	487
39.8	70,105	483

CTJ2SG		
σ cyclic [psi]	Mr [psi]	Mr [MPa]
14.7 (conditioning)	52,186	360
4.5	32,611	225
8.4	43,363	299
14.6	56,782	391
19.1	59,647	411
29.5	60,788	419
39.8	67,630	466

CTM2SG		
σ cyclic [psi]	Mr [psi]	Mr [MPa]
14.4 (conditioning)	37930	262
4.4	26,662	184
8.3	29,881	206
14.5	40,008	276
18.2	39,710	274
29.0	41,858	289
38.7	40,646	280

UNTJ6SG		
σ cyclic [psi]	Mr [psi]	Mr [MPa]
13.0 (conditioning)	4,231	29
4.1	3,681	25
8.1	3,685	25
13.0	4,240	29
18.1	4,135	29
28.0	3,731	26
38.2	3,760	26

UNTL3SG		
σ cyclic [psi]	Mr [psi]	Mr [MPa]
13.8 (conditioning)	11,936	82
4.4	10,913	75
8.3	10,911	75
13.8	11,965	82
18.4	11,650	80
28.5	11,174	77
38.9	10,727	74

Table B.2 Subbase and subgrade Mr values predicted using Equations 4.4 & 4.5 from plate load tests on subbase with multi radii measurements, as reported by the company that performed the tests (Ingios, 2021)

CTC5SB					
σ cyclic [psi]	Mr–Subbase [psi]	Mr - Subgrade [psi]	Mr–Subbase [MPa]	Mr - Subgrade [MPa]	R
13.5 (conditioning)					
4.2	30,349	82,244	209	567	0.37
9.4	48,215	85,205	332	587	0.57
13.5	61,606	83,484	425	576	0.74
18.6	67,129	88,081	463	607	0.76
29.7	72,931	84,266	503	581	0.87
40.5	73,736	94,371	508	651	0.78

CTJ2SB					
σ cyclic [psi]	Mr–Subbase [psi]	Mr - Subgrade [psi]	Mr–Subbase [MPa]	Mr - Subgrade [MPa]	R
13.5 (conditioning)					
4.2	43,228	90,381	298	623	0.48
8.5	32,692	82,211	225	567	0.40
13.5	43,354	69,349	299	478	0.63
18.8	44,496	87,007	307	600	0.51
29.9	61,996	71,888	427	496	0.86
39.0	60,782	84,097	419	580	0.72

CTM2SB					
σ cyclic [psi]	Mr–Subbase [psi]	Mr - Subgrade [psi]	Mr–Subbase [MPa]	Mr - Subgrade [MPa]	R
13.6 (conditioning)					
4.2	88,519	30,692	610	212	2.88
9.1	45,768	66,630	316	459	0.69
13.6	55,043	63,932	380	441	0.86
18.6	52,870	61,316	365	423	0.86
30.1	65,138	60,551	449	417	1.08
40.4	72,074	58,732	497	405	1.23

UNTJ6SB					
σ cyclic [psi]	Mr–Subbase [psi]	Mr - Subgrade [psi]	Mr–Subbase [MPa]	Mr - Subgrade [MPa]	R
13.7 (conditioning)					
4.2	22,429	14,931	155	103	1.50
8.6	13,795	23,205	95	160	0.59
13.7	15,093	23,638	104	163	0.64
18.9	10,687	22,454	74	155	0.48
29.6	7,230	18,066	50	125	0.40
38.5	6,298	15,253	43	105	0.41

UNTL3SB					
σ cyclic [psi]	Mr–Subbase [psi]	Mr - Subgrade [psi]	Mr–Subbase [MPa]	Mr - Subgrade [MPa]	R
13.5 (conditioning)					
4.2	15,698	35,736	108	246	0.44
8.7	18,692	34,752	129	240	0.54
13.5	21,674	34,380	149	237	0.63
18.9	19,276	35,991	133	248	0.54
28.6	18,641	36,679	129	253	0.51
38.7	18,770	36,329	129	250	0.52

Table B.3 Universal model parameters for aggregate subbase derived plate load tests, as reported by the company that performed the tests (Ingios, 2021)

	k1	k1	k2	k3
SBRITE Tests	CTC5SB	3274.6	0.833	-3.136
	CTJ2SB	2052.6	0.626	-1.177
	CTM2SB	2809.1	0.154	0.746
	UNTJ6SB	1462.7	-0.251	-2.316
	UNTJ6SB	1399.1	0.388	-2.398
FHWA report*	*Mean*	*873.2*	*0.626*	*-0.170*
	Standard deviation	*272.6*	*0.133*	*0.215*
	Maximum	*1847.4*	*1.062*	*0.000*
	Minimum	*280.9*	*0.174*	*-2.898*

**You and Von Quintus (2002)*

statistics refer to 423 sets of data for unbound aggregate base and subbase materials

APPENDIX C. SUPPLEMENTARY PLOTS FROM ANALYSIS OF RDL TEST DATA

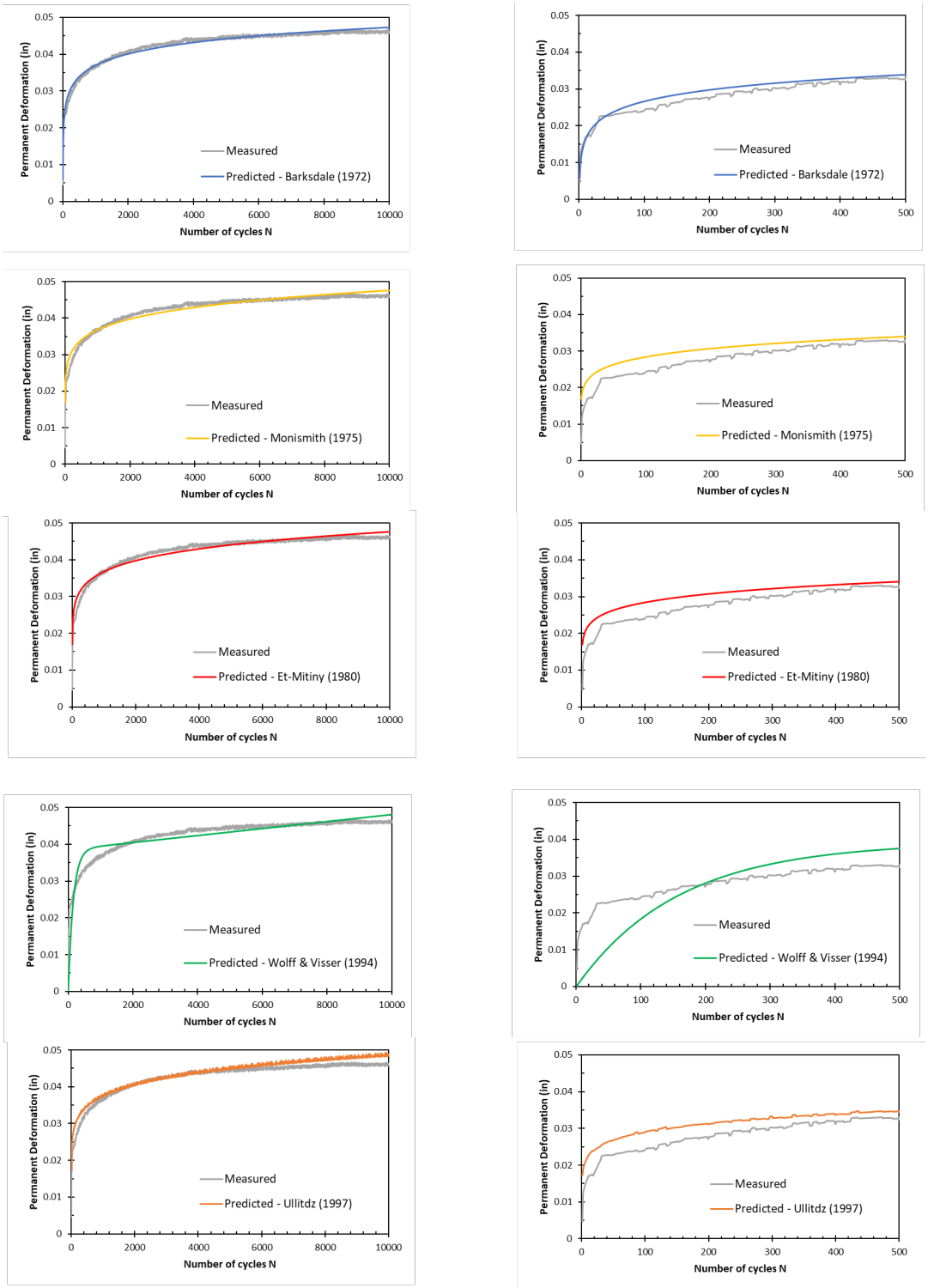

Figure C.1 Comparison of predicted versus measured curves of permanent deformation versus number of loading cycles for test CTO4SB (10,000 cycles): (a–b) Barksdale (1972) model; (c–d) Monismith (1975) model; (e–f) El-Mitiny (1980) model; (g–h) Wolff & Visser model (1994); and (i–j) Ullitdz model.

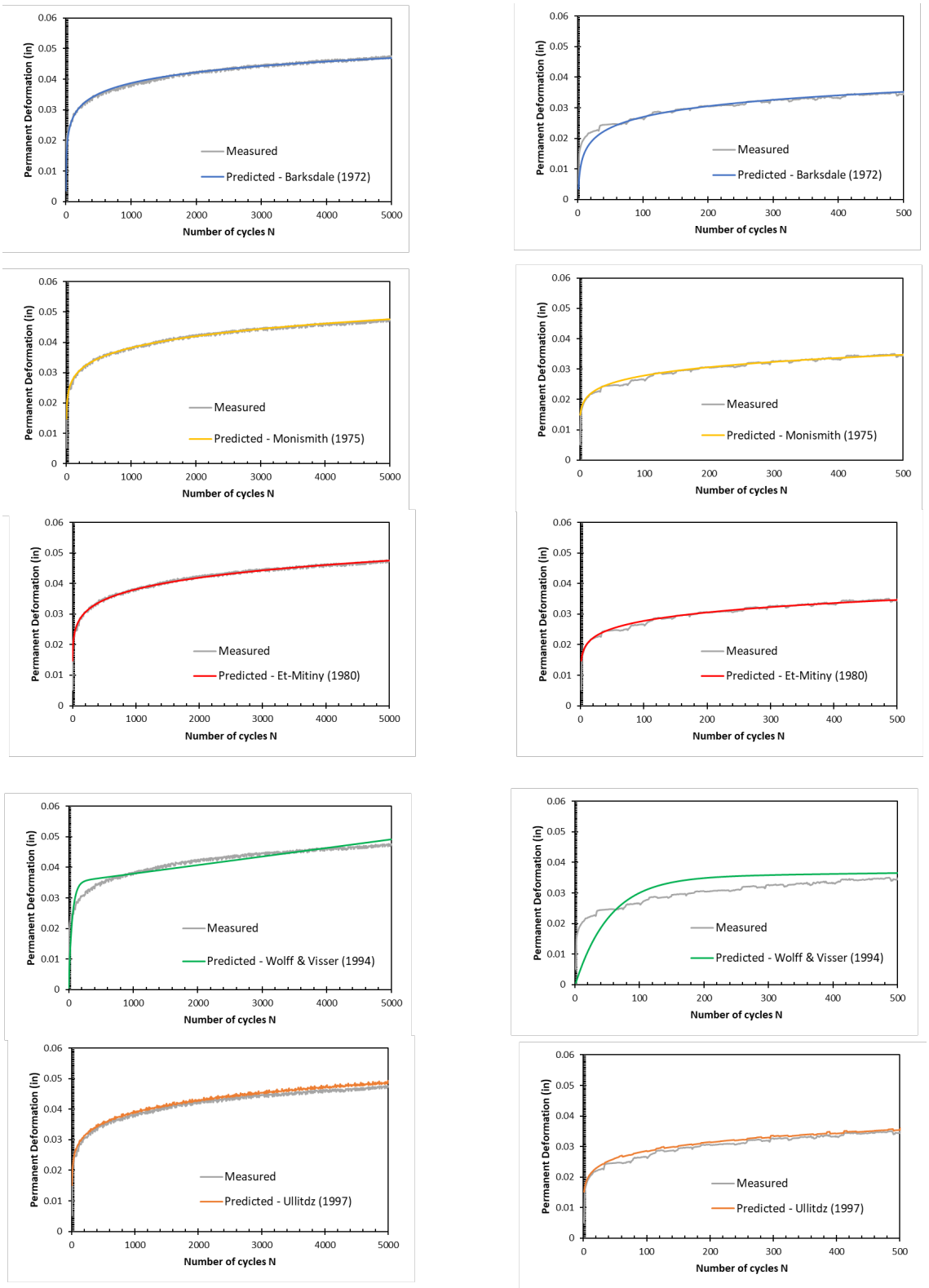

Figure C.2 Comparison of predicted versus measured curves of permanent deformation versus number of loading cycles for test CTQ2SB (5,000 cycles): (a–b) Barksdale (1972) model; (c–d) Monismith (1975) model; (e–f) El-Mitiny (1980) model; (g–h) Wolff & Visser model (1994); and (i–j) Ullitdz model.

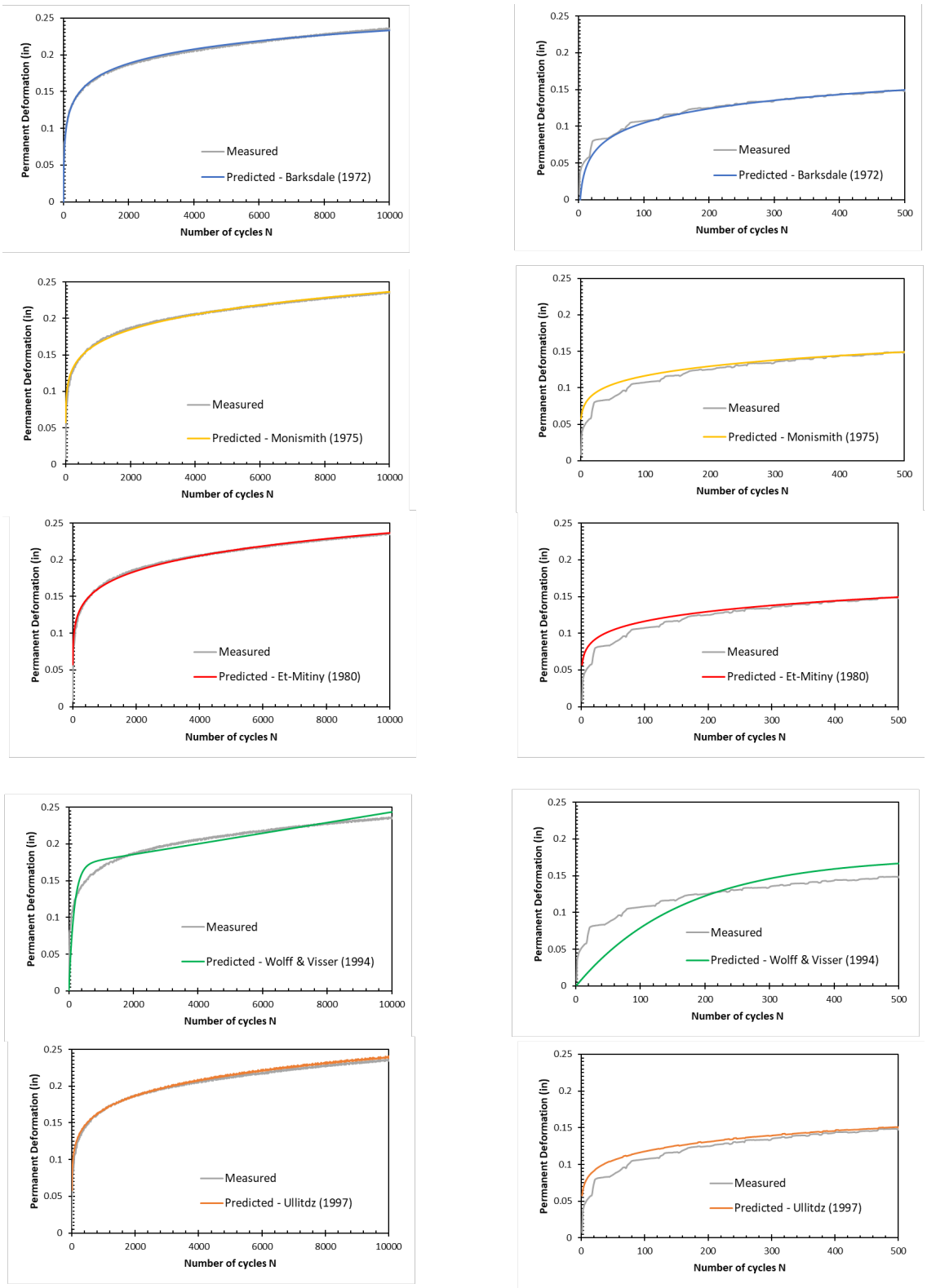

Figure C.3 Comparison of predicted versus measured curves of permanent deformation versus number of loading cycles for test UNTI2SB (10,000 cycles): (a–b) Barksdale (1972) model; (c–d) Monismith (1975) model; (e–f) El-Mitiny (1980) model; (g–h) Wolff & Visser model (1994); and (i–j) Ullitdz model.

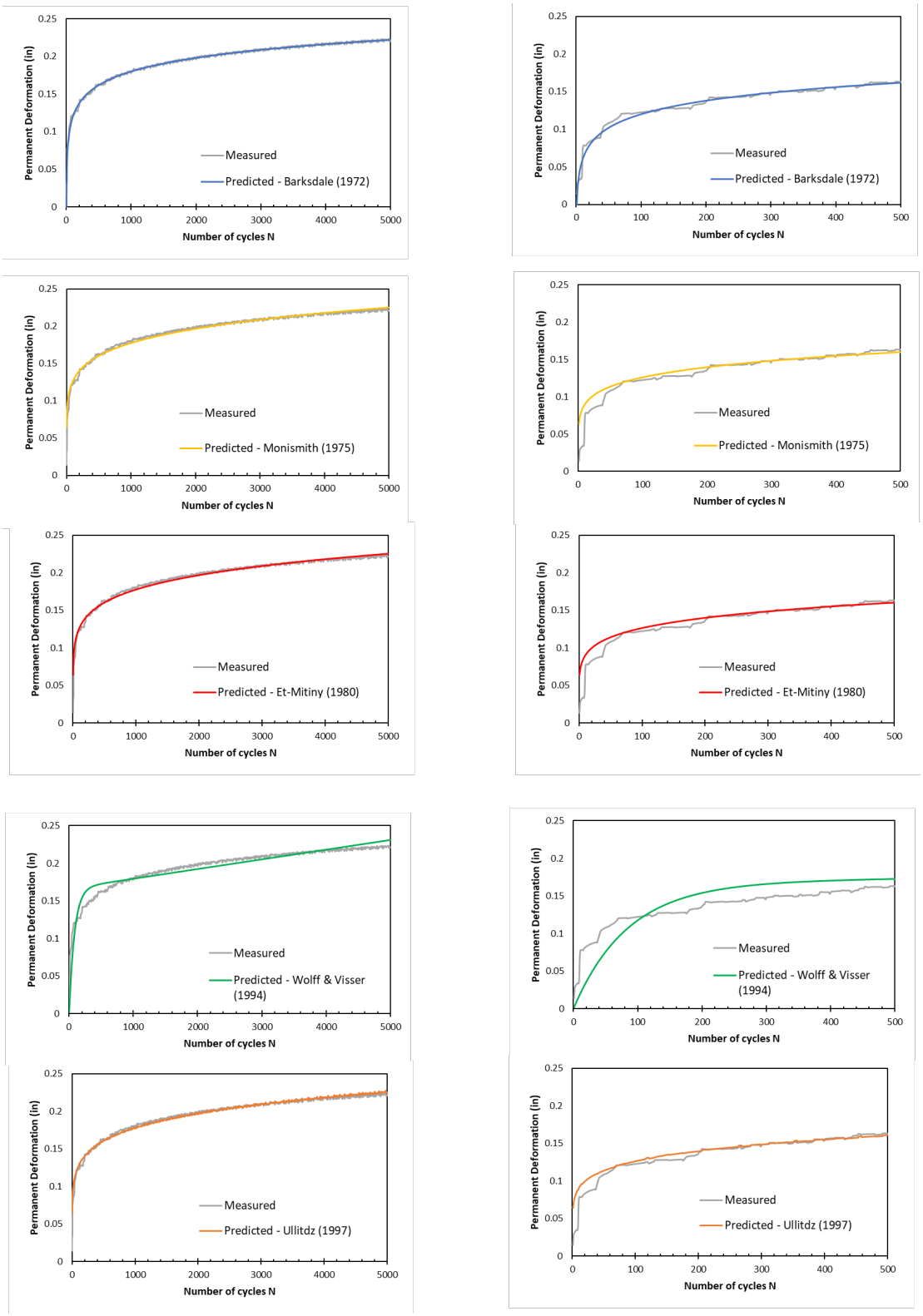

Figure C.4 Comparison of predicted versus measured curves of permanent deformation versus number of loading cycles for test UNTI2SG (5,000 cycles): (a–b) Barksdale (1972) model; (c–d) Monismith (1975) model; (e–f) El-Mitiny (1980) model; (g–h) Wolff & Visser model (1994); and (i–j) Ullitdz model.

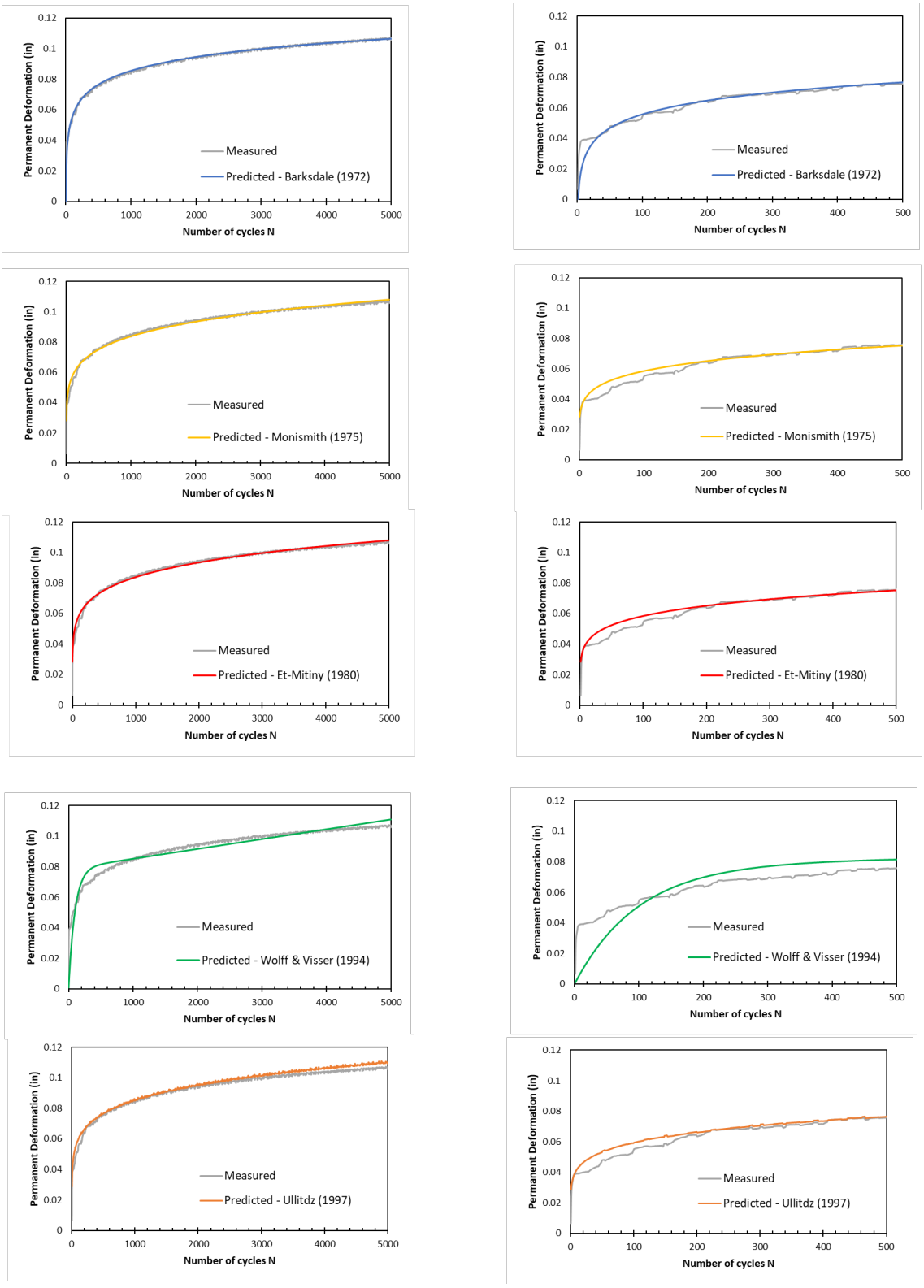

Figure C.5 Comparison of predicted versus measured curves of permanent deformation versus number of loading cycles for test UNTQ3SG (5,000 cycles): (a–b) Barksdale (1972) model; (c–d) Monismith (1975) model; (e–f) El-Mitiny (1980) model; (g–h) Wolff & Visser model (1994); and (i–j) Ullitdz model.

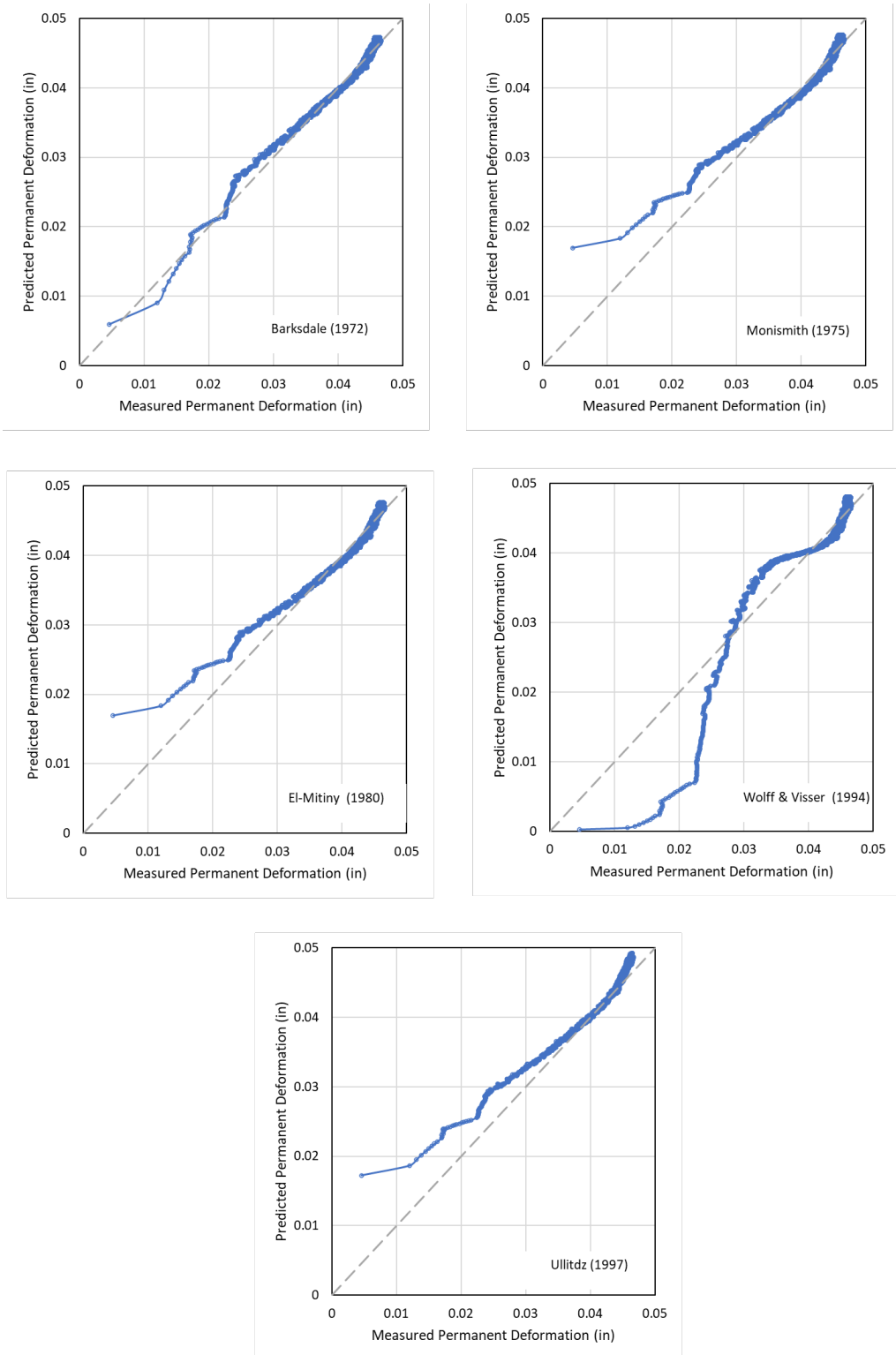

Figure C.6 Comparison of predicted versus measured permanent deformation for test CTO4SB: (a) Barksdale (1972), (b) Monismith (1975), (c) El-Mitiny (1980), (d) Wolff & Visser model (1994), and (e) Ullitdz model.

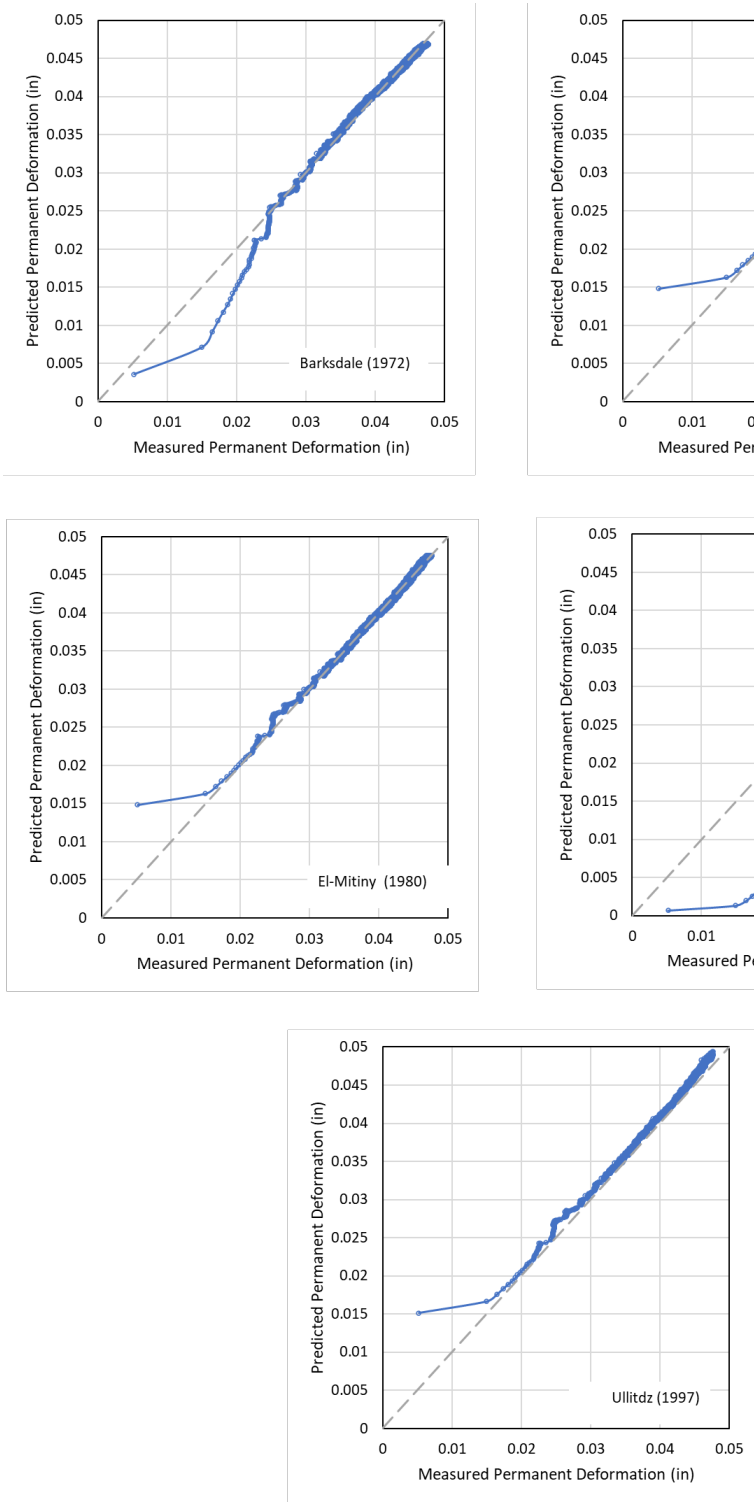

Figure C.7 Comparison of predicted versus measured permanent deformation for test CTQ2SB: (a) Barksdale (1972), (b) Monismith (1975), (c) El-Mitiny (1980), (d) Wolff & Visser model (1994), and (e) Ullitdz model.

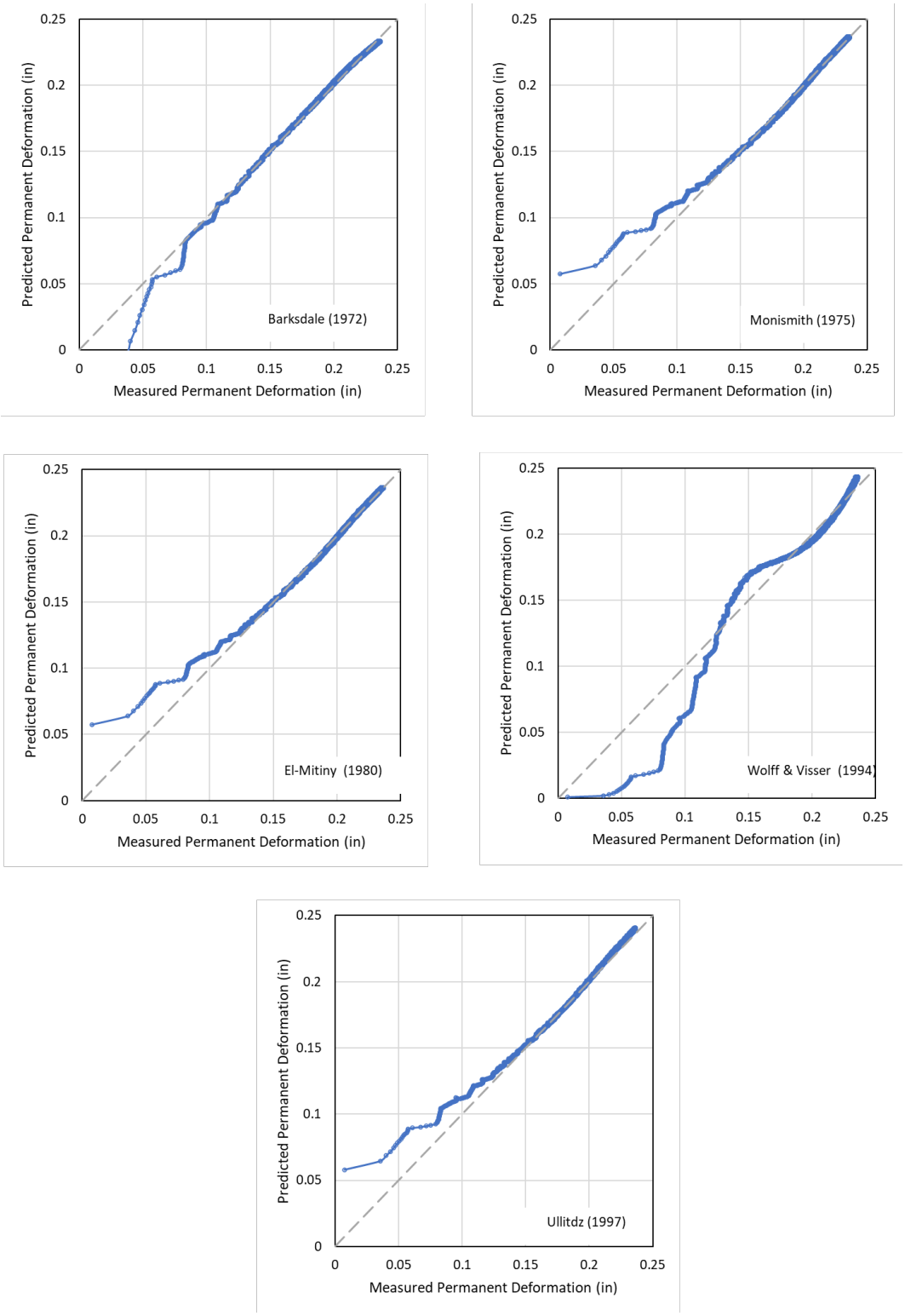

Figure C.8 Comparison of predicted versus measured permanent deformation for test UNTI2SB: (a) Barksdale (1972), (b) Monismith (1975), (c) El-Mitiny (1980), (d) Wolff & Visser model (1994), and (e) Ullitdz model.

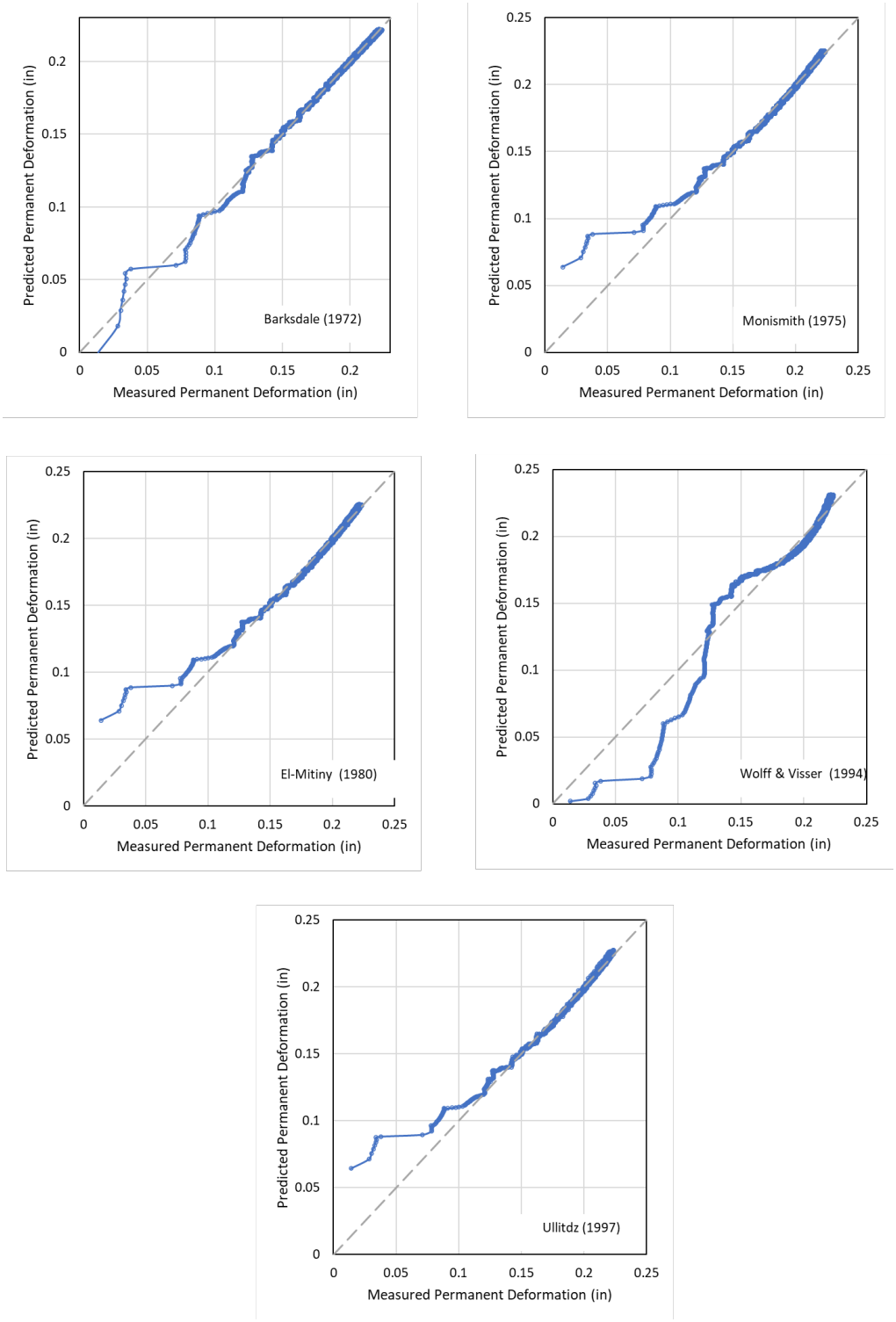

Figure C.9 Comparison of predicted versus measured permanent deformation for test UNTI2SG: (a) Barksdale (1972), (b) Monismith (1975), (c) El-Mitiny (1980), (d) Wolff & Visser model (1994), and (e) Ullitdz model.

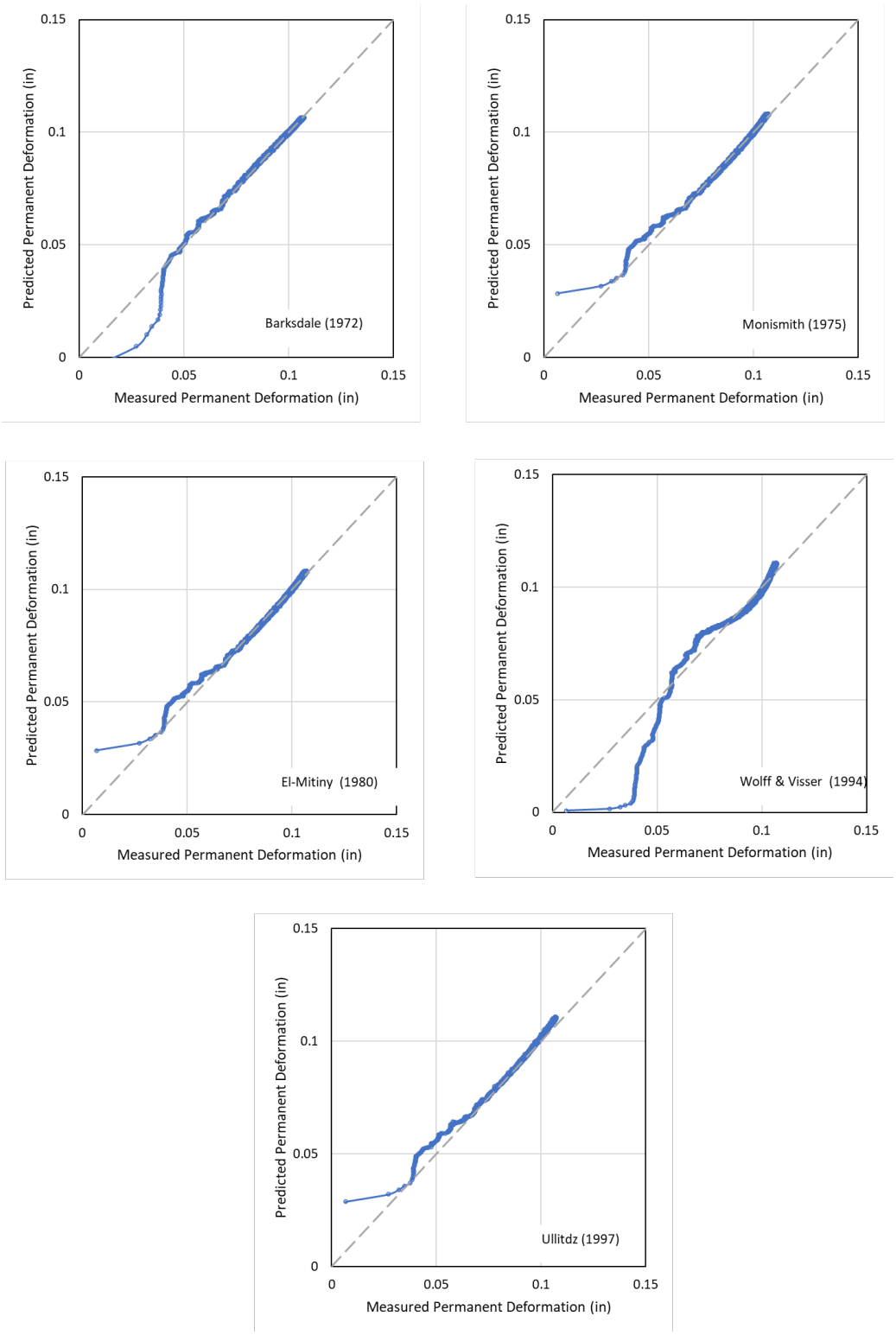

Figure C.10 Comparison of predicted versus measured permanent deformation for test UNTQ3SG: (a) Barksdale (1972), (b) Monismith (1975), (c) El-Mitiny (1980), (d) Wolff & Visser model (1994), and (e) Ullitdz model.

APPENDIX D. IMAGES OF EXHUMED GEOTEXTILE FABRIC

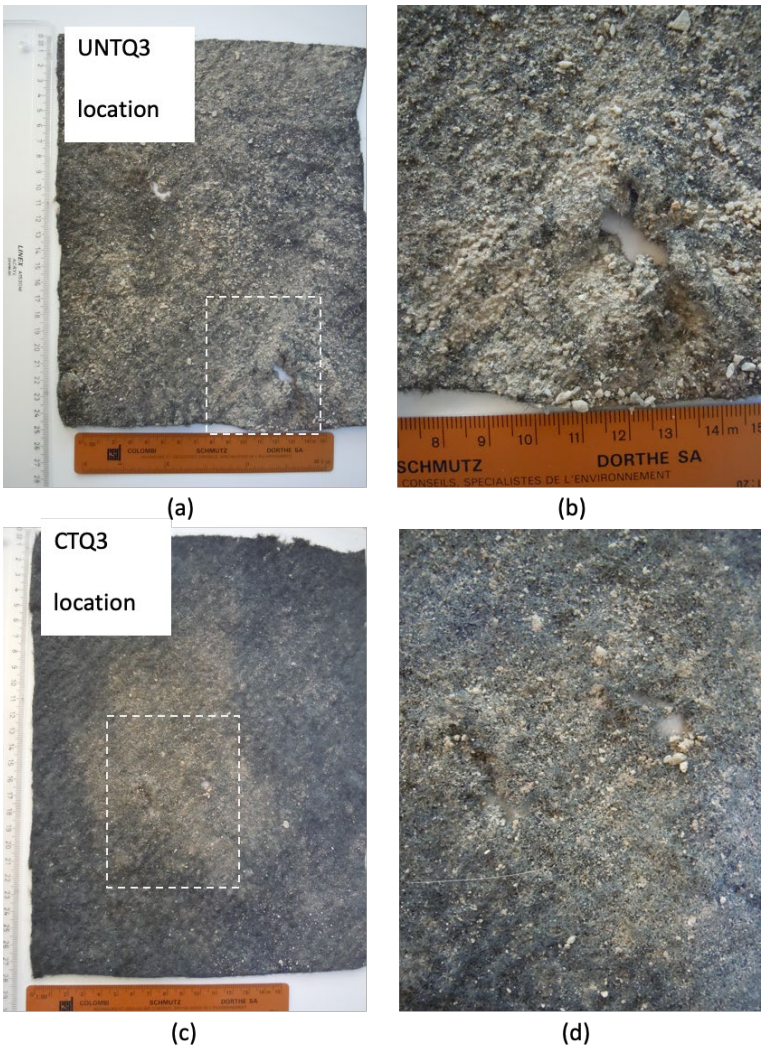

Figure D.1 Photos of geotextile samples (view of geotextile face in contact with aggregate) exhumed immediately below location of RDL tests: (a–b) UNTQ3 location on untreated strip; (c–d) CTQ2 location on cement treated strip. (b) and (d) show detail of photos (a) and (c).

About the Joint Transportation Research Program (JTRP)

On March 11, 1937, the Indiana Legislature passed an act which authorized the Indiana State Highway Commission to cooperate with and assist Purdue University in developing the best methods of improving and maintaining the highways of the state and the respective counties thereof. That collaborative effort was called the Joint Highway Research Project (JHRP). In 1997 the collaborative venture was renamed as the Joint Transportation Research Program (JTRP) to reflect the state and national efforts to integrate the management and operation of various transportation modes.

The first studies of JHRP were concerned with Test Road No. 1—evaluation of the weathering characteristics of stabilized materials. After World War II, the JHRP program grew substantially and was regularly producing technical reports. Over 1,600 technical reports are now available, published as part of the JHRP and subsequently JTRP collaborative venture between Purdue University and what is now the Indiana Department of Transportation.

Free online access to all reports is provided through a unique collaboration between JTRP and Purdue Libraries. These are available at http://docs.lib.purdue.edu/jtrp.

Further information about JTRP and its current research program is available at http://www.purdue.edu/jtrp.

About This Report

An open access version of this publication is available online. See the URL in the citation below.

Pajo, B., Becker, P. J., Bourdeau, P. L., & Santagata, M. (2023). *Data interpretation of automated plate load test (APLT) for real-time in situ determination of unbound layer resilient modulus* (Joint Transportation Research Program Publication No. FHWA/IN/JTRP-2023/22). West Lafayette, IN: Purdue University. https://doi.org/10.5703/1288284317653